Development of Advanced MR Elastography Techniques for Biomechanical Assessment of Neurodegeneration

Em Rose Triolo

A dissertation

submitted in partial fulfillment of the

requirements for the degree of

Doctor of Philosophy

University of Washington

2024

Reading Committee:

Mehmet Kurt, Chair

Katherine M. Steele

Swati Rane Levendovszky

Program Authorized to Offer Degree:

Mechanical Engineering

University of Washington

Abstract

Development of Advanced MR Elastography Techniques for Biomechanical Assessment of Neurodegeneration

Em Rose Triolo

Chair of the Supervisory Committee:

Mehmet Kurt

Department of Mechanical Engineering

Alzheimer's disease (AD) is the leading cause of dementia in the aging population worldwide, and a progressive neurodegenerative condition of enormous socio-economic impact. Identification of non-invasive correlates of these pathologies to aid diagnosis in the earliest stages of disease will help to afford improved disease management and prevention. One such non-invasive correlate that has received growing attention involves the study of the mechanical properties of the brain via MR Elastography (MRE) , as it is becoming increasingly clear that tissue mechanics are related to the underlying cellular microstructure and overall health state of an organ. Pivotal studies applying MRE at 3T have shown a progressive softening of white and gray matter tissue in AD patients compared to healthy controls (especially in the frontal, parietal and temporal lobes) in line with the known topography of AD pathology. One of the limitations of this approach, however, is that the underlying microstructural causes of tissue viscoelasticity variations cannot be directly determined, hence there is a lack of physical understanding regarding the meaning of these parameters in the context of dementia and neurodegeneration. This

difficulty limits the current predictive value of MRE for early diagnosis and for the assessment of individual risk of developing cognitive decline. This work seeks to investigate noise reduction and applications of ultra-high field (7T) magnetic resonance elastography (MRE) in determining the mechanical properties of brain tissue, with applications in early detection of dementias.

Table of Contents

List of Figures

List of Tables

Acknowledgements

This endeavor would not have been possible without the support and feedback of my advisor, Dr. Mehmet Kurt. It is due to his enthusiasm first and foremost that I joined his lab at Stevens Institute of Technology, and it was with his support and feedback that I was able to complete the projects I started working on back in 2019. While moving across the country to continue working on the project I resolved to dedicate myself to seemed impossible at times, I am so very grateful for the flexibility Dr. Kurt allowed me. Living on two coasts for 2022 and 2023 was quite the arrangement, but it worked even better than expected. I would also like to extend my sincere thanks Dr. Priti Balchandani for being so welcoming and supportive throughout my Ph.D., and for making me feel like a member of her lab when on the opposite side of the country from my own. I am also deeply indebted to Dr. Oleksandr Khegai who has been my closest collaborator over the past five years. I absolutely could not have accomplished what I did without his knowledge, expertise, guidance, and hard work. Even when 12 hours apart in time zones, he always made time for me somehow.

I would also like to thank my reading committee, Dr. Katherine Steele and Dr. Swati Levendovszky, as well as my GSR, Dr. Paul Kinahan, for taking time our of their busy schedules to be on my committee, and for their invaluable feedback. I am also incredibly grateful to my lab mates for their support in research projects, moving across the country, and of course, in moral support when deadlines seemed too close to hit and working hours became long. Specifically, thank you to Fargol, Ya-Chen, Javid, Gloria, Efe, Caitlin, Tyson, Juampablo, Aymeric, Aislinn, Akbar, and Mackenzie. Thank you Mackenzie and Efe for giving me the advice to not get married in the same six months as your dissertation defense- that would have been a nightmare. Many thanks to the University of Washington students for being so welcoming. I have never claimed to be the best at making friends, but meeting Melody in MEB on one of those first lonely and rainy days in January 2022 definitely eased some of my fears. Other students like Mia and Kelly, my trivia friends Garrett, Can, Jack, and Charlotte, my housemates Emma, Chris, and Sydney, and, of course, Howl the cat were fundamental in keeping me sane in my new city.

I would be remiss in not thanking my many, many collaborators and co-authors from labs all over the country (and some outside the country) who were fundamental in completing this work. Special thanks to Dr. Curtis Johnson and his lab, Dr. Matt McGarry, and Dr. Grace McIlvain for all their technical help and for keeping me company at conferences. Also thank you to Dr. Johannes Weickenmeier and other professors at Stevens Institute of Technology for helping me get started on my Ph.D. journey. I am also grateful to BMEII at Mount Sinai Hospital and everyone who works there for allowing me to 'volunteer' and helping me to collect the majority of my data. Many thanks to Dr. Brett BuSha and all the folks at The College of New Jersey for fostering my interest in engineering research and always pushing me to do my best work. I am also grateful for my friends and teachers from BTHS who played a huge role in my enthusiasm for learning. I would also like to acknowledge all my funding support that financed my research from the NSF, NIH, University of Washington, and Stevens Institute of Technology.

I, of course, could not have undertaken this journey without my family, friends, and my future husband, Zach Michonski. Although scheduling got pretty crazy after a while, game nights with friends always brought my so much joy and took my mind of off work for a while, and pictures of Minerva from Luke and Rhiannon, of Princess from Carly and Ben, and of Mause from Jason and Chris never fail to make me smile. I am so very lucky that my dad, Dr. Tony Triolo, also went through getting a Ph.D. in engineering, so my mom and him always knew what I was going through. I was extra lucky that our research is tangentially related enough that I could still go to him for advice like I did when I was a kid in school. Finally, to my lovely Zach, I do not know how I would have done this without you. Having to leave for months was the hardest thing I have had to do, and coming home to you was always the happiest. Thank you for coming on this adventure with me and the hours of calls, and I cannot wait to see what the future holds for us.

I thought it would be funny to end this acknowledgements section with some stats about my Ph.D. journey. A lot of these are airplane-related, but here are some fun facts:

- Number of Flights Taken (2022-present): 43
- First Class Upgrades: 4

- Conferences attended: 16
- Checked Bags Lost: 1
- Weddings Attended: 7
- Pandemics Survived: 1
- Universities Attended (for Ph.D.): 2
- Miles Flown (2022-present): ~100,000
- Time Spent in the Air (2022-present): ~230 hours
- Number of times I've been asked my age to sit in an exit row: 5
- MRI Scans performed on myself: 11
- Months lived in Seattle: 16
- Months of renting in two cities simultaneously: 24
- Countries Visited: 5
- Desks Used: 10
- University Email Accounts: 3
- Favorite Scanner Sound: 7T Manual Shimming
- Glasses of Wine: uncountable
- Zoom Calls: also uncountable

To my family and ever-patient Zachary— what a journey this has been.

Chapter 1: Introduction

1.1. Background and Motivation

Historically, pathologies such as tumors or lesions have been identified by physicians by manually palpating soft tissue to compare the mechanical properties of healthy tissue to potentially malignant tissues. However, for internal organs, such as the brain, this technique is not feasible. Therefore, it was necessary for a secondary method of producing these results, or even more accurate results, to be developed, such as Magnetic Resonance Elastography (MRE)[1]. Elastography uses mechanical tissue deformation and detection methods to determine the response of tissue to that mechanical tissue deformation[2]. There are many different methods to apply the force for tissue deformation, and magnetic resonance imaging (MRI) is a popular method of detection of motion in that tissue[1]. In MRE, or the process of performing elastography using MRI, the most common form of recurrently deforming tissue in a controlled manner is through harmonic vibration[3]. Viscoelastic models are used to extract structural information from MRE measurements by establishing a mathematical relationship between viscoelastic parameters of tissue and its response to the resulting deformation from the harmonic vibration applied. Performing MRE on brain tissue can provide information on different structures within brain tissue based on their mechanical properties, such as cell density, myelination, inflammation, vascular density, and functional activation[4–19]. These mechanical parameters can then be used to diagnose pathologies such as multiple sclerosis (MS), Alzheimer's disease, and Parkinson's disease, or indicate disease progression[10,20–28].

Currently, studies investigating the mechanical properties of the human brain using MRE are performed at conventional clinical MRI scanner field strengths of 3 Tesla (T) and 1.5T[1]. More recently there have been a few attempts at performing MRE on the human brain at the ultra-high field strength 7T[29]. This ultra-high field strength allows for higher resolution imaging and higher signal-to-noise ratio (SNR), potentially allowing for the determination of the properties of smaller brain sub-structures that have been suggested at 3T MRE. However, many advancements must be made to MRE hardware, scanner software, and post-processing techniques to make this feasible. When performing MRE, harmonic vibration must be induced in the tissue in synchronization with the motion encoding gradient (MEG) in the MRE sequence[30].

This process requires a type of harmonic actuator that can be used to actuate tissue inside the MRI machine. Therefore, this actuator must be MR compatible or at least have the part of the driver unit (end-effector) that goes inside the scanner room be MR compatible. This end-effector must also be comfortable for the subject for the duration of the scans being executed in the MRI scanning protocol, and provide appropriate vibration amplitude equally across the subject's head[31]. Additionally, in higher field strength MRI scanners, head coils are typically smaller, requiring a more compact end-effector. Additionally, at higher field strengths no metal, even non-ferrous metals, can be present in the scanner room, rendering some MRE actuator designs unusable and placing even more hardware limitations of such designs.

Aiming for higher resolution scans of the human brain at 7T, MRE presents unique challenges of decreased octahedral shear strain-based signal-to-noise ratio (OSS-SNR) and lower shear wave motion sensitivity. Additionally, it has been shown that quantitative values of MRE, i.e., the magnitude of the complex shear modulus estimate (|G*|), are sensitive to changes in this SNR measure[32], so 7T MRE can present a challenge of not only quality, but accuracy. While applying commonly-used filtering techniques (e.g., Gaussian, Median) to MRE phase data can increase OSS-SNR (to combat low OSS-SNR in high-resolution scans), this can also blur fine physiological features, decrease the effective resolution, resulting in artificially increased |G*|[1]. We can increase the OSS-SNR of our MRE acquisition without comprising the anatomical accuracy and spatial resolution by utilizing an advanced denoising algorithm[33]. In this technique, we can exploiting the intrinsic redundancies in MRE acquisition to identify and remove noise-only principal components[33]. We also apply advanced reconstruction to the raw MRI scanner data using a program called Gadgetron to remove artifacts due to scanner reconstruction error.

In the most recent studies comparing 1.5T, 3T, and 7T MRE of the human brain, MRE at 7T and 1mm resolution resulted in significantly lower stiffness values than MRE at 1.5T and 3T at 2mm resolution[34,35]. However, one study indicated that when down-sampled to 2mm, the 7T MRE results matched the traditional MRE field strength results, but in a second study, the difference remained[34,35]. In the past, we have shown that changes in resolution and field strength do not inherently change the value of

|G*| in a linear elastic phantom[36,37]. However, MRE of phantoms typically have very high SNR, even at high resolutions, so this decrease in SNR as resolution increases may not have a large effect on scans with inherently high SNR. For MRE of the human brain, however, SNR drastically drops with increasing resolution, very likely causing an artificially low |G*| calculation. Another hypothesis that requires more evidence, however, is that different structures are being captured at these higher resolutions (and potentially higher field strength in general) resulting in these differences. Additionally, most biological tissues, including the human brain, exhibit a frequency-dependent mechanical response[7], specifically around boundaries[38], which has yet to be explored at 7T.

Despite all these drawbacks, lack of validation thus far, and more unanswered questions, performing MRE at 7T, and more specifically at high resolution, proves to be an attractive option for investigations into small brain structures. One application mentioned previously is detection of neurodegeneration and disease progression in Alzheimer's disease. Early diagnosis of Alzheimer's disease is still challenging, because of the subtlety of the microstructural changes it initially causes in the brain and the difficulty of identifying them with traditional neuroimaging techniques such as MRI, PET or CT scans. However, recent evidence has revealed that the neurodegeneration characterizing AD is accompanied by effective tissue softening, which can be quantified *in vivo* using MRE. Previous MRE studies have clearly indicated that AD is characterized by brain tissue softening accompanying neurodegeneration. However, MRE at conventional field strengths alone is insufficient to characterize how variations in regional viscoelasticity correlate with tissue microstructure. Hence, there is a lack of physical understanding regarding the meaning of these parameters in the context of dementia and neurodegeneration, which limits the current predictive value of MRE for early diagnosis and for the assessment of individual risk of developing cognitive decline. This is the draw, therefore, of MR neuroimaging at 7T, wherein a multi-modal approach (including MRE among other advanced 7T MRI sequences) will enable the joint analysis of biomechanical, connectomic and pathologic markers in AD patients and bring novel insights in our understanding of the mechanisms of AD onset and progression. To apply such neuroimaging, however,

many previously stated questions about its application must be answered, drawbacks must be addressed, and all aspects must be validated in phantoms, healthy human subjects, and finally older adults and Alzheimer's disease patients. Overall:

This work seeks to investigate noise reduction and applications of ultra-high field (7T) magnetic resonance elastography (MRE) in determining the mechanical properties of brain tissue, with applications in early detection of dementias.

1.2 Aims

In this work, we aim to first design, validate, and implement MRE actuator hardware (Aim 1), sequences, and post-processing pipelines at both 7T and 3T for use on both phantoms and the human brain (Aim 2). We will then use these validated methods to answer fundamental questions regarding high resolution mechanical imaging of the healthy human brain using different viscoelastic inversion methods (Aims 3 and 4). Finally, we will utilize this new information and processes to determine the feasibility of MRE as a biomarker or neurodegenerations, specifically in Alzheimer's Disease (Aim 5).

1.1.1. Aim 1: Design, Implement, and Validate a 7T Compatible Convertible Pneumatic MRE Actuator for Use on Phantom and the Human Brain

In MRE, mechanical waves generated by the actuator, usually transmitted in a burst of specified duration, must be synchronized with the MR signal excitation[39]. The vibration frequency, dependent on the application, is generally in the range of 40-120Hz. In order to perform MRE at 7T, however, a novel actuator that is ultra-high field compatible and approved needs to be developed and validated due to the size, material, and T2 relaxation constraints imposed by moving to 7T. Additionally, because the actuator must be used in an ultra-high field MR setting, the tissue-contacting portion of the actuator must contain only ultra-high MR-safe materials. In this Aim, we will build and validate two types of MRE actuators. In the first part of this Aim, we will design, build, and validate a 7T-compatible convertible pneumatic actuator to applying distributed vibration to both human and phantom. The phantom MRE will be used for amplitude, frequency, and sequence integration validation, as well as validation of the basic viscoelastic inversion algorithm use to calculate stiffness. Subsequently, 5-10 healthy human test MRE scans will be

performed with the device to create the optimal end effector (pillow) design for both vibration application and patient comfort.

1.1.2. Aim 2: Sequence and Software Framework Development for High Resolution, Low Noise MRE of the Human Brain at 7T

Recently, there have been a few attempts at performing MRE on the human brain at the ultra-high field strength 7T[29], which allows for higher resolution imaging and higher signal-to-noise ratio (SNR). This advancement will potentially allow for the determination of the properties of smaller brain sub-structures that have been suggested at 3T MRE and has specific applications in early diagnosis of neurodegenerative diseases such as Alzheimer's disease. However, in moving to 7T and subsequently higher resolution, MRE presents unique challenges of decreased octahedral shear strain-based signal-to-noise ratio (OSS-SNR) and lower shear wave motion sensitivity. Additionally, it has been shown that quantitative values of MRE, i.e., the magnitude of the complex shear modulus estimate (|G*|), are sensitive to changes in OSS-SNR[32], so 7T MRE can present a challenge of not only quality, but accuracy. In this Aim, we propose a novel 7T MRE sequence and post-processing framework to obtain accurate 1.1 mm isotropic resolution mechanical property maps (elastograms) of the human brain. To do this, we will first perform validation scans of our elasticity phantom with known mechanical properties at both 3T and multiple resolutions at 7T to ensure that there are no inherent differences in our algorithms between field strengths and resolutions in a linearly elastic, homogeneous material. Next, we will test this sequence and initial post-processing method in healthy human subjects to show human-use feasibility, ensure that mechanical displacement is visible in brain tissue at high resolution at 7T (and ensure that OSS-SNR is high enough for inversion), and perform initial development of direct inversion post-processing to calculate the complex shear modulus in the brain. This aim will be performed concurrently with Aim 1.

1.1.3. Aim 3: Validation of High Resolution and Ultra-High Field Strength MRE on Shear Stiffness Reconstruction of the Human Brain Using Direct Inversion

In the most recent studies comparing 1.5T, 3T, and 7T MRE of the human brain, MRE at 7T and 1mm resolution resulted in significantly lower stiffness values than MRE at 1.5T and 3T at 2mm resolution[34,35]. However, one study indicated that when down-sampled to 2 mm, the 7T MRE results

matched the traditional MRE field strength results, but in a second study, the difference remained[34,35]. In the past, we have shown that changes in resolution and field strength do not inherently change the value of complex shear stiffness in a linear elastic phantom[36,37]. In the past, we have shown that changes in resolution and field strength do not inherently change the value of complex shear stiffness in a linear elastic phantom[36,37]. However, MRE of phantoms typically have very high SNR, even at high resolutions, so this decrease in SNR as resolution increases may not have a large effect on scans with inherently high SNR. For MRE of the human brain, however, SNR drastically drops with increasing resolution, very likely causing an artificially low complex shear stiffness calculation. Another hypothesis that requires more evidence, however, is that different structures are being captured at these higher resolutions (and potentially higher field strength in general) resulting in these differences. In this Aim, we will determine if we are capturing different viscoelastic features at higher resolutions and field strengths or if these apparent differences in |G*| and its components are due to low OSS-SNR at high resolution. This Aim's importance lies in determining whether different resolutions require different 'baseline' mechanical properties to compare to in the case of potential neurodegeneration, if it is simply enough to control for OSS-SNR in analyses, or if both must be done. To accomplish this, we will recruit 20 healthy human subjects (ages 18-35) to undergo 3T MRE at the standard 2.5 mm isotropic resolution and 7T MRE at matched (2.5 mm) isotropic resolution, a middle 1.7 mm isotropic resolution, and finally our 1.1 mm high resolution. The previously validated advanced post-processing techniques will be performed on each field strength and resolution group, and Complex Shear Modulus, its components, and OSS-SNR will be compared between these groups.

1.1.6. Aim 4: Characterizing Brain Mechanics Through 7T MRE with 3T MRE Comparison via Nonlinear Inversion

Direct inversion methods require a variety of simplifying mechanical assumptions that, while result in fast processing, may contribute to the observed resolution-dependent |G*| results for brain tissue. Because these |G*| values are calculated directly using displacement maps, it is very likely that higher spatial wave sampling rate is a contributor to this resolution-dependent differences. Additionally, using direct inversion

requires the application of many spatial and temporal smoothening filter (*e.g.*, curl filtering and Romano filtering), reducing both the effective property map resolution (and therefore the benefit of moving to high resolutions), and the benefit of using non-smoothening denoising methods like the MP-PCA denoised applied in the previous Chapter. Therefore, it became clear that moving to a finite element, optimization based, nonlinear inversional algorithm was necessary for better understanding of the mechanical properties of highly inhomogeneous and complex tissues such as the brain, as well as for determining clinical applicability of high resolution MRE. Nonlinear viscoelastic inversion, as developed by McGarry, *et al.*, has been extensively used and validated for MRE of the human brain at various resolutions at 3T (3.00 mm – 1.25 mm) and can calculate heterogeneous mechanical properties of tissue, reducing model-data mismatch that occurs in direct inversion methods (mcgarry 2021). This will allows us to better model the small heterogeneous structures in the brain that are also visible in other imaging modalities (mcgarry 2021).

Also, one of the main benefits of performing high resolution MRE at 7T is that other high resolution imaging modalities that are only available at 7T can also be captured for the same subjects in the same imaging sessions. The highest resolution that was performed in previous Chapters on the entire healthy young-adult cohort, 1.1 mm isotropic resolution, was specifically targeted because it is the resolution that is used during 7T Diffusion Tensor Imaging (DTI). By performing MRE at a matched resolution to these highly resolved 7T MRI sequences, we can determine the relationship between stiffness and these other properties like microstructural integrity, water diffusion, tissue anisotropy, perfusion, etc., as these contribute to the heterogeneity and anisotropic material properties of brain tissue. We will accomplish this by re-processing the 7T and 3T data collected in the previous Aim with nonlinear inversion to investigate the mechanical properties with greater detail and accuracy at the high resolution. We will also compare the property maps between the 3T MRE elastograms and the matched-resolution 7T elastograms to ensure that we are properly capturing the mechanical stiffness of brain tissue using our 7T method We will segment the brain not just into the main lobes, but also into smaller sub-regions using Freesurfer to determine potential mechanical property contrast differences in small regions. These subjects also will have underwent

DTI scanning at high resolution during the7T scanning protocol so we will also attempt to correlate these microstructural properties with mechanical properties.

1.1.7. Aim 5: MRE as a Biomarker for Alzheimer's Disease and for Exploration of Healthy Brain Aging

Alzheimer's disease (AD) is the leading cause of dementia in the aging population worldwide, and a progressive neurodegenerative condition of enormous socio-economic impact. The main pathogenic hallmarks of the disease are the progressive extracellular accumulation of β-amyloid (Aβ) plaques and intraneuronal aggregation of neurofibrillary tau tangles. Identification of non-invasive correlates of these pathologies to aid diagnosis in the earliest stages of disease will help to afford improved disease management and prevention. One such non-invasive correlate that has received growing attention involves the study of the mechanical properties of the brain via MRE, as it is becoming increasingly clear that tissue mechanics are related to the underlying cellular microstructure and overall health state of an organ. Pivotal studies applying MRE at 3T have shown a progressive softening of white and gray matter tissue in AD patients compared to healthy controls (especially in the frontal, parietal and temporal lobes) in line with the known topography of AD pathology. One of the limitations of this approach, however, is that the underlying microstructural causes of tissue viscoelasticity variations cannot be directly determined, hence there is a lack of physical understanding regarding the meaning of these parameters in the context of dementia and neurodegeneration. This difficulty limits the current predictive value of MRE for early diagnosis and for the assessment of individual risk of developing cognitive decline. In this final aim, we will test the efficacy of the MRE methods developed in the previous Aims on extracting MRE biomarkers in patient with AD and Mild Cognitive Impairment (MCI). For the first part of this Aim, we will develop a framework for correlating regional 7T MRE metrics and amyloid PET metrics, and perform this regional correlation on a small cohort of older healthy adults. In the second part of this Aim, we will perform high resolution 7T MRE and 7T DTI on a cohort of AD or MCI patients and a cohort of age-matched healthy controls who have all undergone amyloid PET scans and cognitive testing in a previous study. We will then utilize our previously validated advanced frameworks and post-processing techniques and correlate the regional complex shear modulus from MRE, fractional anisotropy and diffusivity from DTI, the previously collected

beta-amyloid PET, and cognitive testing results to determine microstructural changes as a result of neurodegeneration.

Chapter 2: Background

2.1. MRI Theory

In a standard anatomical MRI scan, a static magnetic field ($\mathbf{B}_o$) of a strength dependent on the MRI machine induces magnetization (**M**) in protons within its magnetic field to align with that field (where γ_p is the proton gyromagnetic ratio) [40].

$$\frac{d\boldsymbol{M}}{dt} = \gamma_p \boldsymbol{M} \times \boldsymbol{B_o} \qquad (1)$$

The rotation, or precession, of the protons' magnetization occurs at a rate (d**M**/dt) determined by the strength of the magnetic field, and the total magnetization has both a longitudinal and transverse component [40,41].

$$\boldsymbol{M}(t) = \boldsymbol{M}_{||}(t) + \boldsymbol{M}_{\perp}(t) \qquad (2)$$

A second magnetic field (B_1) can be used to tilt the magnetization from equilibrium (longitudinal plane) to the transverse plane [40]. This transverse magnetization induces a characteristic sinusoidal voltage signal in conductor loops/receive coils placed around the tissue of interest[41]. This received signal is divided and filtered into real and imaginary parts to determine the magnitude of the signal and phase angle between the transverse signal and axis of the rotating frame of reference[41]. However, the interactions of a spin with its surroundings will change the orientation of its magnetic moment[42]. This magnetization will dephase over time, moving from the transverse plane back to the longitudinal plane. T_1 is a time constant that indicates energy dissipation, or relaxation into the longitudinal axis over time[41,42].

$$\frac{\partial \boldsymbol{M}_{||}}{\partial t} = \frac{1}{T_1}(\boldsymbol{M}_o(t) + \boldsymbol{M}_{||}(t)) \qquad (3)$$

T_2 is a time constant that describes relaxation that occurs independently but simultaneously with T_1[42]. T_2 characterizes signal decay due to loss of phase coherence of the precession phase, meaning that the spins which were in phase immediately after excitation are no longer in phase with each other[42]. T_2 relaxation is said to characterize proton mobility, where a low proton mobility indicated by a small T_2[41].

$$\boldsymbol{M}_{\perp}(t) = \boldsymbol{M}_{\perp}(0) \cdot e^{-t/T_2} \qquad (4)$$

The sequential application of three orthogonal magnetic gradients leads to 3D spatial encoding of MRI signal, one in the 'slice selection' (SS) direction, one in the 'phase encoding' (PE) direction, and one in the 'readout' (RO) direction[40]. In the slice selection procedure, a combination of a slice select gradient and a sinc-shaped B_1 magnetic pulse excites only protons in a slice of specified orientation and thickness[40,41]. The phase encoding gradient is applied for a short time and is perpendicular to the slice-select gradient[40]. By applying the phase-encoding gradient, an excited spin is encoded in its precession phase as a function of its position along the phase-encoding axis[40]. The readout/frequency encoding gradient is perpendicular to slice selection and phase encoding gradients and is applied when the signal is being sampled by the receive coils' analog-to-digital converter[41]. Therefore, the receive coils will detect the magnetization signal (both magnitude and phase) as a superposition of all of the individual signals averaged over space[41]. By changing the amplitude and duration of the phase encoding gradient, different 'lines' of the image can be captured[40].

If readout begins immediately after B_1 excitation, T_2 relaxation would cause the signal amplitude at the end of the 'line' to be smaller than at the beginning of the 'line' leading to asymmetry in the image [41]. To overcome this asymmetry problem, the magnetization must be refocused by a B_1-like magnetization pulse so that the amplitude of the signal reaches a local maximum, or echo, at a certain time (TE or echo time) post-excitation [41]. Therefore, readout must be performed symmetrically around this local maximum so that the signal amplitude is symmetrical over the entire 'line'[41].

2.2. MRE Theory

MRE is a phase-contrast MRI technique, meaning that the relevant information is stored in the signal's phase as opposed to its amplitude[41]. In order to detect motion, another magnetic gradient pulse is added to the sequence (Fig. 2.2.1) called a motion encoding gradient (MEG)[43]. To isolate wave information, several images at different phases of wave oscillation must be acquired to calculate phase difference images. This capturing of wave images requires the signal acquisition be synchronized with the physical mechanical

vibration[43]. To achieve this, typically a trigger signal in the form of a TTL pulse is sent to the vibration generator by the MR scanner to initiate imaging [41]. Different wave phases are captured by repeating this triggering and acquisition process with different time delays, τ, to capture n wave phases at frequency, f, in steps of $\Delta\tau = \frac{1}{f \cdot n}$, so that one vibration cycle is sampled with n equidistant data points[41].

For capturing the accumulation of phase (ϕ(t)) due to motion, in the presence of the MEG gradient field superimposed on B_o (**G**(t)), a spin with position **x**(t) accumulates phase[44]:

$$\phi(t) = \gamma \int_0^t \boldsymbol{G}(t') \cdot \boldsymbol{x}(t') dt' \qquad (5)$$

The simple linear motion of this spin is described by:

$$\boldsymbol{x}(t) = x_o + v_o t \qquad (6)$$

Where x_o and v_o are the initial position and velocity[44]. Given that terms higher order than velocity are negligible, a MEG function establishes a relationship between the accumulation of phase and the first gradient moment[44]. The complex motion of the spin can be described as:

$$\boldsymbol{x}(t) = \boldsymbol{x}_o + \vec{\xi}(\boldsymbol{x}, t) \qquad (7)$$

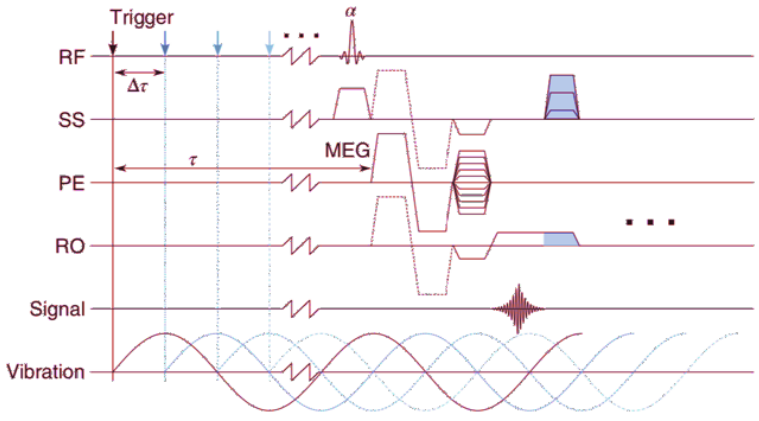

Figure 2.2.1: *Timing Schematic of A Common MRE Sequence Where The MEG is Applied Sequentially On The 3 Different Axes* [41]

Where $\mathbf{x}_o$ is the spin's average position, and $\vec{\xi}(\boldsymbol{x}, t)$ is the displacement of the spin about its average position, **x**, in this case[44]:

$$\vec{\xi}(\boldsymbol{x},\theta) = \overrightarrow{\xi_o}\cos\left(\boldsymbol{k}\cdot\boldsymbol{x} - \omega t + \theta\right) \qquad (8)$$

With **k** being the wave vector, θ being the phase offset, ω being the angular frequency of excitation, and $\overrightarrow{\xi_o}$ being the displacement amplitude, assuming that the spin undergoes simple harmonic motion[44]. The main assumption for the MEG gradient function is that it is considered to be the basis function for the harmonic components of **x**(t), where the area under the function is equal to zero for the time duration t, meaning that the gradient is switched in polarity at the same frequency of the spin's motion[44]. This then means that the phase accumulation is:

$$\phi(\boldsymbol{x},\theta) = \gamma\int_o^{t=N\cdot T<TE} \boldsymbol{G}(t)\cdot\overrightarrow{\xi_o}\cos\left(\boldsymbol{k}\cdot\boldsymbol{x} - \omega t + \theta\right)dt \quad (9)$$

$$\phi(\boldsymbol{x},\theta) = \frac{2\gamma NT(\boldsymbol{G}\cdot\overrightarrow{\xi_o})}{\pi}\sin\left(\boldsymbol{k}\cdot\boldsymbol{x} + \theta\right) \qquad (10)$$

Where N is the number of gradient cycles, T is the period of mechanical excitation, and TE is the time when the signal is received [44]. In practice, the gradient waveform and vibration frequency are chosen to meet the demands of wave mechanics, image resolution, signal quality, and hardware performance[41].

This final equation (10) is used to convert the phase shifts to displacement values in order to create a displacement map. Using these displacement maps, the wavelength (λ) of the mechanical waves in the medium is measured, and the magnitude of the shear modulus of the material (μ) was calculating using the basic inversion:

$$\mu = f^2\lambda^2\rho \qquad (11)$$

Where f is the frequency of the mechanical excitation and ρ is the density of the material/tissue[44].

2.3. Mechanical Modeling and SNR Calculation of Tissue using MRE

While equation (11) for calculating shear modulus is technically correct and was used in the initial MRE experiments and papers to calculate material properties, it is only truly useful for use with 1-D mechanical waves and is considered simplistic. Assuming linear wave propagation due to small

deformations (~1mm), the wave equation in a homogeneous and isotropic material can be derived from the relationship between displacement, strain, and stress. Change in displacement, ignoring translational motion, rotation, and rigid body deformation can be written as:

$$\delta u_i = \frac{\partial u_i(x)}{\partial u_j}\delta x_j = \frac{1}{2}\left(\frac{\partial u_i}{\partial x_j} + \frac{\partial u_j}{\partial x_i}\right)\delta x_j + \left(\frac{\partial u_i}{\partial x_j} - \frac{\partial u_j}{\partial x_i}\right)\delta x_j = (e_{ij} + \omega_{ij})\delta x_j \qquad (12)$$

Where e_{ij} is the strain tensor that contains the spatial derivatives of the displacement field (u) and ω_{ij} is the rotational translation. The relationship between strain and displacement can be written as:

$$e_{ij} = \frac{1}{2}(\nabla u + (\nabla u)^T) \qquad (13)$$

And using the relationship between displacement and stress, we can derive the following equation of motion (excluding body force):

$$\sigma_{ij,j}(x,t) = \rho\frac{\partial^2 u_i(x,t)}{\delta t^2} \qquad (14)$$

And we can then write the following constitutive equation:

$$\sigma_{ij} = C_{ijkl}e_{kl} \qquad (15)$$

In the isotropic case where C_{ijkl} only has Lame constants μ and λ such that we are now observing a linearly elastic, isotropic materials, we can write our wave equation as:

$$\rho\ddot{u} = (\lambda + 2\mu)\nabla(\nabla \cdot u) - \mu\nabla \times \nabla \times u \qquad (16)$$

We can further simplify using the assumption of incompressibility of our material and perform what is considered the Algebraic Inversion of the Differential Equation (AIDE) using the Helmholtz Equation:

$$\mu\nabla^2 u = -\rho\omega^2 u \qquad (17)$$

Which can also be written as (through Laplace Transform):

$$G(\omega) = \frac{\rho\omega^2 U}{\Delta U} \qquad (18)$$

Where G(ω) = G' + iG" is the complex shear modulus, which is the sum of the Storage Modulus (elastic modulus; real component) and Loss Modulus (viscous modulus; imaginary component). More complex inversions are also used to calculate material properties without simplifying to the Helmholtz equation, such as nonlinear viscoelastic inversion of the time-harmonic Navier's equation[45]. The time-harmonic Navier's equation describes the evolution of displacement fields in a viscoelastic medium given by Equation 19.

$$\nabla \cdot (\mu(\nabla \vec{u} + \nabla \vec{u}^T)) + \nabla(\lambda \nabla \cdot \vec{u}) = -\rho\omega^2 \vec{u} \qquad (19)$$

Where μ is the complex-valued viscoelastic shear modulus, λ is the second Lamẽ parameter, ρ is the density, ω is the excitation frequency, and **u** vector is the complex valued displacement vector computed during the solution of the forward problem. The nonlinear inversion involves the iterative minimization of the objective function[45]:

$$\Phi(\theta) = \sum_{i=1}^{N_m} \{(u_{m(i)} - u_{c(i)}(\theta))(u_{m(i)} - u_{c(i)}(\theta)) *\} \qquad (20)$$

Where $u_{m(i)}$ is the complex-valued amplitude of the i^{th} displacement measurement, $u_{c(i)}(\theta)$ is the analogous displacement calculated with the forward computational model based on the current estimates, θ, and N_m is the number of measurements. While the forward problem involves the calculation of $u_c(\theta)$, the inverse problem iteratively estimates the material properties that minimize (20). The forward problem requires a partial differential equation solution of (19), which requires boundary conditions in the form of the fixed displacement measurements that we can acquire anywhere in the tissue when we perform MRE. By using a subzone method where there is a grid of boundaries (fixed or sliding), we can acquire a well characterized solution using 15-20 nodes per wavelength.

As previously stated, MR measurements of harmonic motion during MRE involves recording displacements at a given number of phase offsets, and a sinusoid is then fitted to these temporal measurements using a discrete Fourier transform. The noise level of the MRE data can therefore be estimated by determining the mismatch between the fitted sinusoid and the displacement measurements.

We can do this by assuming that all components of the signal that are not the main harmonic Fourier component are due to noise. While estimating signal-to-noise ratio (SNR) based on motion alone is a valid method, calculating SNR based on strain rather than motion provides a reliable measure of the quality of MRE data due to the direct dependency of shear modulus on strain[46].

In general, Cauchy's symmetric strain tensor can be written as:

$$\vec{\varepsilon} = \begin{bmatrix} \varepsilon_{xx} & \varepsilon_{xy} & \varepsilon_{xz} \\ \varepsilon_{yx} & \varepsilon_{yy} & \varepsilon_{yz} \\ \varepsilon_{zx} & \varepsilon_{zy} & \varepsilon_{zz} \end{bmatrix} = \begin{bmatrix} \frac{du}{dx} & \frac{1}{2}\left(\frac{du}{dy} + \frac{dv}{dx}\right) & \frac{1}{2}\left(\frac{du}{dz} + \frac{dw}{dx}\right) \\ \frac{1}{2}\left(\frac{dv}{dx} + \frac{du}{dy}\right) & \frac{dv}{dy} & \frac{1}{2}\left(\frac{dv}{dz} + \frac{dw}{dy}\right) \\ \frac{1}{2}\left(\frac{du}{dz} + \frac{dw}{dx}\right) & \frac{1}{2}\left(\frac{dw}{dy} + \frac{dv}{dz}\right) & \frac{dw}{dz} \end{bmatrix} \quad (21)$$

Where u, v, and w are displacement in the x, y, and z directions respectively. From this tensor, we can calculate the octahedral shear strain (OSS, deviatoric component):

$$\varepsilon_s = \frac{2}{3}\sqrt{(\varepsilon_{xx} - \varepsilon_{yy})^2 + (\varepsilon_{xx} - \varepsilon_{zz})^2 + (\varepsilon_{yy} - \varepsilon_{zz})^2 + 6(\varepsilon_{xy}^2 + \varepsilon_{xz}^2 + \varepsilon_{yz}^2)} \quad (22)$$

Which is the maximum value of the shear strain in any plane. In harmonic motion of tissue, OSS over a cycle is periodic with a frequency twice that of the driving signal. In our OSS-SNR calculation, we perform a Fourier decomposition on the unwrapped phase difference to determine the amplitudes of the harmonic signal components. We then sum all harmonic components that are not the main harmonic and calculate strain components and OSS for the main harmonic components and the summed noise harmonic components individually. We can then calculate OSS-SNR using the ratio of OSS of the main harmonic component to OSS of the summed noise components. Typically, an average OSS-SNR of 3 or greater is considered acceptable for inversion.

2.4. MRI and MRE Sequences

In general, for MR pulse strategies, one cycle can be described as first excitation, then signal manipulation, and finally readout.[2] Excitation is transverse magnetization through radiofrequency (RF) pulses, including slice selection.[2] Signal manipulation can include additional RF pulses, gradients, or time delays. [2] Readout is the sampling of the MR signal, which can be done as a segmented image collection

where one line is recorded per excitation pulse or as the full image in a single-shot sequence.[2] While an RF pulse flips magnetization, the signal amplitude will decrease over time as dephasing occurs.[2] Pulses called spin-echoes and gradient-echoes can be used to reverse this dephasing.[2] A spin echo is a 180-degree RF pulse, while a gradient echo uses a pair of dephaser and rephaser gradients.[2]

Fast Low-Angle Shot (FLASH) is a segmented image acquisition sequence, meaning that it requires several excitation-readout cycles to obtain a full image.[2] Each repetition is one line in the image with a different phase encoding gradient on each repetition.[2] This sequence has very short echo times and a small flip angle, meaning only a fraction of the longitudinal magnetic field is flipped into the transverse plane, and a certain amount of the magnetic field flips back to the longitudinal plane between pulses.[2] This process removes most of the recovery time that is needed to flip the magnetic field back to the longitudinal plane, so image processing is faster.[2] This process also uses a gradient spoiling, which is when a magnetic field gradient pulse is applied to remove transverse magnetization by producing a rapid variation of its phase along the direction of the gradient. [2] A slice-select spoiler gradient with a different amplitude per repetition prevents the buildup of remaining transverse magnetization.[2]

For a FLASH MRE sequence, the motion encoding gradient (MEG) is located between the slice-select and phase-encoding gradients.[2] The acquisition loop consists of a trigger signal to the actuator to trigger vibration generation, followed by a set time delay, which is then preceded by the FLASH sequence with the MEG on a gradient axis.[2] After a series of acquisitions, the time delay is adjusted, and this acquisition loop is repeated.[2] This delay-repeat cycle is repeated until all phase propagation steps are acquired.[2] This full acquisition sequence is repeated with the MEG on the other two gradient axes to acquire different projections of the tissue displacement field.[2] The entire sequence is done with continuous vibration, needing only one trigger signal to the actuator.[2] Adding the MEG to the sequence prolongs the echo time and repetition time compared to the MRI FLASH sequence.[2] Increasing the repetition time allows for greater signal quality, however, it increases the acquisition time.[2]

Balanced Steady-State Free Precession (bSSFP) is another segmented image acquisition sequence.[2] The gradients of each axis are fully balanced for each loop iteration, so a spoiler gradient is not necessary.[2] The radiofrequency (RF) pulses are deployed so that the remaining longitudinal magnetization can contribute to the steady state precession.[2] If the RF pulses are in the same phase as the rotating reference frame and are orthogonal to the in-plane magnetization, each pulse both flips the longitudinal magnetization into the transverse plane and flips part of the transverse magnetization onto the negative longitudinal axis.[2] If the increase in transverse magnetization per RF pulse due to the longitudinal magnetization flipping to the transverse plane is larger than the decrease in transverse magnetization due to the flipping of transverse magnetization into the negative longitudinal axis, then the signal amplitude is larger than that produced by FLASH imaging.[2] However, if the pulses are not orthogonal to the transverse magnetization, the flipping effect has to be deconstructed into two components.[2] This then leads to complex magnetization patterns that will interfere with data acquisition, which shows up as a banding pattern.[2] When adding a MEG into the sequence, the signal generation is far more complex than that of FLASH or EPI MRE, so a modified bSSFP sequence is typically not used for MRE.[2]

Echo Planar Imaging (EPI) is a single-shot sequence that allows to the acquisition of a full 2D image with one RF excitation.[2] An oscillating readout gradient combined with short intermittent phase encoding gradient pulses to sample the image in a zigzag pattern.[2] EPI uses a 90-degree RF pulse followed by a refocusing pulse with a time delay.[2] The signal sampling starts right after the refocusing pulse that forms a spin echo.[2] Even though the magnetization takes time to return to the longitudinal state before the next flip, EPI is one of the fastest MRI techniques available.[2] Low spatial frequencies allow for maximum signal-to-noise-ratio (SNR).[2]

An MRE EPI sequence can be implemented as a gradient echo (GE) or spin echo (SE) technique.[2] The MEG can be inserted into the SE-EPI sequence by either being placed between the 90 and 180-degree refocusing pulses, which doesn't necessarily increase echo time or repetition time, or the MEG can be split in half and placed on either side of a single refocusing pulse, in which case the duration of the MEG dictates

how long the echo time is.[2] One disadvantage of using SE-EPI is that SNR can be decreased at higher field strengths due to increased field fluctuations when multiple lines of the signal are sampled in quick succession.[2] In general, the GE-EPI structure is much simpler than the SE-EPI structure.[2] There is only one possible location for the MEG (between the refocusing pulses), and it is implemented as a segmented acquisition sequence with a spoiler gradient at the end of the sequence to remove the in-plane magnetization in order for the following RF pulses do not generate undesirable echoes.[2] This extra gradient pulse and the fact that it is a segmented acquisition sequence means that GE-EPI is slower than the single-shot SE-EPI.[2]

Table 2.4.1. *Commonly used MRI sequences, advantages and disadvantages of using these sequences, their use in MRE, and advantages and disadvantages of using these altered sequences for MRE*[2]

Sequence	FLASH	bSSFP	EPI
MRI Theory	Flips a fraction of the longitudinal magnetic field while a certain amount relaxes back during each interval between pulses	Each pulse flips longitudinal magnetization to transverse plane and transverse to negative longitudinal axis	Oscillating readout gradient combined with a short-intermittent phase encoding gradient pulses, and signal sampling starts right after a refocusing pulse
Advantages	Removes recovery time, so image processing is faster	Signal amplitude larger than FLASH	One of the fastest MRI techniques available
Disadvantages	Potential buildup of transverse magnetization requires a spoiler gradient	If pules are not orthogonal to transverse magnetization, complex magnetization patterns interfere with data acquisition	Periphery sampled at lower amplitudes limiting SNR to a maximum value
Location of MEG	Between slice-select and phase-encoding gradients	Not typically used for MRE due to too high motion sensitivity and complex signal generation	Between two refocusing pulses OR split on either side of one refocusing pulse
Advantages	Can increase repetition time to allow for better signal quality	N/A	Faster acquisition, and sensitivity can be increased by slightly lengthening acquisition
Disadvantages	Longer acquisition time than FLASH due to delay and potentially increased repetition time	N/A	In SE-EPI, SNR can become decreased at higher field strengths. GE-EPI increases acquisition time.

Another MRE sequence specifically used in Johnson et al.'s studies is a specialized multi-shot spiral sequence. In this case, a spiral readout gradient instead of a symmetric readout gradient, such as those

in the above-mentioned sequences, allows for a shorter echo time.[17] In addition, the spiral readout allows for high resolution acquisition, as echo time is no longer dependent on resolution.[17] This sequence uses a multi-shot acquisition scheme because a single-shot approach would lead to long readout times in high-resolution acquisitions and distortions due to inhomogeneities in the static magnetic field.[17] While the most common sequence used in brain MRE acquisition is SE-EPI, Johnson *et al.*'s group uses this spiral readout sequence as faster alternative.

2.5. Benefits and Challenges in Moving to 7T

Conventional human MRI scanners have static magnetic fields of 1.5T or 3T, however, more recently the FDA approved 7T human scanners for clinical use. Compared to 3T scans, 7T has much greater sensitivity, and inherently increased signal to noise ratio (SNR) and spatial resolution[47]. Theoretically, SNR scales with field strength in MR imaging with the relationship $SNR \propto B_o$, and the resolution is approximately $1/n^{0.33}$ when B_o is increased by a factor of n[48]. The resolution can be even greater increased using different gradients and specialized sequences. However, despite the theoretical linear relationship between SNR and field strength, a linear increase is unattainable due to changing tissue relaxation and increased magnetic field inhomogeneities.

As stated before, interactions of a spin with its surroundings can changes the orientation of its magnetic moment. These magnetization vectors will therefore dephase over time, reducing the transverse magnetization. B_o inhomogeneities are also greater at higher magnetic field strengths, adding to this dephasing. Also, at higher magnetic field strengths, relaxation effects occur faster, resulting in a decreased apparent T_2 (T_2*) value[49]. For example, for the gray matter in the brain, while T_2* at 3T is 66ms, at 7T, T_2* is only 33.2ms[50]. For example, the scaling of T_2* for subcortical gray matter can be approximated as $T_2^* = 1/(7+3.5 \times B_o)$[51]. This causes a unique problem not addressed at conventional field strengths, and that is making the TE of a sequence close enough to the T_2 or T_2* value to preserve SNR and signal amplitude. Long echo times make a sequence more sensitive to signal relaxation, resulting in lower SNR. In general, for MRI sequences:

$$SNR \propto \sqrt{T_s} \cdot V \cdot \exp\left(-\frac{TE}{T_{relax}}\right) \qquad (23)$$

Where T_s is the sampling time, T_{relax} is T_2 or T_2*of the tissue of interest, and V is the volume of a single voxel[41]. The signal amplitude can be calculated as:

$$|S(TE)| = |S(0)| \cdot \exp\left(-\frac{TE}{T_{relax}}\right) \qquad (24)$$

Where |S(TE)| is the signal amplitude at echo time, and |S(0)| is the signal amplitude immediately after excitation[41]. Therefore, a larger TE compared to the relaxation constant results in both lower SNR and lower signal amplitude. However, in MRE, the length of the echo time is longer than most other MRI sequences in order to accommodate the MEG, leading to SNR and amplitude degradation in MRE more than other 7T sequences.

As for field inhomogeneities, B_o inhomogeneity directly scales with field strength, which leads to distortion in both the shape and intensity of images. This inhomogeneity reduces SNR but can be combatted using decreased voxel volumes, shimming (adding coils to make B_o more homogeneous), and collecting reference volumes in opposite phase encoding directions so the distortions are in opposite directions and can be filtered out[51]. B_1 inhomogeneity also increases with field strength[47]. As the B_o field increases, the B_1 operating wavelength gets closer to the diameter of the tissue of interest (in this case the human head)[49]. This results in decreased B_1 strength at the periphery of the tissue compared to the center, with peripheral B_1 being 42% lower than central B_1[49]. This leads to changes in contrast and signal drop-out across the image, and conventional pulse sequences are particularly susceptible to this B_1 inhomogeneity. To combat this, unconventional sequences, such as adiabatic pulse sequences, can be developed and used in place of the conventional pulse sequences[52], although no such specialized B_1 pulses have been used in MRE sequences.

Chapter 3: Design, Testing, and Implementation of MRE Actuators

3.1 Introduction

During MRE, mechanical waves generated by the mechanical actuator, usually transmitted in a burst of specified duration, must be synchronized with the MR signal excitation[39]. The vibration frequency, dependent on the application, is generally in the range of 40-120 Hz[39]. This actuator must be used in an ultra-high MR setting, so the tissue-contacting portion of the actuator must contain only ultra-high MR-safe materials. Common electromagnetic and piezoelectric actuators are inherently made of metals and may not be ultra-high field MR-safe. Specifically, electromagnetic actuators can cause electromagnetic interference during MR signal acquisition, while 7T-safe versions of piezoelectric actuators are cost-prohibitive and can cause distortions due to eddy currents. With a pneumatic design, the active metallic components can be stored in the equipment room, while all of the tissue-contacting components used in the scanner room can therefore be made entirely of plastics. However, both acoustic wave attenuation and synchronization with the scanner can present an issue with this type of design due to the time delay of the acoustic waveform moving from the active pneumatic driver to the end-effector.

In this Aim, we will build and validate two types of MRE actuators. In the first part of this Aim, we will design, build, and validate a 7T-compatible convertible pneumatic actuator to applying distributed vibration to both human and phantom. The phantom MRE will be used for amplitude, frequency, and sequence integration validation, as well as validation of the basic viscoelastic inversion algorithm use to calculate stiffness. Subsequently, 5-10 healthy human test MRE scans will be performed with the device to create the optimal end effector (pillow) design for both vibration application and patient comfort.

3.2 MRE Actuator Review

When performing MRE on any tissue type, harmonic vibration must be induced in the tissue in synchronization with the motion encoding gradient (MEG)[1,41]. This process requires a type of harmonic actuator that can be used to actuate tissue inside the MRI machine. Therefore, this actuator must be magnetic resonance (MR) compatible, or at least the part of the driver unit that is used inside the scanner room should be MR compatible. In general, there are three main categories of actuators. First, there are indirect actuators

that use an active driver outside of the scanner room and a passive driver inside the scanner[30,39,53–58]. In this type of actuator, usually pneumatic, an active driver that generates the vibration is placed in the control room as opposed to in the scanner room, and a passive driver is placed inside the scanner, in contact with the tissue of interest[30,39,53–58]. A long rod or tube is then used to transmit the vibration from the active driver to the passive driver[30,39,53–58]. The Resoundant, a pneumatic MRE device, is used by clinicians to diagnose liver fibrosis without a tissue biopsy [59]. The passive component of this device has also been altered in various studies investigating the human brain and phantoms[17,30,60,61]. To the best of our knowledge, this is the only commercially available MRE actuator and has been extensively tested in various studies across different organ systems[3,62]. The advantage of using a pneumatic actuator is that custom built versions are inexpensive and have a simple design, and pneumatic actuators in general allow for precise control with good MR compatibility of the passive driver[39]. However, these designs typically have phase lag and therefore difficulties in synchronization control due to the long transmission tubes or rods necessary to transmit vibration[63]. These are typically the designs used for brain MRE due to their versatility and ability to produce large enough actuation amplitude[16,30,54].

A second category of actuator takes advantage of the static magnetic field by using an electromagnetic coil/coil(s) to induce vibration. Current passing through an electromagnetic coil results in an oscillating magnetic field. Based on Lorentz Law, if the surface normal vector of the coil is perpendicular to the static magnetic field of the MRI machine, a rotary motion is generated[64]. This rotary motion is then transferred to the tissue using some type of vibration pad or bite-bar (for brain MRE)[64–69]. This type of design is inexpensive as well, and can be manufactured using standard metal machining equipment[3]. Also, a wide range of frequencies and displacements can be produced by changing the thickness of wire, amount of current, number of coils, and radius of coils[64]. However, this design is not commonly used anymore and, generally, the application of this design is limited due to the MRI safety challenges associated with its metallic structure. Two main drawbacks are also that the coil is mostly inflexible in terms of positioning, and the induced magnetic field can potentially cause artifacts in the image[3]. The third category of actuator

category uses an active vibrational component that directly interfaces with the tissue, as opposed to the previous two categories where the active component is a distance away from the tissue and relies on a rod, pad, or pillow to transmit vibration over a distance. For this type of actuator, the entire unit has to be MR compatible and small enough to attach to the tissue of interest. The units are usually driven by air pressure or piezoelectric crystals[70–80]. The main drawback for this type of device is that they are usually quite bulky and have difficulty in attaching to the tissue of interest[3]. Typically, this type of actuator, particularly the piezoelectric actuators, are more commonly used for MRE of small animals or phantoms [74–80].

Table 3.2.1. *Three main categories of actuators used in MRE, and their advantages and disadvantages*[1]

Actuator Type	Indirect Actuation	Electromagnetic Coil	Direct Actuation
Features	Actuator transmitted from system outside scanner room through pneumatic mechanism or long rod	Current passes through coil placed inside the scanner and rotary motion is induced	Actuation system near image of interest inside of scanner
Advantages	Simple and inexpensive design and allows for precise control with good MR compatibility	Inexpensive and simple design, and allows for wide range of frequencies and large displacements	End effector is fully MR compatible
Disadvantages	Phase lag and potential difficulties in synchronization control	Inflexible in terms of device position and can cause artifacts	Difficulty in attaching to tissue

The mechanical actuator used in the paper by Sack et al. 2008 used a commercial loudspeaker as an active driver with a carbon fiber rod coupled to the center of the flexible loudspeaker membrane.[6] The carbon fiber rod was attached to a pin joint on top of a passive driver head-rocker unit that would encircle the head of the patient or head phantom.[6] The loudspeaker was triggered to output at a specific frequency by a waveform generator, which was triggered in sequence with the MEG.[6] This active driver unit was placed outside the scanner room as the commercial loudspeaker and waveform generator are not MR compatible.[6] So, while this actuation setup was relatively inexpensive and had appropriate frequency ranges with acceptable displacements, the long rod (2-3m) induced phase lag in actuation leading to difficulty in synchronization.[6] This model of actuation is very common in performing MRE on brain tissue.

In Lewa et al.'s paper regarding MRE on a phantom gel, a commercial vibration unit was used to induce vibration in a plexiglass rod which transmitted the vibrations to the phantom.[10] Again, the active vibration unit was placed outside of the scanner room due to poor MR compatibility.[10] So, while the commercial vibration unit offered a large frequency range, the permanent magnet makes the unit inappropriate for use in an MRI machine.[10] Bishop et al. offered a design using a compression piston to convert rotary motion to linear motion in order to actuate a tissue/phantom with precise control and good MR compatibility.[11] However, this design had a limited frequency and amplitude range, so this type of actuator is not typically used in brain MRE.[11]

Another design using a loudspeaker as an active driver is seen in a study by Latta et al. Two active subwoofers that were modified with airtight acrylic lids were used as a source of air pressure.[12] Acoustic waves were delivered through tubes from the acrylic lids to passive drivers made from firm plastic containers.[12] The use of two loudspeakers and two plastic containers, one on either side of the head, produced a side-to-side rocking motion at varying frequencies.[12] The waveform generator driving the loudspeaker was triggered by the MRE pulse sequence, so this design allowed for good synchronization and therefore good potential for use as an actuator for brain MRE.[12] However, there was limited amplitude due to the compressibility of air and the size of the loudspeaker used.[12]

Feng et al. built a custom vibration control module consisting of a function generator and power amplifier.[13] The signal generator was triggered via the MR scanner to transmit current to an electromagnetic actuator.[13] The actuation unit comprised of a coil wired so its axial direction was perpendicular to the static magnetic field and a bar with a vibration pad to be adjust to the tissue of interest.[13] This design was used for a phantom gel, the brain, and the liver.[13] Benefits of this design include a simple deign, a wide range of frequencies, and a large range of displacements.[13] However, there were still limited placements because of necessary positioning of the coil and had the potential to induce artifacts due to the induced magnetic field.[13] A second design using an electromagnetic coil was implemented by Braun et al., where instead of using a pillow to induce actuation in a tissue, a bite-bar was used.[14] This design was specific to brain MRE and

featured the same easy synchronization as the other electromagnetic actuator design.[14] However, the bite bar limited how deeply the vibration penetrated the brain tissue, and again, potentially induced artifacts due to the induced magnetic field.[14]

A direct actuation approach was used by Tse et al., where a stack of piezoelectric disks was used to induce actuation.[15] The piezoelectric disks converted an electrical signal to mechanical actuation, and therefore had high accuracy, a fast response time, and were able to produce large forces.[15] However, piezoelectric crystals do not produce large displacements, which is why a long stack was needed.[15] Even with the large stack, the final tissue displacement was very small and therefore is not useful in brain MRE.[15] A novel design by Numano et al. also produced direct actuation of the tissue of interest through a rotational imbalance in a unit attached to the patient/phantom model.[16] Compressed air flowed through a tube connector to a chamber inside of the actuation unit.[16] This compressed air rotated a ball inside of this circular chamber, which induced vibration due to centrifugal force dependent on the weight and size of the internal ball.[16] An optical-fiber sensor sender/receiver used to track the motion of the ball was used to synchronize the vibration with the MRI machine.[16] This design is completely MR compatible, and the displacement and frequency can be changed with the weight of the ball, the size of the ball, and airflow.[16] However, there was difficulty in attaching this unit to the tissue of interest and therefore it would be difficult to use this design for brain MRE.[16]

Table 3.2.2. *Summary of MRE actuators and their advantages and disadvantages*

Actuator	Features	Advantages	Disadvantages
Loudspeaker with long transmission[6] (Sack et al. 2008)	Loudspeaker outside scanner room provides vibration to a passive driver inside scanner	Simple and inexpensive, frequency range appropriate for brain MRE	Phase lag in motion, difficulty in synchronization, high bandwidth difficult
Electromagnetic vibration generator[10] (Lewa et al. 2000)	Vibration generator placed outside scanner room, long plexiglass rod to transmit vibrations	Large range of potential frequencies, commercially available	Contains a permanent magnet, so bad MR compatibility
Ultrasound Motor[11] (Bishop et al. 2000)	Compression piston used to convert rotary motion to linear motion	Precise control, good MR compatibility	Limited frequency and amplitude range

Pneumatic Actuator[12] (Latta et al. 2011)	Active subwoofers with acrylic lids over speakers create source of air pressure and delivers acoustic wave vibrations through tubes	Function generator triggered by MRE pulse sequence, so good synchronization	Limited amplitude due to compressibility of air
Electromagnetic Coil[13] (Feng et al. 2018)	Torque acts on the coil of wire due to the static magnetic field, placed directly on the patient	Simple and inexpensive design, wide range of frequencies and displacements	Single direction of vibration, limited positioning, can induce artifacts
Electromagnetic Bite Bar[14] (Braun et al. 2014)	Similar design to electromagnetic actuator design, but uses a bite bar instead of vibration pad	Easy synchronization via function generator, design specific to brain MRE	Bite bar limits how deeply vibrations penetrate brain tissue
Piezoelectric Stack[15] (Tse et al. 2011)	Piezoelectric material converts electrical energy to mechanical motion and is placed directly on the patient	High accuracy, fast response, and high force production	Very small displacement, so a long stack is needed, which is why it isn't typically used in brain MRE
Air Ball-Actuator[16] (Numano et al. 2013)	Compressed air flows through the tube connector and rotates internal ball, centrifugal force generates vibration, optical-fiber sensor sender/receiver	Force can be changed with weight and dimensions of the ball, RPM controlled by airflow	Difficulty in securing connection to the tissue

3.3 Pneumatic Actuator Design and Testing

In MRE, mechanical waves generated by the actuator, usually transmitted in a burst of specified duration, must be synchronized with the MR signal excitation[39]. The vibration frequency, dependent on the application, is generally in the range of 40-120Hz. In order to perform MRE at 7T, however, a novel actuator that is ultra-high field compatible and approved needs to be developed and validated due to the size, material, and T2 relaxation constraints imposed by moving to 7T. Additionally, because the actuator must be used in an ultra-high field MR setting, the tissue-contacting portion of the actuator must contain only ultra-high MR-safe materials. Common electromagnetic and piezoelectric actuators are inherently made of metals and may not be ultra-high field MR-safe. Specifically, electromagnetic actuators can cause electromagnetic interference during MR signal acquisition, while 7T-safe versions of piezoelectric actuators are cost-prohibitive and can cause distortions due to eddy currents. With a pneumatic design, the active metallic components can be stored in the equipment room, while all the tissue contacting components

used in the scanner room can therefore be made entirely of plastics. However, both acoustic wave attenuation and synchronization with the scanner can present an issue with this type of design due to the time delay of the acoustic waveform moving from the active pneumatic driver to the end-effector. Therefore, the purpose of this sub-objective is to develop a 7T MR high field-compatible actuator for MRE data acquisition, quantify the frequency response of the actuator using laser doppler vibrometry, and perform 3T and 7T validation scans on a phantom of known mechanical properties and the human brain. This MRE actuator can be used at multiple field strengths to provide distributed vibration at the surface of the phantom or human brain, but the end effect is able to be modified for various tissue types.

Figure 3.3.1. *a)3000W Class-D Amplifier on top of the modified subwoofer, and b) high air pressure tubing carrying air pressure waves from the modified subwoofer cone encased in acrylic.*

The original proposed pneumatic actuator design consists of a modified dual 12” cone subwoofer (MTX 1200 W max, 2 Ohm impedance) as an active driver to provide harmonic vibration in the form of pressure waves through flexible PVC tubing (1” ID, 1-¼” OD) to a pillow-like passive driver as the tissue-contacting end effector. Both cones have acrylic sheets mounted to the front with custom hose attachments to direct the acoustic haves into the tubing and to the passive driver. The original passive driver is constructed from heat-sealed polyurethane and compressible foam. The modified subwoofer is driven by a function generator (RIGOL DG-1022) through a Class-D audio amplifier (300W), which provides a harmonic signal to the active driver (Figure 3.3.1). A TTL signal is output from the MRI scanner prior to each acquisition cycle to the function generator, which triggers the function generator to output the specified harmonic signal to the subwoofer, ensuring that the vibration is in sync with the MRE sequence.

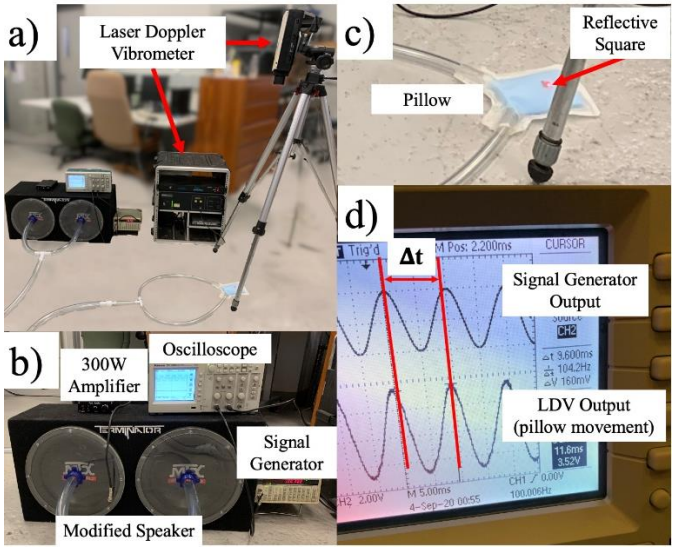

Figure 3.3.2. *a) Full laser doppler vibrometry setup for frequency response testing of the original MRE actuator design, b) the actuator full active driver setup with labeled components, c) the pillow and reflective square for measuring end effector vibration, and d) messing the amplitude and time delay between signal output and pillow vibration.*

To both evaluate the vibration amplitude and to address the time delay from the active driver to the passive driver and the frequency response of the actuator, a laser doppler vibrometer (LDV) was used to capture the harmonic motion of the passive driver (Figure 3.3.2a,b). A small square of reflective material was attached to the center of the passive driver, and the laser was aligned with the square (Figure 3.3.2c). Both the output of the LDV and the signal generator driving the modified subwoofer were visualized in an oscilloscope, and both the amplitude of vibration of the pillow and the time delay (ms) between the peaks were measured for driving frequencies 50-100 Hz (5 Hz increments) (Figure 3.3.2d). These data were then phase-unwrapped, and a linear regression was developed to qualify the time delay as a function of driving frequency to be used in that driving frequency range[37].

Following the results of the initial validation tests, multiple changes were made to the actuator setup. First, the 300 W amplifier was replaced with a 3000 W amplifier to directly increase vibration amplitude. Next, the soft PVC tubing was replaced with harder, high pressure rubber tubing of smaller diameter (¾" ID) to reduce vibration dampening from the output of the subwoofer cone to the end-effector.

Additionally, Y- and T-connectors for the tubing were found to greatly contribute to the vibration dampening, so only one speaker cone was used to provide vibration instead of two.

3.3.1 3T and 7T Phantom MRE Validation

This new configuration was validated during multiple phantom test scans at both 3T and 7T. To validate that the actuator functioned as intended during MRE, a custom silicone MRE phantom (CIRS 049) of dimensions 21.0 × 15.0 × 10.7 cm was acquired with a background young's modulus of 5±1 kPa (1.67±0.33 kPa shear modulus) and spherical inclusions of 3±1 kPa, 8±1.5 kP a, 12±2 kPa, and 20±2 kPa (1±0.33 kPa, 2.67±0.5 kPa, 4±0.67 kPa, and 6.67±0.67 kPa shear modulus respectively). 3T MRE scan was performed using the original end effector, with 2.5 mm isotropic resolution and 48 slices at 50 Hz vibration frequency. This was performed inside of a 3T Siemens Skyra scanner with a 16-channel head coil (Siemens Healthineers). Experiments were also performed on a 7T whole-body MRI scanner (Magnetom 7T, Siemens Healthineers, Germany) equipped with a 70 mT/m gradient coil and a 32-channel head coil (Nova Medical, Wakefield, MA). The modified single-shot multi-slice spin-echo 2D-EPI based sequence (Fig. 3.3.1.2) was designed to acquire MRE data using phase shifted bipolar or trapezoidal flow-compensated motion-encoding gradients (MEGs) synchronized with the acoustic actuator by TTL triggering. The imaging parameters were optimized for 1.1mm isotropic resolution and allowed to acquire 40 transversal slices covering the superior part of the brain with a matrix size of 210 × 210, echo spacing 0.83 msec, in-plane acceleration GRAPPA=3, TE=65 msec, TR=5600 msec and anterior to posterior (A-P) phase-encoding direction. MRE imaging was performed at 50Hz vibration frequency with eight acquisitions or phase offsets over one wave cycle and three orthogonal motion encoding gradients[36].

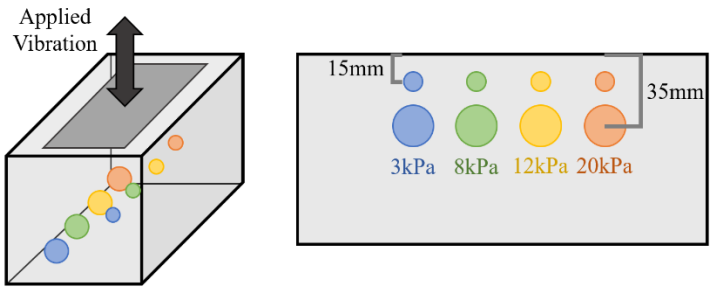

Figure 3.3.1.1: *Custom CIRS 049 Phantom with inclusions of 10mm and 20mm diameter. Vibration of specified amplitude and frequency is applied to the top surface of the phantom as shown on the left*

The same CIRS phantom was then scanned using this 50 Hz MRE protocol at 2.5 mm, 1.7 mm, 1.3 mm, and 1.1 mm resolutions. This data set was used to quantitatively compare stiffnesses between resolutions and field strengths. Additionally, because filtering parameters can have an effect on stiffness, this data set was used to determine appropriate filtering parameters for these resolutions, as wider filter windows are required for higher resolution scans to overcome increasing shear wave phase mismatch between slices. Maps of the absolute value of the complex shear modulus (|G*|) of the phantom's cross section were obtained using an in-house direction inversion algorithm using equations (17) and (18), and the mean of each |G*| map of five homogeneous slices per scan (2.5 mm at 3T, and 2.5 mm, 1.7 mm, 1.3 mm, and 1.1 mm at 7T) were compared both visually and using a one-way ANOVA with a post-hoc Tukey test to compare between these five groups. Due to plans to use this MRE actuator at multiple frequencies, we performed MRE on the same CIRS phantom, collecting 40 slices at 1.1 mm isotropic resolution with a GRAPPA of 3 and 8 phase offsets. These experiments were performed at 30-80 Hz at 10 Hz intervals with the parameters as shown in Table 3.3.1.1.

Table 3.3.1.1: *MRE Parameters for Each Frequency*

Frequency (Hz)	Echo Time (TE, ms)	Total TR for 40 Slices (ms)	Vibration Cycles/TR
30	90	6667	5
40	74	6000	6
50	65	5600	7
60	65	6000	9
70	65	5715	10
80	65	5500	11

For processing MRE acquisitions, the difference was taken between two phase images acquired with opposite encoding directions, and the phase difference images were then curl filtered to remove the longitudinal wave component. We then performed a Fourier decomposition to extract the main harmonic, and we applied a quartic smoothing kerned with the kerned window scaled based on resolution, previously validated with phantom studies. Finally, we calculated loss and storage modulus (elastograms) using the in-house direct inversion methods using equations (17) and (18).

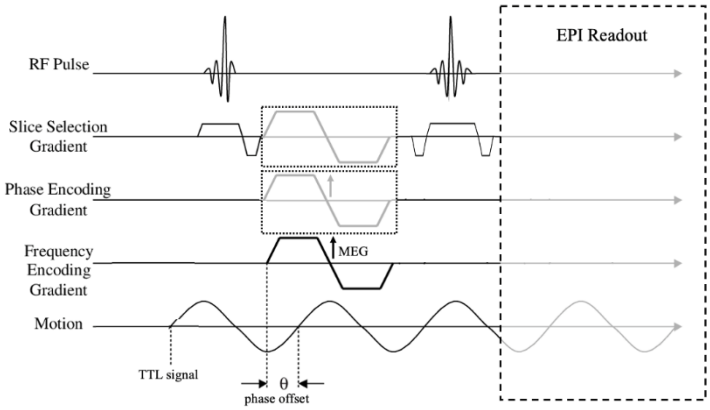

Figure 3.3.1.2: *Custom single-shot multi-slice spin-echo 2D-EPI based 7T MRE sequence with 3-D motion encoding gradients (MEGs)*

3.3.2 Human MRE Validation

The human end-effector design was also modified multiple times to provide higher vibration amplitudes, as well as subject comfort, as the initial design compressed under the weight of the subject's head and did not provide sufficient vibration. MRE was performed at both 3T and 7T on multiple human subject to investigate the different human brain end effectors. The new human end-effector designs were 3-D printed using TPU filament material. Multiple pillow designs were manufactured and tested for both effective, even, vibration application and patient comfort, resulting in the final design that matches the shape of the head coil without any sharp ridges, and thin enough to allow us to scan a diverse patient population (Figure 3.4.2.1). The size and shape are dependent on the head coil, and due to challenges with the head coil size at 7T MRI scanners, our pillow design required several iterations, but the same design

issues arise for many multi-channel head coils. The initial pillow design did not provide sufficient vibration, while the second pillow design provided enough vibration but was not comfortable to lay on for the duration of the scan. The third pillow design also provided sufficient vibration but was not fully comfortable due to the ridge in the back. This design was also too thick to allow us to scan a diverse patient population. The fourth design initially did not provide sufficient vibration due to the pillow compressing under the weight of the head, however, by adding soft supports to the inside of the pillow where the head rests, the pillow was both comfortable and provided sufficient vibration. Due to concerns about uneven application of vibration, a modification to the inlet to make it central resulted in the final pillow design.

Using the final end-effector and the same 7T scanner and head coil as previously described, we performed full and partial brain coverage MRE on 3 subjects over 7 scanning sessions at 50Hz with TR/slice=140 ms and TE=65 ms at 2.5 mm (n=1, GRAPPA=2), 1.7 mm (n=1, GRAPPA=2), 1.3 mm (n=3, GRAPPA=3), and 1.1 mm (n=6, GRAPPA=3, Partial Fourier=7/8) isotropic resolutions and 8 phase offsets. We also performed full brain coverage MRE on the same 3 subjects at 2.5 mm isotropic resolution at 50 Hz using a 64-channel head coil on a 3T Siemens Prisma scanner (TE = 70 ms, TR = 5600 ms). These experiments were not only used to validate the MRE actuator, but also preliminarily validate our sequence parameters, the move from 3T to 7T, and our post-processing procedure on the human brain. This data was also used to determine areas for improvement for our post-processing procedure. We also performed preliminary testing at 40, 60, and 80 Hz on one healthy human subject using the same 7T scanner and head coil as previously described, the same MRE parameters listed in Table 3.3.1.1, and using the finalized custom pneumatic actuator. All data were processed using the in-house direct inversion method described in the previous section.

3.4 Pneumatic Actuator Results and Discussion

3.4.1 Phantom Results and Discussion

The linear regression developed from the LDV testing (Fig. 3.4.1.1) to calculate time delay from trigger signal to pillow movement, where f is the driving frequency and n is any positive integer as shown in equation 1. The R^2 value of this linear regression is 0.9986. The peak-to-peak amplitude of the initial

actuator design ranged from 0.6 mm to 0.3 mm dependent on the frequency of actuation. Shear wave propagation from the initial MRE scan at 3T is shown in Figure 3.4.2.1 in units of mm/mm.

$$time\ delay = \frac{0.3565f - 29.882}{2\pi f} - \frac{n}{f} \qquad (25)$$

These initial MRE results as well as the amplitude measurements from the LDV study prompted the switch to both the more powerful 3000W amplifier and to the new tubing and end-effector design(s).

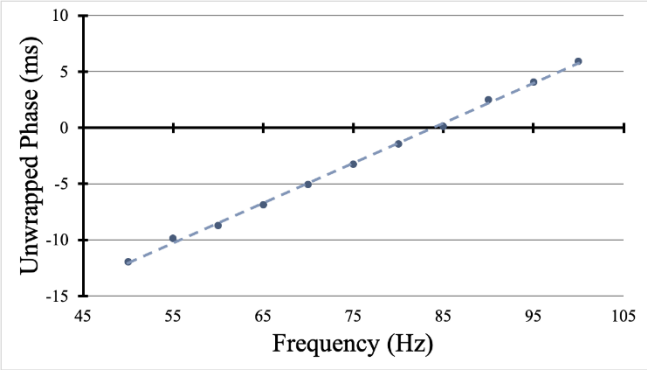

Figure 3.4.1.1: *LDV testing time delay linear regression*

Using the results from the second 3T MRE scan (at 2.5 mm resolution) that utilized the 3000 W amplifier and the original end effector design, the average |G*| estimates of the background of the phantom (measuring five homogeneous slices) is 1.430±0.023 kPa (Figure 3.4.1.2). This shear stiffness value is within the specification range given by the phantom's data sheet (1.333-2.000 kPa), therefore validating the MRE procedure (actuator and post-processing) at 3T. Evaluating the 50 Hz 7T MRE phantom scan results (Figure 3.4.1.2 and 3.4.1.3), the average |G*| estimates of the background of the phantom (measuring five homogeneous slices) were 1.425±0.006 kPa, 1.427±0.004 kPa, 1.430±0.004 kPa, and 1.423±0.010 kPa at 2.5 mm, 1.7 mm, 1.3 mm, and 1.1 mm respectively. All of these are within the specification range of the custom phantom, and comparing the five data sets each with n=5 samples, there was no significant difference found between any of the pairs of data sets ($p>0.50$). This would indicate that in a homogeneous, linear, material, changing neither field strength nor resolution inherently changes the calculated stiffness of the material being imaged with sufficient OSS-SNR (all values above 95, much greater than the accepted

threshold value). This investigation also allowed for the selection of appropriate filtering parameters used for the preliminary 7T human MRE scans.

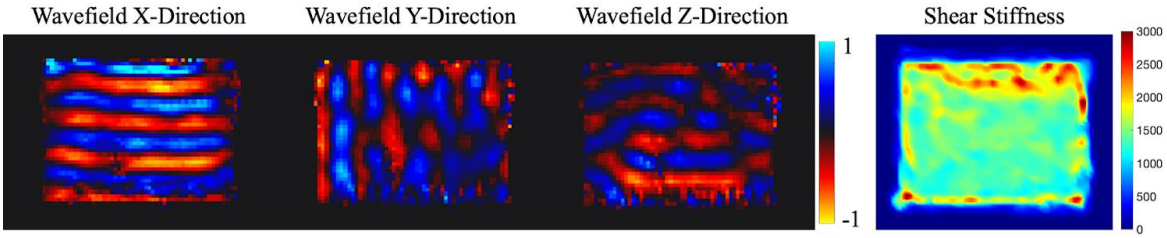

Figure 3.4.1.2: *3T MRE on silicone phantom showing wavefield propagation in each direction in mm/mm, and |G*| in Pascals*

Shear stiffness maps were successfully calculated for phantom MRE scans at all frequencies using a custom pneumatic actuator and custom 7T MRE sequence. Using a higher frequency was able to discern more detail in the custom phantom, specifically the stiff spherical inclusions (outlined in pink in Figure 3.4.1.3). All calculated |G*| values are within the specification range of the custom phantom, which would be a shear stiffness between 1.333-2.000 kPa. This data was also used to determine the filter window necessary for quartic smoothing kernel at each frequency, as this must be scaled for wavelength to prevent over-smoothening of short wavelength waves. Comparing all data sets each with n=5 samples, there was no significant difference found between any of the pairs of data sets ($p>0.50$). This would indicate that in a homogeneous and linearly elastic material, vibration frequency does not inherently change the calculated |G*| of the material being imaged. Wavefield images shown at 1.1 mm resolution at all tested frequencies are shown in Figure 3.4.1.3.

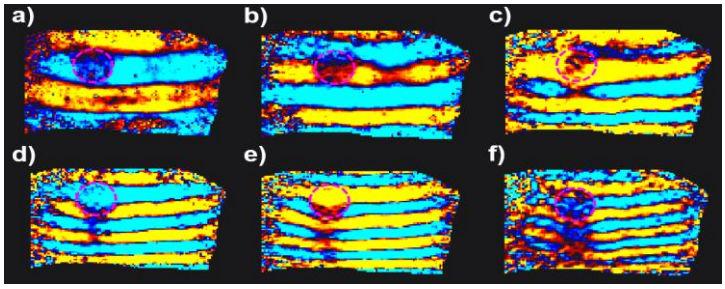

Figure 3.4.1.3: *Wavefield in the x-Direction in a Central Slice of the Phantom at Each Frequency a)30 Hz, b)40 Hz, c)50 Hz, d)60 Hz, e)70 Hz, and f)8 0Hz, Where the Pink Outline is the Location of a Stiff Inclusion*

3.4.2. Human Results and Discussion

Wave propagation in the brain was visualized with all but the first pillow design. The second two end effector designs, however, were rejected due to patient discomfort despite the acceptable wave propagation. The final end effector design was chosen over the second to last due to the single sided inlet design resulting in a lack of symmetrical wave propagation. These wavefields are shown in Figure 3.4.2.1, along with the end-effector that resulted in said wavefield. This pneumatic actuator with the final human brain end effector was therefore used in all other MRE investigations in this work involving MRE of the human brain.

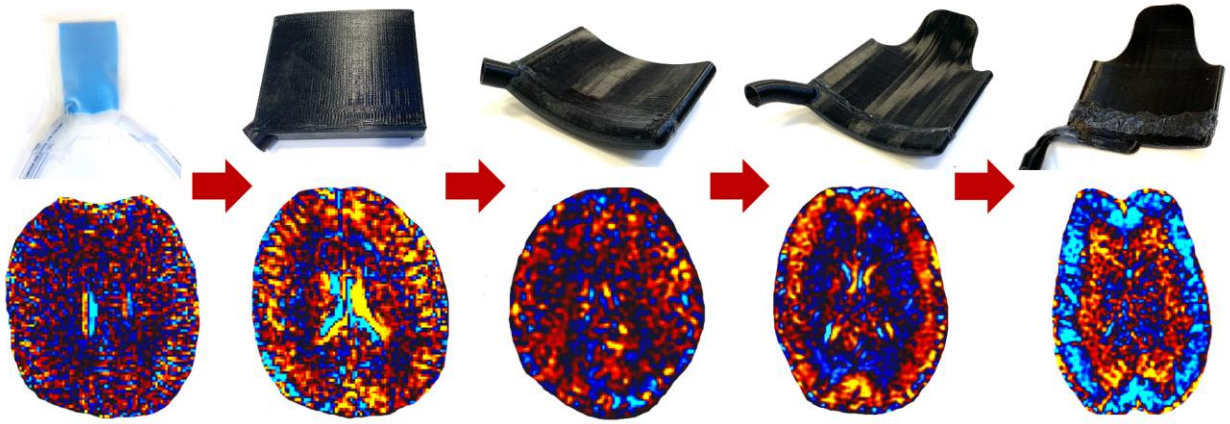

Figure 3.4.2.1. *Progression of MRE End Effector Development and Resulting Brain Wavefields*

Using the finalized MRE actuator and human end-effector design, we successfully calculated |G*| of the human brain at multiple resolutions, and at both 3T and 7T (Figure 3.4.2.2)[31]. However, unlike the phantom results, changing resolution does change the apparent |G*| with a pattern that suggests a relationship to OSS-SNR. With increasing resolution, the OSS-SNR decreases (with no apparent difference between matched resolution 3T and 7T), as does apparent complex shear modulus. The average whole-brain |G*| values were 1.994±0.082 kPa, 2.201 kPa, 2.219 kPa, 1.786±0.125 kPa, and 1.757±0.183 kPa for 3T at 2.5mm resolution, 7T 2.5 mm, 1.7 mm, 1.3 mm, and 1.1 mm isotropic resolutions respectively, while the average whole-brain OSS-SNR values were 28.477±4.479, 28.277, 20.916, 8.093±1.412, and 5.121±0.801 for 3T at 2.5 mm resolution, 7T 2.5 mm, 1.7 mm, 1.3 mm, and 1.1 mm isotropic resolutions respectively.

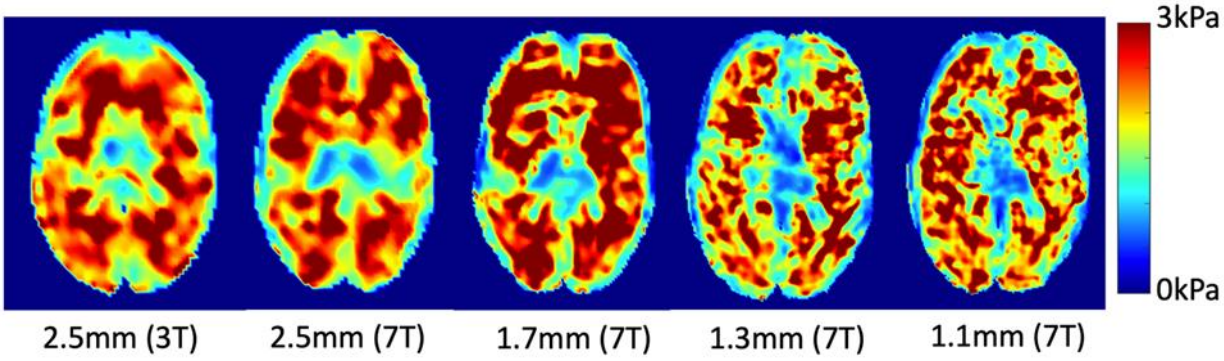

Figure 3.4.2.2: *|G*| (kPa) Shown across all representative resolutions and field strengths in the same healthy human subject at a representative central slice*

While no conclusions can be drawn using this preliminary data, further investigation into these trends is warranted. Additionally, advanced reconstruction and denoising techniques are also necessary to not only investigate this trend, but also increase accuracy at high resolutions. Not only is there higher thermal and gaussian noise at higher resolutions in 7T scans, there are also artifacts present due to scanner reconstruction error around phase wrapping lines. This cannot be corrected with denoising or filtering techniques and requires post-hoc reconstruction from the raw scanner data.

Wavefield images (Figure 3.4.2.3) and |G*| maps were also successfully generated from our preliminary 40, 60, and 80 Hz human MRE scans at 1.1 mm resolution. The results from our initial multifrequency pilot scan match the known frequency dependent (shear stiffening) behavior of the human brain[7]. More work needs to be done, however, at ensuring that vibration amplitude is the same at all frequencies, as increasing frequency decreases both wave amplitude in the end effector and penetration through the skull. This preliminary data also suffers from the same noise and scanner error concerns as the 50 Hz 1.1 mm resolution data, and the same corrections will be performed to future multifrequency data as will be validated in 50 Hz data.

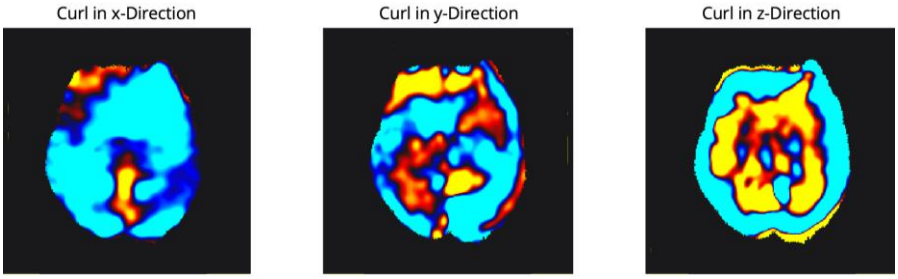

Figure 3.4.2.3: *Smoothed wavefields in a central slice of the human brain at 40Hz*

3.5 Pneumatic Actuator Alternate Case Study: 3T MRE of the Human Lumbar Intervertebral Disc

3.5.1 Introduction

Chronic low back pain is the most common cause of disability in adults between 45 and 65 years old, affecting 70-85% of individuals over the course of their lifetime[81]. Isolating a single cause is difficult, and multiple factors may contribute to the pain, such as degenerative disc disease (DDD), facet arthropathy, disc herniation, spondylolysis, and muscle stiffness[81]. Specifically, intervertebral disc degeneration (IDD) is a common disorder that usually leads to pain and spine dysfunction, and can be caused by acute overloading or long-term repetitive intervertebral disc (IVD) mistreatment [81,82]. As the disease progresses, the loss of disc integrity and shock absorption is thought to increase biomechanical stresses on facet joints, leading to heightened pain and dysfunction.

Early detection of disc degeneration is critical for symptom management and preventative measures, as IDD can progress through physiological and morphological changes, resulting in alterations in tissue mechanical properties. However, early detection has been challenging, however, due to limited success in finding *in-vivo* imaging biomarkers for early stages of degeneration[83]. Additionally, the presence or severity of back pain does not necessarily correlate with degenerative change seen radiographically[84]. Despite this, several magnetic resonance imaging (MRI) changes have been found to be helpful in prediction of disc-related back pain, making MRI the most commonly used imaging modality for the diagnosis of DDD and IDD. The current standard MRI protocol for DDD/IDD detection usually includes 2D T1-weighted and T2-weighted structural images, as well as a short tau inversion recovery (STIR) sequence, a gradient echo sequence (particularly in the cervical spine), and coronal proton density-weighted [81]. Disc degeneration on

MRI shows as a loss of T2-weighted intensity and loss of disc height. It is currently classified into 'Pfirrmann' stages based on disc structure, height, and loss of distinction between the nucleus pulposus and annulus fibrosus[85]. While this imaging biomarker is noninvasive and can image internal morphology of the IVD, it has been reported to have both low sensitivity and high false-positive and false-negative rates[86].

Because the physiological and morphological changes resulting from disc degeneration leads to alterations in the tissue's mechanical properties, magnetic resonance elastography (MRE) may be a promising imaging tool for the detection of IDD. Because human tissue is viscoelastic, the mechanical response of tissue is dependent on loading speed, or in the case of MRE, the frequency of actuation. Therefore, some studies use multifrequency MRE, in which the vibration is applied and encoded at different frequencies to determine the viscoelasticity[7,23,63,79,87]. The aim of this ssection is to perform multifrequency MRE on a pilot cohort to determine the frequency-dependent properties of the intervertebral disc, and to determine a relevant viscoelastic material model to determine frequency-independent parameters.

3.5.2 Methods

One scanning session was conducted on a 3T Siemens Prisma (Siemens Healthineers) using the integrated lumbar body coil was performed on six healthy volunteers (Avg. Age 25.5 ± 3.9 years). One additional volunteer (Age 28 years) with no current pain or ongoing treatment, but with a history of a discectomy, which is a surgery to remove a damaged part of an IVD, on the disc between L4 and L5 (Fig. 3.5.3.2) was also scanned.

Subjects were positioned supine with legs elevated on a pad to relax the lower back muscles. The end effector of a custom pneumatic actuator, as described earlier and in Triolo, *et al*.[31], was placed under the lower back of the volunteer, with the volunteer's body weight holding the end effector in position throughout the scan (Fig. 3.5.2.1). Vibration was applied in sync with the MRE sequences though triggering at the beginning of each TE, and at the frequency specified in the MRE sequence (50, 80, or 100 Hz). Unlike previous investigations [88], applying vibration using a pneumatic actuator allows for supine positioning of

the eliminating the complications that result from spinal imaging of a prone volunteer during free breathing (*i.e.*, the rise and fall of the spine) or the discomfort of breath-holds during a lengthy sequence.

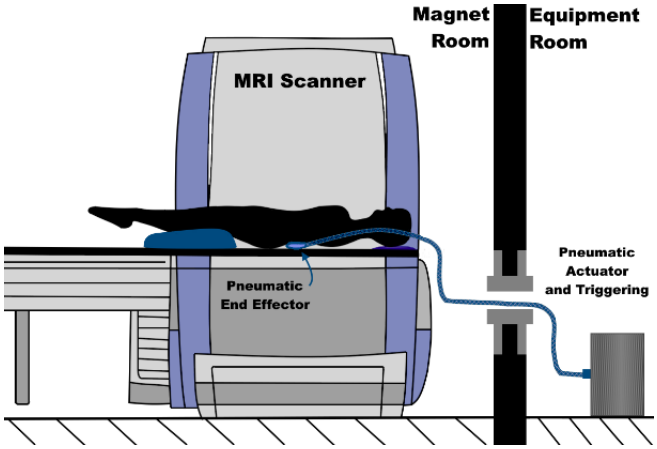

Figure 3.5.2.1. Schematic of MRE actuator and volunteer positioning *inside the MRI scanner. Air pressure waves are generated by the active components outside the magnet room and pushed through semi-flexible tubing into a 3D printed TPU end effector placed under the volunteer's lower back.*

A sagittal T2-weighted structural scan was performed first (TE = 95 ms, TR = 3500 ms, 0.677 × 0.677 × 4.800 mm resolution). Subsequently, three frequencies of MRE (50, 80, and 100 Hz, 1.7 mm isotropic resolution, Table 3.5.2.1) were performed using an echo planar spin echo 2D-multislice pulse sequence with spiral readouts [89] (axial slice positioning) to investigate the mechanical properties of the IVDs between L3 and L4, and L4 and L5.

Table 3.5.2.1. *MRE Sequence Parameters*

Frequency	**Scanning Parameters**		
	TE (ms)	***TR (ms)***	***GRAPPA***
50 Hz	83 ms	5600 ms	3
80 Hz	65 ms	4522 ms	3
100 Hz	58 ms	5800 ms	3

After acquisition, we employed a Marchenko-Pastur Principal Component Analysis (MP-PCA) denoising algorithm to both the magnitude and phase image set using a 5 × 5 × 5 sliding block to reduce thermal and spatially varying noise. Then, we obtained the difference between two phase images acquired with opposite encoding directions. The resulting phase difference images underwent curl filtering to remove the

longitudinal wave component (Fig. 3.5.2.2). We then performed a Fourier decomposition to extract the main harmonic, and we applied a quartic smoothing kernel with the kernel window scaled based on resolution, previously validated with phantom studies. Finally, we calculated the magnitude of the complex shear modulus (|G*|) using the previously-described in-house direct inversion method using Equations (17) and (18) [90].

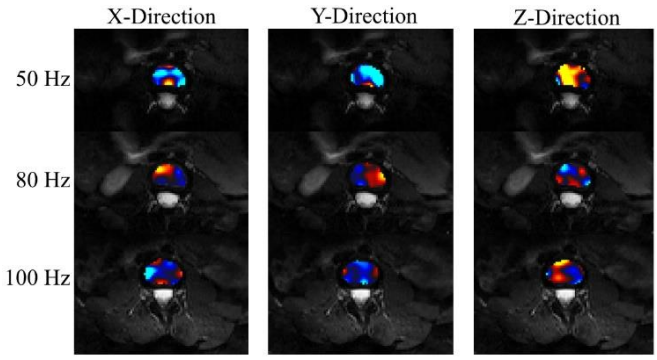

Figure 3.5.2.2. Curl filtered wavefield images *masked to the IVD at each vibration frequency and in each motion direction during MRE acquisition (normalized units, mm/mm).*

We also calculated OSS-SNR for each image series to ensure that the images exceeded the threshold for accurate viscoelastic inversion (OSS-SNR > 3.0) [91]. To achieve this, we used the displacement as calculated during Algebraic Inversion processing (SEGUE unwrapped phase multiplied by the motion encoding scaling factor) before using Fourier decomposition to extract the different harmonic displacements. We then calculated Octahedral Shear Strain (OSS) of only the main harmonic component and the OSS of the sum of the other harmonic components. The ratio of the main harmonic component OSS to the OSS of the other harmonics is used as the OSS-SNR of the scan and data processing method. Masks for each IVD were manually segmented using the MRE magnitude images and T2-weighted structural image. These masks were used to segment elastograms and OSS-SNR to calculate the average |G*| in each disc at each frequency.

To determine the frequency independent parameters of the IVD, we employed four linear, viscoelastic models to understand which model would best approximate the behavior of the IVD [7]. We performed spatial averaging of the loss and storage modulus over each IVD for each subject at all three frequencies and

performed optimization to calculate the frequency-independent parameters using the storage and loss modulus averages from the six healthy individuals.

3.5.3 Results

We successfully performed multifrequency MRE of the lumbar IVDs in seven human volunteers. Despite the usual drop-off in vibration amplitude with increasing frequency, the data exceeded the OSS-SNR threshold for accurate viscoelastic inversion in the IVDs of all subjects at all frequencies of actuation. The average |G*| in the IVDs of the six healthy volunteers at each frequency were calculated and are shown in Table 3.5.3.1, and are depicted as a function of frequency with a comparison to the subject with the history of a discectomy in Figs. 3.5.3.1 and 3.5.4.1. As has been observed in most human tissue, the apparent |G*| in the IVD increases with vibration frequency. The average |G*| of the healthy IVD here is in a similar range as a previous investigation with similar vibration frequencies [92]. We can also observe that the |G*| of the IVD between L3 and L4 is slightly stiffer than the IVD between L4 and L5.

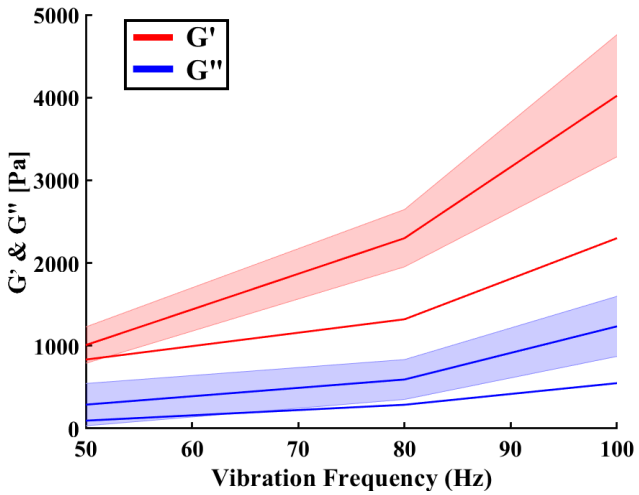

Figure 3.5.3.1. Average frequency dependent G' (red) and G" (blue) *in the IVDs between L4 and L5 in the six healthy volunteers (with shaded error bars) and the one volunteer with a history of a discectomy (line only).*

From Figs. 3.5.3.1. and 3.5.3.2, we see that the IVD with degeneration has a lower |G*|, G', and G" than a healthy IVD. The IVD with degeneration also appears compressed, shown in the T2-weighted structural scan (Figure 3.5.3.2). The difference in |G*|, G', and G" between a healthy and degenerated disc also widens with increasing frequency, so we therefore attempted to determine a frequency-independent mechanical

property to best describe the healthy IVD, as we expect the frequency-independent properties of the IVD to be altered during disc degeneration.

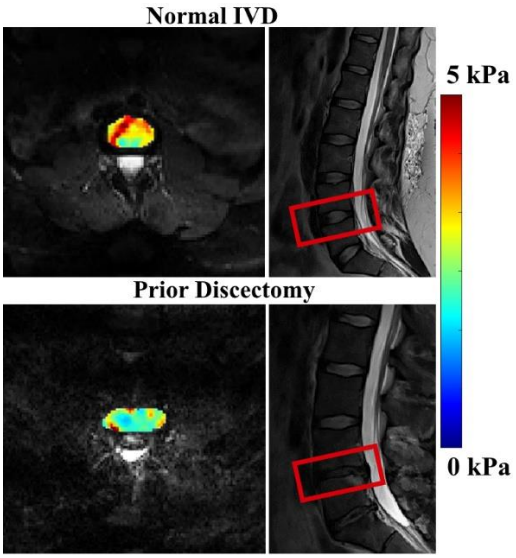

Figure 3.5.3.2. *|G*| at 100Hz in a healthy IVD (top) and an IVD with degeneration from a prior discectomy (bottom), location shown in red on the associated Sagittal T2-weighted structural scan.*

Table 3.5.3.1. *Average |G*| Across Healthy Subjects*

IVD	Average |G*|		
	50 Hz	***80 Hz***	***100 Hz***
L3-L4	1.43 ± 0.39 kPa	4.19 ± 0.63 kPa	6.20 ± 1.60 kPa
L4-L5	1.28 ± 0.50 kPa	2.78 ± 0.53 kPa	5.15 ± 1.10 kPa
Discectomy[a]	0.88 kPa	1.43 kPa	2.58 kPa

[a.] Average |G*| in only one subject with history of discectomy in L4-L5 IVD

3.5.4 Discussion

In this study, we obtained *in-vivo* measurements of the human IVD's mechanical response at multiple frequencies ranging from 50 to 100 Hz. Our findings show that the Zener model may best represent the IVD's frequency-dependent mechanical response, with a μ_1 of 1800 ± 213 Pa, μ_2 of 3186 ± 1116 Pa, and η of 4.61 ± 1.23 Pa·s. While we only have one subject with disc degeneration, we expect these frequency-independent material properties to change over the course of disc degeneration. While there has been previous evidence in the literature regarding the clinical advantage of using a multifrequency MRE protocol on various other human tissues, this is the first investigation applying this principle to the intervertebral disc.

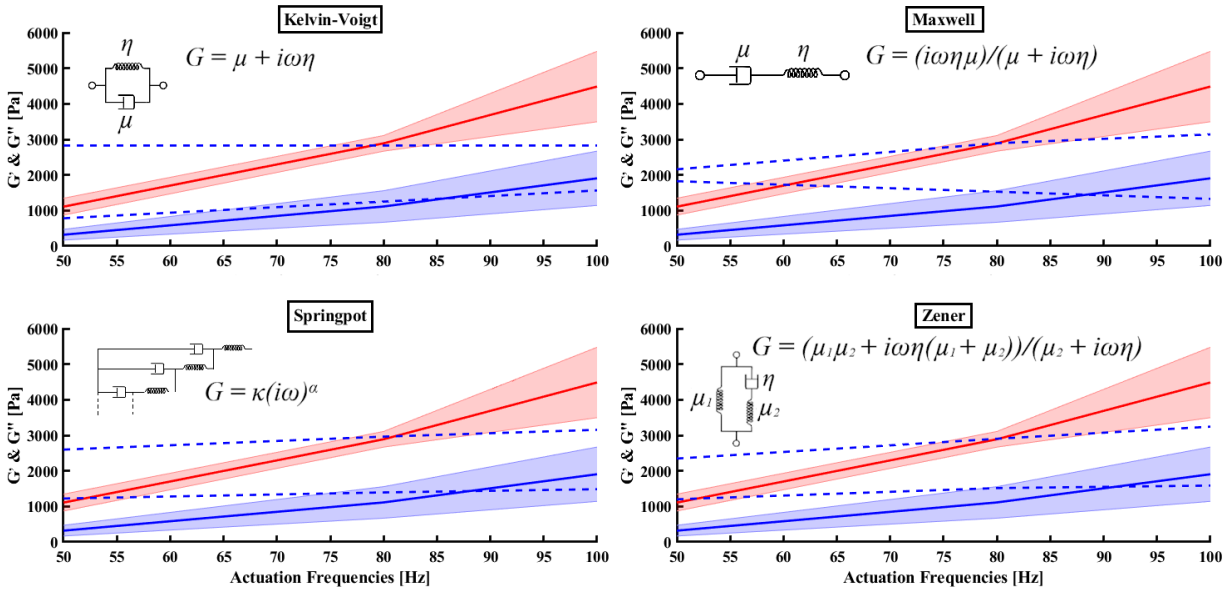

Figure 3.5.4.1. Linear viscoelastic material model fits *for G' (red) and G" (blue) for the IVD between the L3 and L4*

Additionally, due to the application of mechanical vibration in a distributed manner to the lumbar region of the lower back, this technique and hardware setup has the potential to be utilized to investigate the mechanical properties of multiple lumbar structures simultaneously. As stated previously, the cause of chronic back pain is difficult to isolate to a single cause and may even been due to multiple factors. For example, lumbar back pain specifically may be caused by changes in lumbar muscle stiffness. The shear waves generated by the pneumatic actuator are distributed and have a high enough amplitude to penetrate the IVD and the surrounding musculature at the same time. This therefore would allow for the investigation of the mechanical properties of multiple structures concurrently, potentially allowing for better pinpointing the cause(s) of back pain with a short, non-invasive, scanning session.

One limitation of this study was that the frequency range was low for the size of the target tissue. 50 Hz is a relatively long wavelength for the size of the IVD, so it may be useful in the future to extend the multifrequency range to higher frequencies for investigating the IVD. A larger number of frequencies in the imaging protocol would also help in the accuracy of our mechanical model optimization problem. Additionally, this pilot study had a small sample size, and a larger number of volunteers should be recruited

for more accurate material modeling of healthy IVD, and to better determine the difference between degenerated and healthy IVD. Ideally, we would also recruit subjects with varying stages of IDD or DDD as specified by Pfirrmann, *et al.* [85]

3.8 Conclusion

A custom pneumatic MRE actuator and 7T multi-slice MRE sequence with motion encoding gradients capable of producing high resolution MRE elastograms of the human brain and lumbar spine were developed, and MRE was performed on both a validation phantom and multiple healthy human subjects. Through validation scans at both 3T and 7T at various resolutions, we determined that performing MRE at high resolution and high field strength does not inherently change the wavelength-based stiffness estimate of a linear isotropic material. Additionally, shear wavefield propagation was visualized at high resolution in preliminary human data, resulting in successfully generated elastograms of the human brain. Further investigation is needed to reduce noise and scanner artifacts in high resolution 7T scans, as well as to determine the relationship between noise, complex shear stiffness, and resolution. This pneumatic actuator will be used in all future human brain MRE investigations.

Chapter 4: Validation of High Resolution and Ultra-High Field Strength MRE on Shear Stiffness Reconstruction of the Human Brain Using Direct Inversion

4.1. Introduction

Performing MRE on brain tissue can provide information on different structures within brain tissue based on their mechanical properties, such as cell density, myelination, inflammation, and vascular density. These mechanical parameters can then be used to diagnose pathologies such as multiple sclerosis (MS), Alzheimer's disease, and Parkinson's disease, or indicate disease progression[10,22,23]. One of the current limitations, however, of performing MRE on brain tissue is the coarse resolution, leading to the lack of specificity in determining microstructural changes that result in these changes in viscoelastic parameters. While there are multiple methods of potentially tackling this issue, moving from conventional field strengths (1.5T or 3T) to the ultra-high field strength, 7T, is an attractive option as human 7T scanners have an increasing availability.

Compared to 3T scans, 7T has much greater sensitivity, and inherently increased signal to noise ratio (SNR) and spatial resolution[47]. While SNR theoretically scales with field strength, 7T MRE suffers from B_o and B_1 inhomogeneities that need to be addressed with shimming and reference volume collection. Additionally, at higher magnetic field strengths relaxation effects occur faster resulting in a decreased apparent T_2 (T_2*) value for tissue, and therefore requiring a smaller TE to better match the T_2* and reduce signal dropout. This presents a unique challenge in MRE, as the length of the echo time is longer than most other MRI sequences in order to accommodate the additional motion encoding gradient (MEG), leading to SNR and amplitude degradation in MRE more than other 7T sequences. Due to these challenges and the current novelty of 7T human MRI scanners, there have only been a handful of studies investigating 7T MRE. The first published study performing 7T MRE of the human brain was a single-subject feasibility study comparing MRE at 1.5T to MRE at the same resolution at 7T for partial brain coverage[68]. While this study proved the feasibility of MRE at 7T, it failed to show increased SNR or increased resolution at 7T. This was attributed to more pronounced susceptibility artifacts and greater T_2* spatial variation and signal decay. The following 7T MRE studies investigating the human brain were also partial-brain acquisition

only, and although high resolution was implemented, these studies still suffered from the same drawbacks (e.g., signal dropout, and distortions) as the first[29]. Additionally, the reported values of complex shear stiffness were much lower than that of other literature values. While motion corrections were successful at 7T on the magnitude images, distortion and inhomogeneity corrections were not, and neither was motion correction on phase images, despite their implementation at 3T[93]. Subsequent investigations have also found potential differences in mechanical properties between 1.5T, 3T, and 7T MRE, although these studies did not control for resolution or include phantom validation[34,35]. In these most recent studies comparing 1.5T, 3T, and 7T MRE of the human brain, MRE at 7T and 1mm resolution resulted in significantly lower stiffness values than MRE at 1.5T and 3T at 2 mm resolution[34,35]. However, one study indicated that when down sampled to 2 mm, the 7T MRE results matched the traditional MRE field strength results, but in a second study, the difference remained[34,35].

Despite these challenges, 7T MRE has shown promise in more recent pilot studies as a method of obtaining high resolution quantitative viscoelastic parameters of the human brain. At conventional field strengths, MRE has been shown to be sensitive to changes in brain viscoelasticity due to healthy brain development and aging, as well as changes due to neurodegenerative disease such as Multiple Sclerosis, Parkinson's Disease, progressive supranuclear palsy, dementia, and Alzheimer's disease[10,22,23]. By exploiting the high spatial resolution possible at 7T, we can potentially increase this sensitivity to show more subtle changes viscoelasticity and pinpoint changes in smaller brain sub-structures. However, as mentioned previously, aiming for higher resolution scans of the human brain at 7T, MRE presents unique challenges of decreased signal-to-noise ratio (SNR) and lower shear wave motion sensitivity. Additionally, it has been shown that quantitative values of MRE, i.e., the magnitude of the complex shear modulus estimate ($|G^*|$), are sensitive to changes in SNR[32], so 7T MRE can present a challenge of not only quality, but accuracy. While applying commonly-used filtering techniques (e.g., Gaussian, Median, Wavelet Thresholding, RER, directional filtering)[94–100] to MRE phase data can increase SNR (to combat low SNR

in high-resolution scans), this can also blur fine physiological features, decrease the effective resolution[33], resulting in artificially increased |G*|[32].

Another complication at 7T, particularly at high resolution, is image reconstruction error along phase wrapping lines when using scanner-reconstructed images. While advanced reconstruction options are available on some MRI scanners, they are not optimized for reconstructing phase images. Millimeter or sub-millimeter EPI using conventional reconstruction algorithms introduces irregularities and wrapping effects in the phase images that can bias the MRE inversion reconstruction. In order to be more advantageous than 3T MRE and provide accurate stiffness values for brain tissue at high resolution, the 7T MRE images collected must have sufficient amplitude of the motion encoded, be reconstructed from the Fourier space in an accurate manner to remove irregularities, and denoised without over-smoothening and losing anatomical structure.

In the past, we have shown that changes in resolution and field strength do not inherently change the value of |G*| in a linear elastic phantom (Chapter 3)[36,37]. However, MRE of phantoms typically have very high SNR, even at high resolutions, so this decrease in SNR as resolution increases may not have a large effect on scans with inherently high SNR. For MRE of the human brain however, SNR drastically drops with increasing resolution, very likely causing an artificially low |G*| calculation. While the preliminary results show an overall strong correlation between |G*| and OSS-SNR regardless of field strength and resolution, these initial analyses also indicate a more complex relationship when taking resolution into account that require a greater number of replicates. Due to this potential relationship described above, it is hypothesized that a different distribution of features is being captured at high resolution compared to those captured at low resolution.

In this Chapter, we have three main goals: (1) to demonstrate and validate the use and accuracy of 7T MRE at multiple high resolutions, using the advanced post-processing techniques of MP-PCA denoising and Gadgetron advanced image reconstruction, to accurately calculate the viscoelastic properties of the human brain and validation phantom using a direct inversion method, (2) to compare the results of matched-

resolution 3T and 7T MRE and determine the correlation between |G*| and OSS-SNR regardless of field strength, resolution and processing technique, and (3) to investigate the frequency dependence of the mechanical properties of the human brain in-vivo by performing multifrequency MRE of the healthy human brain at 7T.

4.2. Methods

4.2.1 7T MRE Sequence Parameter Optimization

Theoretically, SNR scales with field strength in MR imaging with the relationship $SNR \propto B_o$, and the resolution is approximately $1/n^{0.33}$ when B_o is increased by a factor of n[48]. The resolution can be even greater increased using different gradients and specialized sequences. However, despite the theoretical linear relationship between SNR and field strength, a linear increase is unattainable due to changing tissue relaxation and increased magnetic field inhomogeneities. B_o inhomogeneity directly scales with field strength, which leads to distortion in both the shape and intensity of images. This inhomogeneity reduces SNR, but can be combatted using decreased voxel volumes, shimming, and collecting reference volumes in opposite phase encoding directions so the distortions are in opposite directions and can be filtered out[51]. B_1 inhomogeneity also increases with field strength[47], as the B_1 operating wavelength gets closer to the diameter of the tissue of interest (in this case the human head) as B_o increases[49]. This results in decreased B_1 strength at the periphery of the tissue compared to the center, with peripheral B_1 being 42% lower than central B_1 [49]. This leads to changes in contrast and signal drop-out across the image, and conventional pulse sequences are particularly susceptible to this B_1 inhomogeneity.

As mentioned previously, in addition to increased B_o and B_1 inhomogeneities, at higher magnetic field strengths, relaxation effects occur faster, resulting in a decreased apparent T_2 (T_2*) value[49]. For example, for the gray matter in the brain, while T_2* at 3T is 66 ms, at 7T, T_2* is only 33.2 ms[50]. For example, the scaling of T_2* for subcortical gray matter can be approximated as $T_2^* = 1/(7+3.5 \times B_o)$[51]. This results in a unique problem not addressed at conventional field strengths, and that is making the TE of a sequence close enough to the T_2 or T_2* value to preserve SNR and signal amplitude. Long echo times make a sequence more sensitive to signal relaxation, resulting in lower SNR. In general, for MRI sequences, as described

through equations (23) and (24) in Section 2.5. Therefore, a larger TE compared to the relaxation constant results in both lower SNR and lower signal amplitude. However, in MRE, the length of the echo time is longer than most other MRI sequences in order to accommodate the MEG, leading to SNR and amplitude degradation in MRE more than other 7T sequences. An echo-planar imaging (EPI) pulse sequence is useful for such an application because it can acquire a necessary volume of data with short acquisition times.

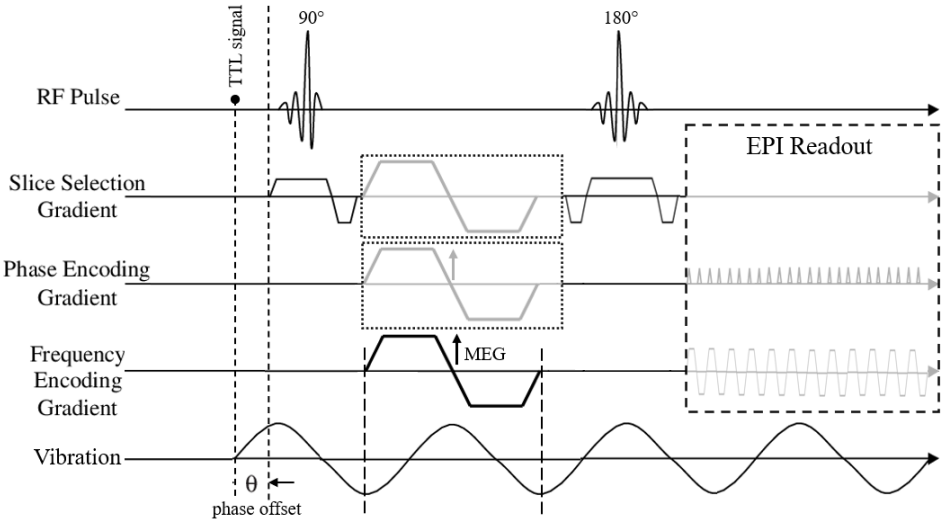

Figure 4.2.1.1. *Custom 7T MR Elastography sequence diagram with bipolar MEGs applied consecutively on frequency, phase and slice encoding directions.*

The modified single-shot multi-slice spin-echo 2D-EPI based sequence (pulse sequence diagram is shown below) was designed to acquire MRE data using phase shifted bipolar or trapezoidal flow-compensated motion-encoding gradients (MEGs) synchronized with the acoustic actuator by TTL triggering. Additionally, we used acceleration techniques such as GRAPPA and partial Fourier to decrease our TE over the course of sequence development from 100 ms to 65 ms to decrease signal dropout. We also investigated the difference between bipolar motion encoding gradients and flow-compensated motion encoding gradients. The switch to flow-compensated motion encoding gradients from bipolar resulted in more symmetric encoding of wave propagation and therefore complex shear stiffness estimates.

4.2.2 MP-PCA Denoising

We increase the SNR of our MRE acquisition without compromising the anatomical accuracy and spatial resolution by utilizing a Marchenko-Pastur Principal Component Analysis (MP-PCA) denoising algorithm (initially developed for diffusion MRI)[33]. In this technique, we are exploiting the intrinsic redundancies in MRE acquisition to identify and remove noise-only principal components[33]. Specifically, we can exploit the redundancies in slice acquisition (as in 48 acquisitions per slice) and the universal properties of the eigenspectrum of random covariance matrices, the non-gaussian noise-only principal components can be identified and removed. In general, a redundant data matrix can be synthesized by a combination of principal components/linearly independent sources. By doing singular value decomposition of our redundant data matrix, we can obtain our eigenvalues of this data matrix. In agreement with the random matrix theory for noisy covariance matrices, a number of the smallest nonzero eigenvalues, corresponding to the size of the matrix and the number of linearly independent sources, are described by the MP distribution. We can therefore identify and remove the pure noise eigenvalues by estimating noise level and number of significant signal components based on this MP distribution, resulting in our denoised matrix. Thereby, one increases precision and SNR without compromising physiological accuracy and spatial resolution[33].

4.2.3 Post-Processing, Inversion, and SNR Calculation

After image acquisition at 7T, both the raw data file and DICOM image series reconstructed with the Sum of Squares reconstruction for the MRE scans were collected. For the scanner reconstructed image series, we employed the MP-PCA denoising algorithm to both the magnitude and phase in a 5×5×5 sliding block[33]. The difference was then taken between two phase images acquired with opposite encoding directions, and the phase difference images were then curl filtered to remove the longitudinal wave component. We then performed a Fourier decomposition to extract the main harmonic, and we applied a quartic smoothing kerned with the kerned window scaled based on resolution, previously validated with phantom studies[36]. Finally, we calculated loss and storage modulus (elastograms) using the Algebraic Inversion of the Helmholtz equation (Equation 3). Using the raw data files, we used Gadgetron to generate

magnitude and phase images before performing the same pre-processing and inversion method as previously described.

We also calculated OSS-SNR for each image series and method of processing. To do this, we used the displacement as calculated during Algebraic Inversion processing (SEGUE unwrapped phase[101] multiplied by the MENC value) before using Fourier decomposition to extract the different harmonic displacements. We then calculated Octahedral Shear Strain (OSS) of only the main harmonic component and the OSS of the sum of the other harmonic components. The ratio of the main harmonic component OSS to the OSS of the other harmonics is used as the OSS-SNR of the scan and data processing method. Whole brain, white matter, and gray matter binary masks were generated using SPM12 with the magnitude images captured during MRE acquisition. These masks were used to segment elastograms and OSS-SNR masks to calculate whole brain, gray matter, and white matter averages.

4.2.4 Phantom Validation Scans

We used the phantom MRE experiments performed at 3T and 7T as described in Section 3.3.1 to validate the developed MRE sequence and post-processing pipeline at the resolutions of interest with high SNR and OSS-SNR. As a summary: MRE was first performed at 3T with 2.5mm isotropic resolution on a custom silicone elasticity MRE phantom (CIRS 049) with a background Young's modulus of 5.0±1.0 kPa and spherical inclusions of 3.0±1.0 kPa, 8.0±1.0 kPa, 12.0±2.0 kPa, and 20.0±2.0 kPa Young's Modulus (Fig 4.3.1.1(a), background |G*| of 1.7±0.3 kPa and spherical inclusions of 1.0±0.3 kPa, 2.7±0.3 kPa, 4.0±0.7 kPa, and 6.7±0.7 kPa Shear Modulus). This MRE data was acquired for 48 slices with 3D motion encoding gradients using an echo planar spin echo 2D pulse sequence[102] with vibration frequency 50Hz in a 3T Siemens Skyra scanner with a 16-channel head coil (Siemens Healthineers).

MRE acquisition was performed on a on 7T whole-body MRI scanner (Magnetom 7T, Siemens Healthineers, Germany) equipped with a 70 mT/m gradient coil and a 32-channel head coil (Nova Medical, Wakefield, MA) using our custom multi-slice 2D-EPI pulse sequence with 3D MEGs[30], a vibration frequency of 50 Hz and 8 phase offsets at 2.5 mm, 1.7 mm, and 1.1 mm isotropic imaging resolutions. I

would like to note that when referring to 'resolution' in this work, we are referring to imaging resolution and not resolution of elastographic detail, of which the numerical value is difficult to exactly determine and is dependent on inversion technique[103]. In both cases, external vibration was applied to the surface of the phantom using a custom pneumatic actuator described in Chapter 3 and Triolo, *et al*.[31,36,37,104]. Elastograms and OSS-SNR maps of the phantom's cross section were obtained using the processing methods described previously on the scanner-reconstructed images. The average of each elastogram and OSS-SNR map of five homogeneous slices per scan (2.5 mm at 3T and 2.5 mm, 1.7 mm, and 1.1 mm at 7T) using the AIDE algorithm with and without denoising were compared using a one-way ANOVA with a post-hoc Tukey test to compare between groups. An ROI around the 1.0 kPa and 2.7 kPa |G*| spherical inclusions were also drawn to compare accuracy of small structures at each resolution.

After human MRE experiments described in the following sections completed, we performed additional phantom scans with adjusted parameters to obtain similar SNR, vibration amplitude, and OSS-SNR to that of the human scans for further comparison and validation of accuracy. MRE was performed on the same validation phantom at 7T using our custom sequence and pneumatic MRE actuator[31,36,37,104], a vibration frequency of 50 Hz and 8 phases at 1.1 mm, 1.7 mm, and 2.5 mm isotropic resolution. To obtain a comparable SNR to that of human scans, a lower excitation flip angle of 35^{o} was used. To obtain a similar vibration amplitude and OSS-SNR, lower amplitudes of vibration were used by adjusting the input voltage to one of two relatively low levels. Raw data was collected for this phantom validation, and the mean of each elastogram and OSS-SNR map of five homogeneous slices per scan were analyzed with the same four image processing methods as the human scans (*e.g.*, standard reconstruction, standard reconstruction with denoising, advanced reconstruction, and advanced reconstruction with denoising) and groups were compared.

4.2.5. Human Scans

Full brain coverage MRE at 2.5 mm, 1.7 mm, and 1.1 mm isotropic resolution was performed on twenty healthy volunteers (Average age 27 ± 3 years old, 10F, 10M), and partial brain coverage MRE (32 slices)

at 0.8mm isotropic resolution was performed on five of those healthy volunteers (Average age 30 ± 3 years old, 3F, 2M) at 7T using previously described MRE pulse sequence (Section 4.2.1), a vibration frequency of 50 Hz and 8 phase offsets with the sequence parameters listed in Table 4.2.5.1.

Table 4.2.5.1. *Sequence Parameters for Full (2.5 mm, 1.7 mm, 1.1 mm Resolutions) and Partial (0.8 mm Resolution) Brain Coverage Human MRE Scans at 7T*

Resolution	**2.5 mm**	**1.7 mm**	**1.1 mm**	**0.8 mm**
TE (ms)	65	65	65	70
TR (ms)	4800	7200	14000	5120
GRAPPA	2	2	3	3
Partial Fourier	N/A	N/A	7/8	7/8
Bandwidth (Hz/pixel)	2013	2042	1849	1221
# of Slices	40	60	100	32
Scan Duration (mm:ss)	04:05	06:07	12:22	04:31

Vibration was applied to the head via the custom pneumatic actuator, using the final 3D printed TPU end-effector shaped to rest in the base of the head coil as described in Triolo, *et al*.[31] (Figure 4.2.5.1). Elastograms and OSS-SNR maps of each of the scans were obtained using the processing methods described above on the scanner-reconstructed images, and raw data image processing was performed on all scans.

As a full description of the post-processing: both the raw data file and DICOM image series (reconstructed with the scanner-based 'Sum of Squares' coil combination) for the MRE scans were collected. For the scanner reconstructed image series (subsequently called 'standard reconstruction'), we employed the MP-PCA denoising algorithm to complex signal in a 5×5×5 sliding block. The difference was then taken between two phase images acquired with reversed MEGs, and the phase difference images were then curl filtered to remove the longitudinal wave component. We then performed a Fourier decomposition to extract the main harmonic, and applied a quartic smoothing kernel with the kernel window scaled based on imaging resolution, previously validated with phantom studies (described in Chapters 3 and 4). Finally, we calculated loss and storage modulus (elastograms) using the Algebraic Inversion of the Helmholtz equation[90]. Using the raw data files, we perform post-hoc offline reconstruction of magnitude and phase images (subsequently called 'advanced reconstruction') using an open-source Gadgetron image

reconstruction framework[105] to remove artifacts caused by scanner reconstruction error such as inaccurate pixel assignment along phase wrapping lines. Gadgetron implements advanced reconstruction techniques that are not typically used in scanners due to long computation time. Specifically in this study, we are using advanced coil combination based on a non-linear optimization before performing the same pre-processing (including denoising) and inversion method as previously described.

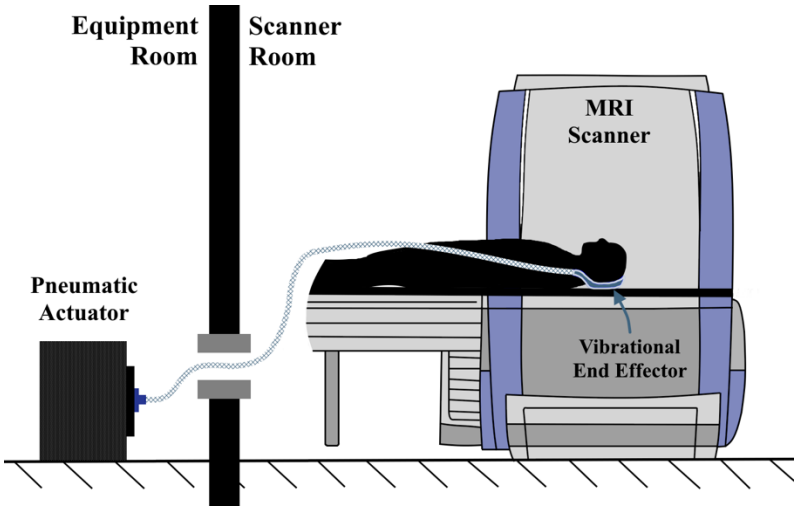

Figure 4.2.5.1: Schematic of MRE actuator and volunteer positioning *inside the MRI scanner. Air pressure waves are generated by the active components outside the magnet room and pushed through semi-flexible tubing into a 3D printed TPU end effector placed under the volunteer's head.*

We also calculated OSS-SNR for each image series and method of processing (*e.g.*, standard reconstruction, standard reconstruction with denoising, advanced reconstruction, and advanced reconstruction with denoising). To do this, we used the displacement as calculated during Algebraic Inversion processing (SEGUE[101] unwrapped phase multiplied by the MENC value) before using Fourier decomposition to extract the different harmonic displacements. We then calculated OSS[91] of only the main harmonic component and the OSS of the sum of the other harmonic components. The ratio of the main harmonic component OSS to the OSS of the other harmonics is used as the OSS-SNR of the scan and data processing method. Whole brain, white matter, and gray matter binary masks were generated using SPM12[106] using an MP2RAGE T1-weighted whole-brain acquisition (0.7 mm isotropic resolution, TE/TR = 3.62/6000 ms) for each subject, and the resulting masks and T1 structural images were then co-registered

with the magnitude images captured during MRE acquisition. The masks were used to segment elastograms and OSS-SNR maps to calculate whole brain, gray matter, and white matter averages.

Only data processed with advanced reconstruction and denoising will be presented for 0.8mm resolution scans due to the partial brain coverage and limited dataset. For the whole brain coverage scans, repeated measures ANOVA with Bonferroni correction and multiple comparisons was performed between each group of resolutions and post-processing to determine statistical significance while better accounting for inter-subject variation.

4.2.5.1 Human Scans at 3T

Full brain coverage MRE was performed on the same subjects on a 3T Siemens Skyra scanner with a 16-channel head coil (Siemens Healthineers) at 2.5 mm isotropic resolution using an echo planar spin echo 2D pulse sequence with vibration frequency 50 Hz, TE = 70 ms, TR = 5600 ms, GRAPPA = 3. It is worth noting that while the sum-of-squares coil combination option was chosen for the 7T MRE scans, due to improvements in reconstruction software, the advanced coil combine option was used in all 3T MRE scans. Elastograms and OSS-SNR maps of the 3T scans were obtained using the processing methods described above on the scanner-reconstructed images (both with and without denoising). Repeated measures ANOVA was performed between each group of field strengths, resolutions, and post-processing to determine statistical significance while better accounting for inter-subject variation.

4.3. Results

4.3.1. Phantom Validation Scans

Although we see a 2.8%, 2.7%, and 32.6% increases in OSS-SNR in the 2.5 mm, 1.7 mm, and 1.1 mm phantom scans respectively, there is very little to no change in |G*| values comparing denoised data to non-denoised data, likely due to the already very high initial OSS-SNR values (Table 4.3.1.1).

Table 4.3.1.1. *Phantom Validation of Post Processing using Average |G*| Over 5 Homogeneous Slices and Percent Increase in OSS-SNR post- Denoising*

Isotropic Resolution (Field Strength)	**2.5 mm (3T)**	**2.5 mm (7T)**	**1.7 mm (7T)**	**1.3 mm (7T)**	**1.1 mm (7T)**
|G*| Standard (kPa)	1.430±0.023	1.425±0.006	1.427±0.004	1.430±0.004	1.423±0.010
|G*| Denoised (kPa)	1.430±0.023	1.425±0.006	1.429±0.007	1.430±0.010	1.423±0.010
OSS-SNR Percent Increase	9.6%	2.8%	2.7%	26.4%	32.6%

The estimated shear modulus values were within the specification range given by the phantom's data sheet (1.7±0.3 kPa). There was also no significant difference found between any of the pairs of |G*| data sets ($p>0.50$), now including the denoised data in the analysis. This would indicate that in a homogeneous, linearly elastic material, changing resolution or adding our post-processing techniques do not inherently change the calculated |G*| of the material being imaged with sufficiently high OSS-SNR. Additionally, moving from 2.5 mm resolution to 1.1 mm resolution results in shear modulus estimates of the spherical inclusions that match the manufacturer specifications of the custom MRE phantom.

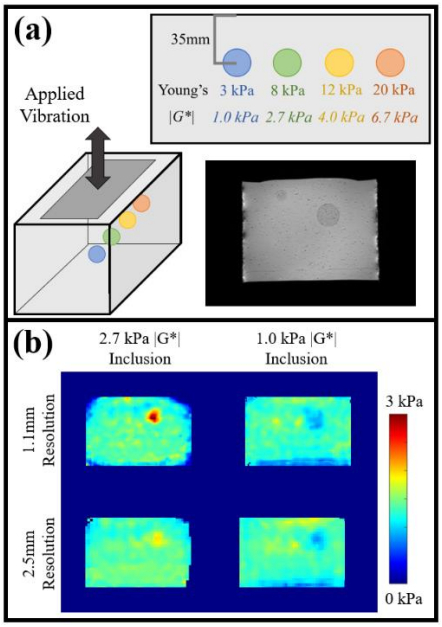

Figure 4.3.1.1. *(a) Schematic and T2-weighted slice of custom CIRS phantom with a background |G*| of 1.7 kPa and multiple spherical inclusions (listed as both Young's Modulus values and |G*|), (b) 1.1 mm and 2.5 mm resolution elastograms in the custom phantom in slices with the 2.7 kPa |G*| (measured as 2.393 kPa |G*| in 1.1 mm resolution scan and 1.744 kPa in 2.5mm resolution scan) and 1.0 kPa |G*| (measured as 1.003 kPa |G*| in 1.1 mm resolution scan and 1.078 kPa in 2.5mm resolution scan) spherical inclusions*

At 2.5 mm resolution, the inclusion in the specification range 1.0±0.3 kPa Shear modulus is within the specified range at 1.078 kPa, but the inclusion of specification range 2.7±0.3 kPa is not in the correct range at only 1.744 kPa. However, at 1.1mm resolution, both inclusions are calculated to have |G*| in the correct ranges at 1.003 kPa and 2.393 kPa respectively (Fig 4.3.1.1(b)). This implies that increasing resolution results in more accurate shear modulus calculations for smaller features, such as these inclusions. This also, however, is dependent on shear wavelength (and therefore vibration frequency) utilized, as well as the inversion method.

In phantom validation scans with lowered SNR and OSS-SNR values similar to the human scans, there was still no difference found in apparent complex shear modulus between the different resolution groups (Figure 4.3.1.2). Additionally, there is a slight trending increase in average magnitude of the complex shear modulus with improvement in OSS-SNR due to the application of denoising and advanced reconstruction.

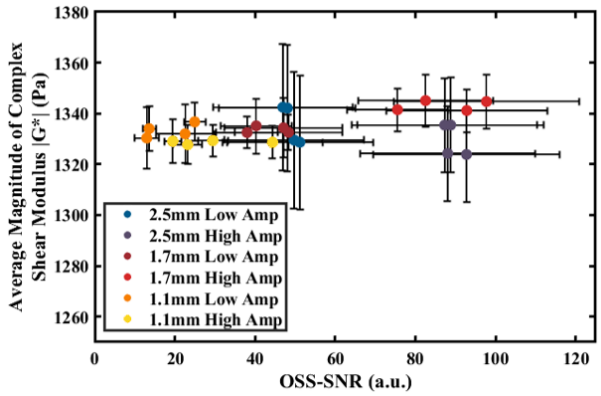

Figure 4.3.1.2. *Relationship between average |G*| and OSS-SNR in homogeneous slices in our linearly viscoelastic phantom with OSS-SNRs lowered to be similar to those found in human brain imaging.*

4.3.2. 7T Human Scans

By applying MP-PCA denoising on the standard scanner reconstruction images, the OSS-SNR significantly increased by 27.1%, 64.4%, and 127.1% with an increase of 1.4%, 2.8%, and 7.5% in |G*| in the 2.5 mm, 1.7 mm, and 1.1 mm imaging resolution datasets, respectively. We generally observe a greater increase in |G*| with a greater increase in OSS-SNR when moving from standard scanner reconstruction to advanced

Gadgetron reconstruction (Table 4.3.2.1). Less of an increase in both OSS-SNR and |G*| is observed in lower resolution scans, as expected, due to inherently higher initial OSS-SNR in those datasets. Therefore, we assume that the noise-only components are being removed to increase OSS-SNR, and the increase in OSS-SNR results in a higher apparent |G*| as more of the true signal is implemented in the viscoelastic inversion step.

Table 4.3.2.1. *Percent Increases in OSS-SNR for Denoising, Advanced Reconstruction, and Advanced Reconstruction with Denoising as compared to Standard Reconstruction*

Isotropic Resolution	**2.5mm**	**1.7mm**	**1.1mm**
OSS-SNR / |G*| Standard Reconstruction	25.2 / 2.05 kPa	12.9 / 1.67 kPa	3.6 / 1.33 kPa
Percent Increase with Denoising	27.1% / 1.4%	64.4% / 2.8%	127.1% / 7.5%
Percent Increase with Advanced Reconstruction	60.8% / 3.0%	84.1% / 4.9%	166.5% / 14.7%
Percent Increase with Advanced Recon and Denoising	98.3% / 4.0%	174.0% / 7.2%	374.5% / 18.7%

Simply moving from standard scanner reconstruction to advanced reconstruction (without denoising) significantly increases OSS-SNR by 60.8%, 84.1%, and 166.5% ($p<0.05$) and increases |G*| by 3.0%, 4.9%, and 14.7% in the 2.5 mm, 1.7 mm, and 1.1 mm datasets, respectively. We can visually observe that advanced reconstruction using the Gadgetron framework not only improves phase image quality in general, but also removes artifacts along wrapping lines, which causes large regions of drop-out in the elastograms generated using the 7T scanner sum-of-squares reconstruction (Fig 4.3.1).

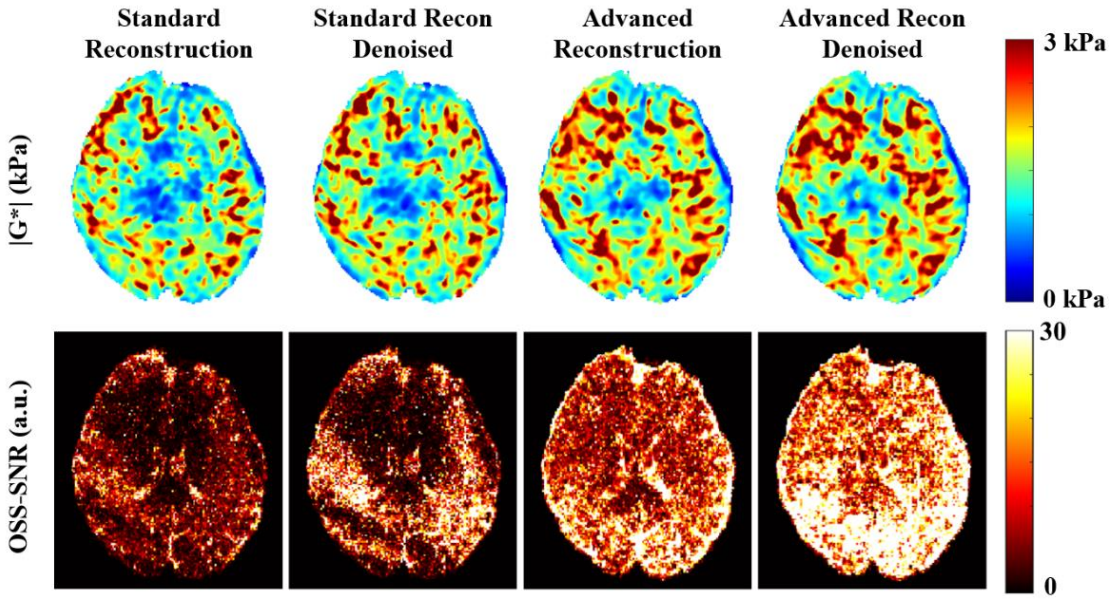

Figure 4.3.2.1: *High resolution (1.1 mm isotropic resolution) Elastogram and OSS-SNR progression with increasingly advanced reconstruction algorithm in the same subject. Denoising removes thermal and gaussian noise while advanced reconstruction removes phase wrapping error lines.*

Additionally, we observe the same trend of decreased whole-brain OSS-SNR and average |G*| with increased resolution as was shown in our preliminary results[36,104] and previous partial-brain coverage studies[29,34,35,68,93] (Table 4.3.2.2, Figs 4.3.2.2 and 4.3.2.3). Additional application of denoising on the advanced reconstruction data results in a 4.0%, 7.2%, and 18.7% increase in |G*| and 98.3%, 174.0%, and 374.5% statistically significant increase in OSS-SNR in the 2.5 mm, 1.7 mm, and 1.1 mm datasets, respectively, when compared to standard reconstruction without denoising ($p<0.05$). All whole brain, white matter, and gray matter average values at each resolution after advanced reconstruction with denoising can be found in Table 4.3.2.2, with the final OSS-SNR achieved at each resolution as 50.6±30.8, 35.3±21.8, 17.1±9.8, and 20.1±7.5 at 2.5 mm, 1.7 mm, 1.1 mm, and 0.8 mm resolutions respectively. Consistent with the prior literature, average |G*|, storage modulus, and loss modulus is greater in white matter than gray matter at all resolutions (Table 4.3.2.2), with the average values at 1.1 mm isotropic resolution as 1.73±0.16 kPa for white matter and 1.55±0.13 kPa for gray matter.

Table 4.3.2.2. *Whole Brain, White Matter, and Gray Matter Averages for Each Resolution with Advanced Reconstruction and Denoising Applied Concurrently (Average ± Standard Deviation, *only five subjects represented)*

Whole Brain				
Resolution	2.5 mm	1.7 mm	1.1 mm	0.8 mm*
|G*| (kPa)	2.13±0.12	1.79±0.12	1.58±0.13	1.40±0.17
Storage (kPa)	1.70±0.11	1.42±0.11	1.21±0.11	1.09±0.14
Loss (kPa)	0.74±0.08	0.68±0.07	0.64±0.07	0.56±0.10
OSS-SNR	50.6±30.8	35.3±21.8	17.1±9.8	20.1±7.5
White Matter				
|G*| (kPa)	2.25±0.12	1.95±0.13	1.73±0.16	
Storage (kPa)	1.84±0.12	1.54±0.12	1.30±0.13	
Loss (kPa)	0.85±0.09	0.78±0.09	0.74±0.10	
OSS-SNR	53.3±35.2	34.6±22.5	15.8±9.2	
Gray Matter				
|G*| (kPa)	2.12±0.12	1.76±0.12	1.55±0.13	
Storage (kPa)	1.70±0.11	1.40±0.10	1.19±0.10	
Loss (kPa)	0.73±0.07	0.67±0.06	0.63±0.07	
OSS-SNR	49.6±29.6	36.7±28.0	16.9±10.2	

Within resolution groups, using advanced reconstruction significantly increased |G*| relative to standard reconstruction (Fig 4.3.2.3(b), $p<0.05$), and the application of denoising significantly increased |G*| when applied to both reconstruction methods ($p<0.05$). The single exception to these trends is that there is no significant difference when comparing standard reconstruction with denoising to advanced reconstruction without denoising in the 2.5mm resolution group. Comparing between resolution groups for whole-brain average |G*|, each of the resolution groups was significantly different from each other (*i.e.*, all 2.5 mm resolution groups are different from all 1.7 mm resolution groups and all 1.1 mm resolution groups).

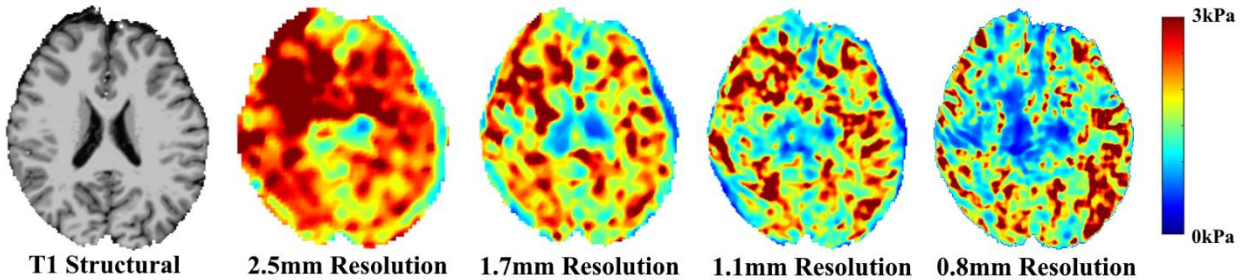

Figure 4.3.2.2. *The same |G*| slice shown at each resolution in a single subject*

Using advanced reconstruction with denoising on the 1.1 mm resolution dataset increased its average OSS-SNR to be in the same range as the 1.7 mm resolution standard reconstruction datasets both with and without denoising. A similar effect is seen in other resolution groups, so generally, applying advanced reconstruction methods to high resolution images can increase the average OSS-SNR values to be in the same range as lower resolution images (Fig 4.3.2.3 (a)). All other groups are statistically different from each other ($p<0.05$). This effect is contrary to that of whole-brain average $|G^*|$ where there are no overlaps between resolution groups, indicating a more complex relationship than simply a difference in OSS-SNR. While denoising affects $|G^*|$ as a whole, of its component parts, the imaginary component is usually more susceptible to noise, and it is therefore valuable to investigate loss and storage modulus individually.

Using advanced reconstruction with denoising on the 1.1 mm resolution dataset increased its average loss modulus to be in the same range as the 1.7 mm resolution standard reconstruction datasets both with and without denoising. A similar effect is seen in other resolution groups, so generally, applying advanced reconstruction methods to high resolution images can increase the average Loss Modulus values to be in the same range as lower resolution images (Fig 4.3.2.3(c)). All other groups are statistically different from each other ($p<0.05$).

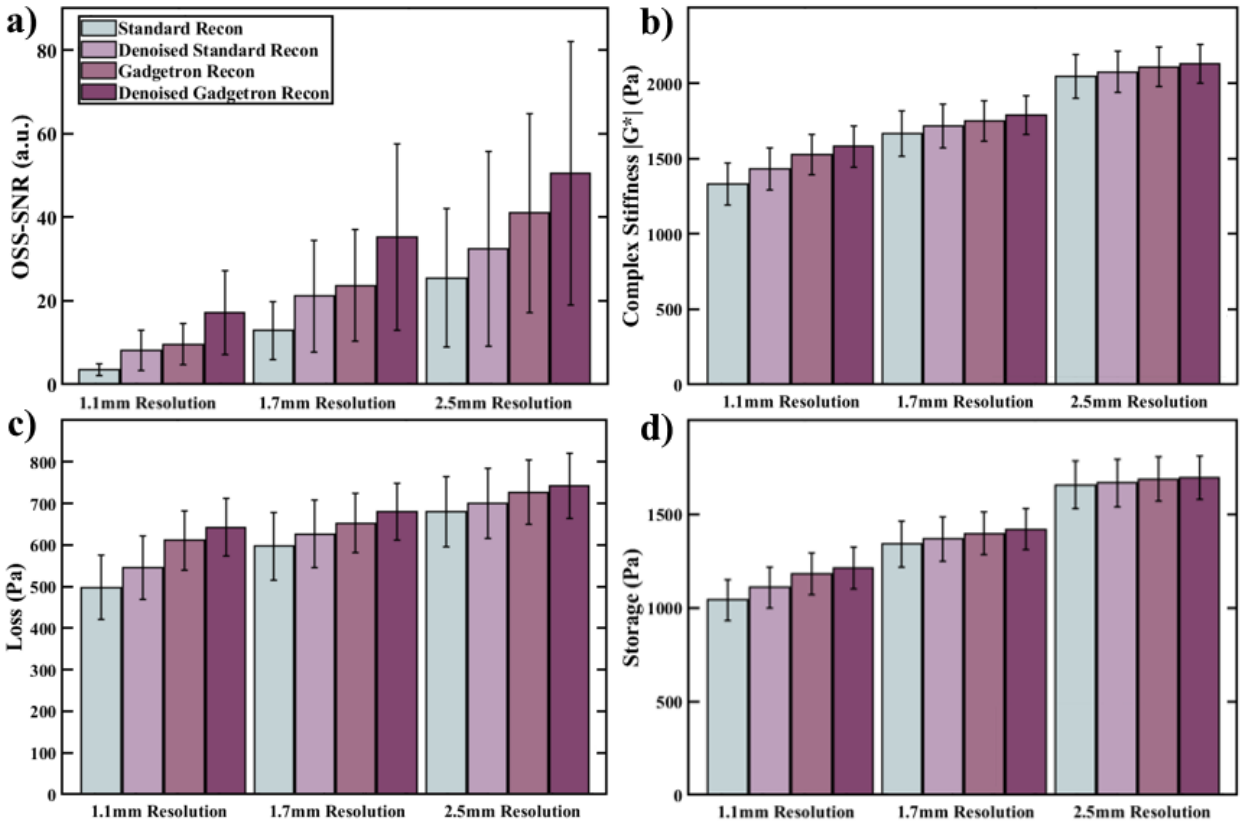

Figure 4.3.2.3. *Whole brain average a) OSS-SNR (arbitrary units) and b) magnitude of the complex shear modulus (|G*|) in Pa over twenty healthy human subjects for each whole brain resolution, and post-processing procedure where error bars indicate standard deviation. Whole brain average c) Loss Modulus (G") and d) Storage Modulus (G') and in Pa over twenty healthy human subjects for each whole brain resolution and post-processing procedure where error bars indicate standard deviation.*

As was the case with |G*|, both storage modulus and loss modulus significantly increase due to the application of denoising in both standard reconstruction and advanced reconstruction for all groups (Fig 4.3.2.3(c,d), $p<0.05$). The single exception to these trends is that there is no significant difference in storage modulus when comparing standard reconstruction with denoising to advanced reconstruction without denoising in the 2.5 mm resolution group, as was the case with whole brain average |G*|. Comparing between resolution groups for whole-brain average storage modulus, each of the resolution groups were significantly different from each other (*i.e.*, all 2.5 mm resolution groups are different from all 1.7 mm resolution groups and all 1.1 mm resolution groups), although this was not the case with loss modulus. While the trends in storage modulus appear to mimic the trends in |G*|, the trends in loss modulus mimic the trends in OSS-SNR.

4.4. Matched-Resolution 7T vs 3T Results and Discussion

Within field strength and resolution groups, there is no statistically significant difference between the non-denoised and denoised whole brain |G*| of 2.5mm at 3T ($p>0.05$), but in all other groups (2.5mm, 1.7mm, and 1.1mm at 7T), denoising significantly increased |G*| from standard reconstruction without denoising ($p<0.05$) and from advanced reconstruction without denoising ($p<0.05$). However, in all 7T datasets, there was no significant increase in |G*| between the standard reconstruction with denoising and advanced reconstruction without denoising (Fig. 4.4.1). Comparing between field strength/resolution groups, there are no significant differences between matched-resolution groups despite the difference in field strength, but each of the resolution groups were significantly different from each other (*i.e.*, all 2.5mm resolution groups are different from all 1.7mm resolution groups and all 1.1mm resolution groups).

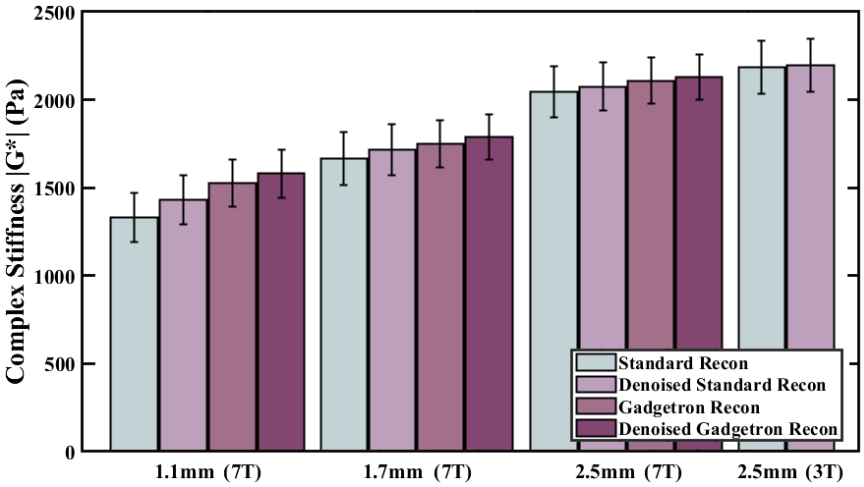

Figure 4.4.1. *Whole brain average magnitude of the complex shear modulus (|G*|) in Pa over twenty healthy human subjects for each field strength, resolution, and post-processing procedure*

Overall, we found no significant differences between whole brain average OSS-SNR, |G*|, G', or G" when comparing between matched resolution (2.5mm isotropic resolution) scans across field strengths. This combined with the phantom validation results strongly implies that the same features are being captured with both of these scans and that there are no inherent changes in viscoelastic properties of the brain under 7T when compared to those under 3T.

4.5. 7T MRE Discussion and Conclusions

4.5.1. Achieving High OSS-SNR MRE at 7T

In this work, MRE was successfully implemented at multiple resolutions at 7T using a custom pneumatic actuator and motion sensitive single-shot EPI-based sequence. Additionally, we applied advanced signal processing techniques to reduce the effects of thermal and Gaussian noise, as well as mitigate image reconstruction errors, to produce accurate elastograms with high OSS-SNR at high resolution. In using our custom elasticity phantom, we validated the accuracy of our sequence and proposed post-processing procedures. We have confirmed that in a linearly elastic material with no known complex microstructure and high OSS-SNR, there are no inherent differences when upgrading to high resolutions at 7T. We also were able to confirm that the noise-only components are removed when using the MP-PCA denoising algorithm, as OSS-SNR was only marginally increased in these cases with inherently high image SNR, and these increases did not change the resulting |G*| values. Using these high OSS-SNR phantom scans, we also investigated the benefits of using higher resolution to resolve small structures, *e.g.*, the spherical inclusions. While we achieved a measurement of |G*| within the manufacturing specifications of the softer inclusion at both 2.5 mm and 1.1 mm resolutions, we only achieved a |G*| within the manufacturing specifications for the stiffer inclusion at 1.1mm isotropic resolution. We hypothesize that this is due to the larger difference between the background modulus (1.7 kPa |G*|) and the modulus of the stiffer inclusion (2.7 kPa |G*|) compared to the softer inclusion (1.0 kPa |G*|). The higher resolution acquisition can better resolve the changes in wavelength and wave speed between materials of different mechanical properties, therefore achieving a more accurate measurement even when tissue types that are beside each other are different. In phantom validation scans with SNR and OSS-SNR similar to that of human scans, there is a slight trending increase in average |G*| with improvement in OSS-SNR due to the application of denoising and advanced reconstruction, although this increase is not statistically significant between any group. There is, additionally, still no significant difference in apparent |G*| between resolution groups despite the lower OSS-SNR, as these values were still above the recommended threshold for accuracy of 3.0 as determined by McGarry, *et al.*[91].

In performing MRE on the human brain, however, there were much greater variations in OSS-SNR captured than in the phantom scans, particularly at the higher resolutions. Particularly at 1.1 mm isotropic resolution, the artifacts resulting from reconstruction error occurred more frequently, which was not the case in the phantom scans, leading to a lower OSS-SNR in these scans prior to reconstruction using the Gadgetron framework. This greater variation can also be attributed to a lowered vibration amplitude due to insufficient contact with the vibrational end-effector, which appeared to be the largest contributor to lowered SNR post-reconstruction using the Gadgetron framework. Although moving to 7T MRE and/or higher resolutions can theoretically decrease vibrational motion sensitivity, we found similar intra-subject vibrational amplitudes across all scan types, with the largest variability being inter-subject. When comparing between signal processing techniques within resolution groups, overall, applying denoising significantly increases OSS-SNR (and therefore apparent |G*|), as does using advanced reconstruction using Gadgetron framework. Using both denoising and advanced reconstruction results in the highest SNR and apparent |G*| for all resolution groups. Taking into consideration the scan duration for each resolution, phantom validation results, and average OSS-SNR after the advanced reconstruction techniques, we have established 1.1 mm isotropic resolution as the most suitable and robust for MRE at 7T to accurately calculate the viscoelastic properties of the whole human brain.

Advanced processing techniques such as rigid body motion correction, B_0 correction, and distortion corrections are not incorporated into the proposed framework but may be considered in the future. Rigid body motion correction is partly addressed in the current framework by removing the 0 Hz component of motion during the Fourier decomposition step, although a prior investigation utilized an SPM-based realign routine, resulting in sharper looking images[93]. In MRE with EPI readout, typically, B_0 and geometric distortion correction are interrelated, as B_0 inhomogeneities result in said geometric distortions[93]. This technique, however, requires either an additional B_0 field map at the time of data collection or repeated full acquisition with reversed phase encoding directions, and while this correction appears quite significant in simulations, its effect is less so *in vivo*[107]. While Gadgetron has a functionality to perform B_0 correction

without such a field map, this algorithm has not been applied. Generally, the potential corrections were not implemented at this time, as to not introduce additional controlled bias, as they have not been shown to be accurate in correction of average stiffness values, particularly with direction inversion techniques[107].

Additionally, one potential drawback of using a denoising technique is the possibility of an artificially increased OSS-SNR due to the general removal of higher order components[108,109]. This effect has been observed when using filtering such as Gaussian or Median filtering[94,96,98–100,109–111], which also result in the blurring of fine physiological features. However, the MP-PCA method aims to remove only the noise without interfering with the signal itself (*i.e.*, without blurring features)[112]. The denoising algorithm is additionally applied in local patches (in our case, a 5×5×5 sliding window) without assumptions on noise levels. Therefore, under the assumption smoothly varying noise maps (noise being constant within a local patch), the denoising can be used on data with spatially varying noise levels[108] and estimate such noise maps accordingly[113]. Just like smoothing, the MP-PCA will not correct the signal offset due to non-Gaussian MR signals, as the algorithm removes random signal fluctuations without interfering with the signal[112,113]. Therefore, the average signal is not altered. If the data are non-Gaussian distributed (*e.g.*, Rician), then the noise will be removed, but the Rician noise floor will be preserved.

4.5.2. Resolution-Dependent Apparent Differences in |G|*

As stated previously, we see a much greater change in Loss Modulus (the imaginary component of complex shear modulus) with the application of these processing techniques than with Storage Modulus (the real component of complex shear modulus), as the imaginary component is more sensitive to noise. So, while advanced reconstruction and denoising that increases G" values from higher resolution scans to be statistically in the same range as lower resolution groups, this is not the case for G' or, consequently, |G*|. We observed that using these advanced processing techniques also increases OSS-SNR in the higher resolution groups to be in the same range as the lower resolution groups. While the trends from Fig 4.5.2.1 show an overall strong correlation between |G*| and OSS-SNR regardless of resolution and processing

technique, these initial statistical analyses and the results from the various phantom scans indicate a more complex relationship when taking resolution into account.

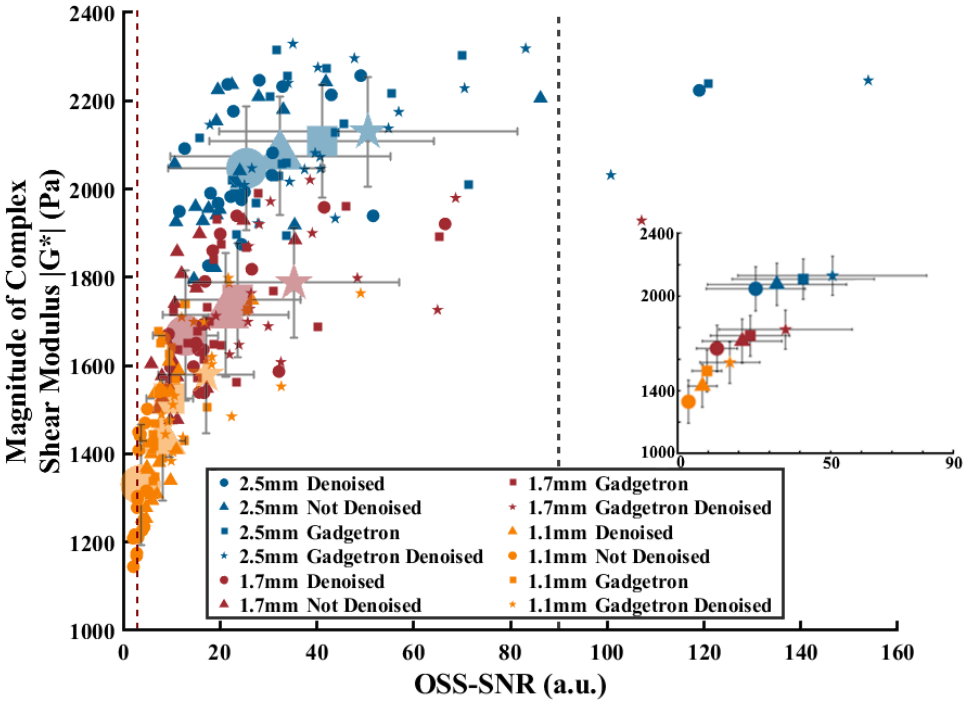

Figure 4.5.2.1. *The relationship between OSS-SNR and whole brain average |G*| across all resolutions and post-processing methods for all twenty subjects where the overlayed, larger icons with error bars represent the average and standard deviations for each resolution and post-processing group, the red dashed line indicates the 3.0 OSS-SNR cutoff for accuracy, and the gray dashed line indicates the area displayed in the smaller plot that only shows the averaged values*

This trend of decreased |G*| and G' values with increasing resolution can also be identified when analyzing whole-brain average mechanical properties between studies that employ direct inversion methods and subject populations but use different resolutions[7,16,18,20,23,24,29,34,35,39,43,87,114–118]. This relationship between resolution and |G*| was also specifically identified by Barnhill, *et al.*[34] and Marshall, *et al.*[35] in the same subject populations, who hypothesized that a different distribution of features is being captured at high-resolution[34]. It was further hypothesized that higher resolution scans, which capture fine features and interfaces not visible at low resolution, produce lower elasticity estimates due to these finer features creating more tortuosity in the wave[34,111]. Neither of these studies, however, investigated the effect of SNR or post-

processing techniques, nor did they investigate matched resolution scans between field strengths, so the lack of controlled variables made it difficult to support this hypothesis further. Additionally, the theory that higher imaging resolutions capture finer viscoelastic features than lower resolutions can be investigated further in future studies by utilizing heterogeneous phantoms with known mechanical properties and by analyzing differences in smaller brain regions, which is one of the goals of using such high-resolution scans. These results also imply the need for establishing different baseline complex shear modulus values for different resolutions and different OSS-SNR ranges for MRE of the human brain. Regardless of the differences between resolutions, it may be recommended that studies involving MRE of the human brain only compare between groups captured at the same resolution. It is possible, however, based on our linearly elastic phantom validation results that these differences may be an artifact of a direct inversion method, which may be addressed by employing an iterative inversion method, such as nonlinear inversion, to the same subject data[119]. Additionally, it may be advisable that in studies involving comparisons of patient populations, OSS-SNR be assessed, and the groups being compared have OSS-SNRs above the accuracy threshold. In conclusion, we have demonstrated the accuracy and robustness of high-resolution 7T MRE with advanced post-processing pipeline. The developed techniques will be used in future studies to investigate biomechanical parameters of small volume brain sub-structures with applications in neurodegenerative diseases and other relevant neurological disorders.

4.6. Preliminary Multi-frequency 7T MRE

4.6.1. Introduction

Most biological tissues, including the human brain, exhibit a frequency-dependent mechanical response which has yet to be explored at 7T[7]. In this study, we investigate the frequency dependence of the mechanical properties of the human brain *in-vivo*. The purpose of this section is to perform Multifrequency MRE of the healthy human brain at the ultra-high field strength, 7T.

4.6.2. Methods

Full brain coverage MRE was then performed at 1.1 mm isotropic resolution at 40, 50, and 60 Hz on a 10-person subset of the healthy human subjects scanned in Chapter 5.1 using the 7T MRE setup

described in Chapters 3 and previous Sections in this Chapter. As described as the "Advanced Reconstruction" process in Previous Sections in this Chapter, phase images were reconstructed from raw data post-hoc using Gadgetron[105] open-source image reconstruction, magnitude images were initially masked using SPM12[106], denoised using a MP-PCA algorithm[112,113], and unwrapped using a Segue Phase Unwrapping[101]. Curl filtering, Fourier decomposition, and a quartic smoothing kernel (scaled for resolution based on our previous investigation)[37,104] were used to acquire wavefield images, before Algebraic Inversion of the Helmholtz Equation was used to calculate the magnitude of the complex shear modulus (|G*|). Octahedral Shear Strain Signal-to-Noise ratio (OSS-SNR)[91] was also calculated for each scan to ensure high enough quality for accurate viscoelastic inversion. Whole brain, white matter, and grey matter average |G*| for each subject at each frequency were calculated (Fig. 4.6.3.1).

Table 4.6.2.1. *Sequence Parameters for 7T Scanning Sessions 1 and 2 and the 3T Scanning Sessions*

Scan Type	Resolution (isotropic)	TE (ms)	TR (ms)	GRAPPA	Partial Fourier	Bandwidth	# of Slices
40Hz MRE	1.1 mm	65	14000	3	7/8	1849	100
50Hz MRE	1.1 mm	65	14000	3	7/8	1849	100
60Hz MRE	1.1 mm	65	14000	3	7/8	1849	100

Of the initial 10 individuals scanned at each frequency, one subject was excluded did not complete the scanning protocol due to a scanner hardware error. The other three were excluded due to low vibration amplitude in the 60 Hz scan, resulting in an OSS-SNR value too low to be considered accurate for viscoelastic reconstruction (OSS-SNR < 3.0)[91].

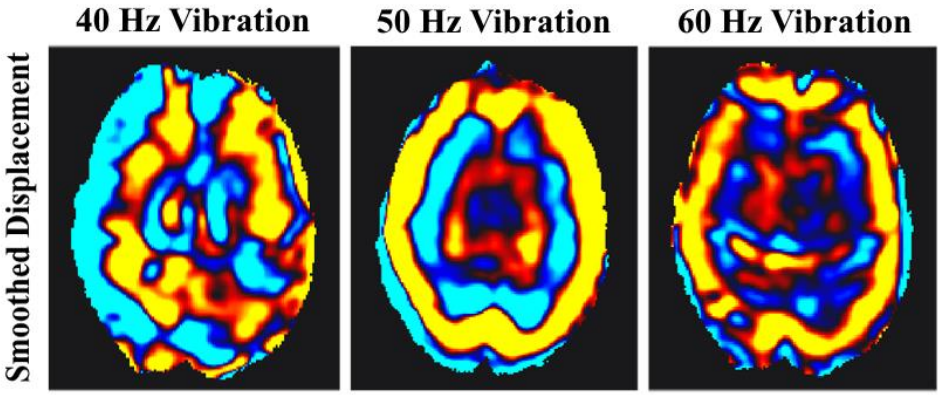

Figure 4.6.2.1. *Smoothed Displacement for the Central Slice of One Healthy Human Subject at 40, 50, and 60 Hz Vibration Frequency*

4.6.3. Results

Using our custom 7T MRE sequence, pneumatic actuator, and advanced post-processing procedure, we successfully performed multifrequency MRE on 6 human subjects at 7T. Wavefield images and elastograms of a representative central slice for each frequency are shown in Figs 4.6.2.1 and 4.6.3.1. We found an increase in stiffness measurement with vibration frequency as consistent with previous literature at conventional field strengths (Figs. 4.6.3.1 and 4.6.3.2). Additionally, we determined that average |G*| white matter values are generally higher than that of grey matter, also consistent with literature (Fig. 4.6.3.2).

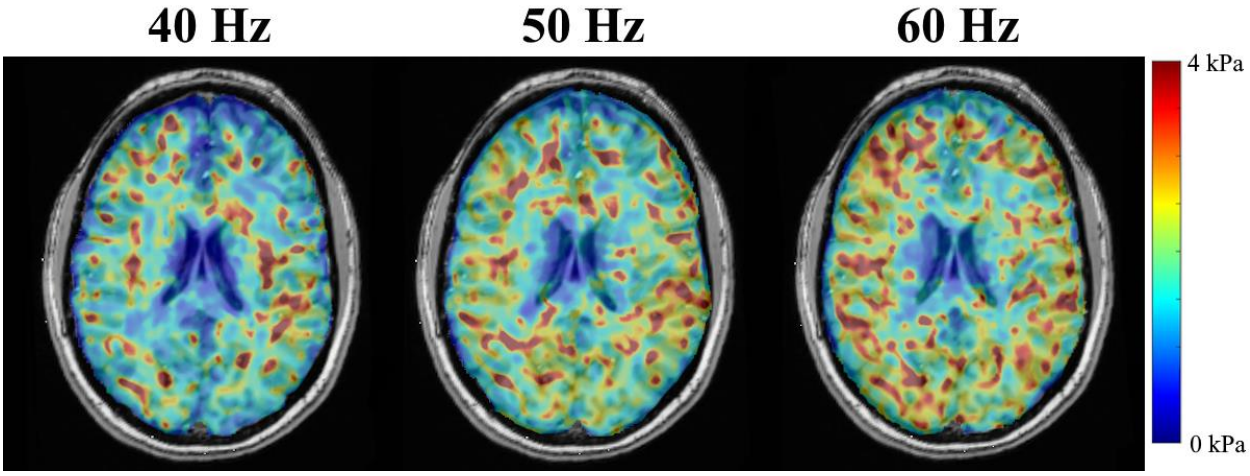

Figure 4.6.3.1. *|G*| map overlayed with the associated T1 structural image for the Central Slice of One Healthy Human Subject at 40, 50, and 60 Hz Vibration Frequency*

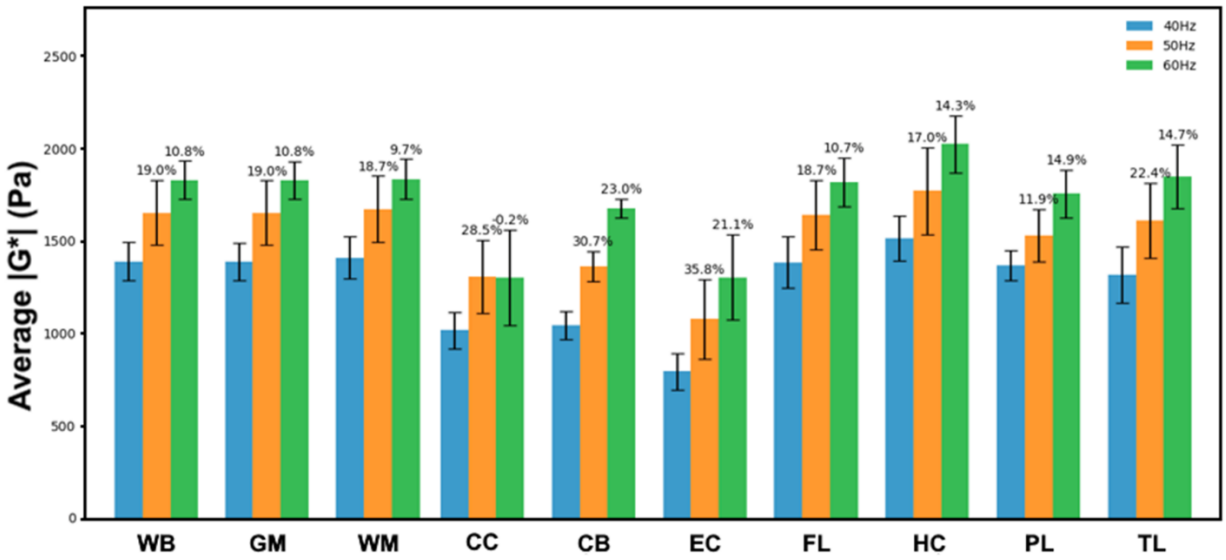

Figure 4.6.3.2. *Average |G*| at each frequency in the whole brain (WB), gray matter (GM), white matter, (WM), corpus callosum (CC), cerebellum (CB), entorhinal cortex (EC), frontal lobe (FL), hippocampus (HC), parietal lobe (PL), and temporal lobe (TL)*

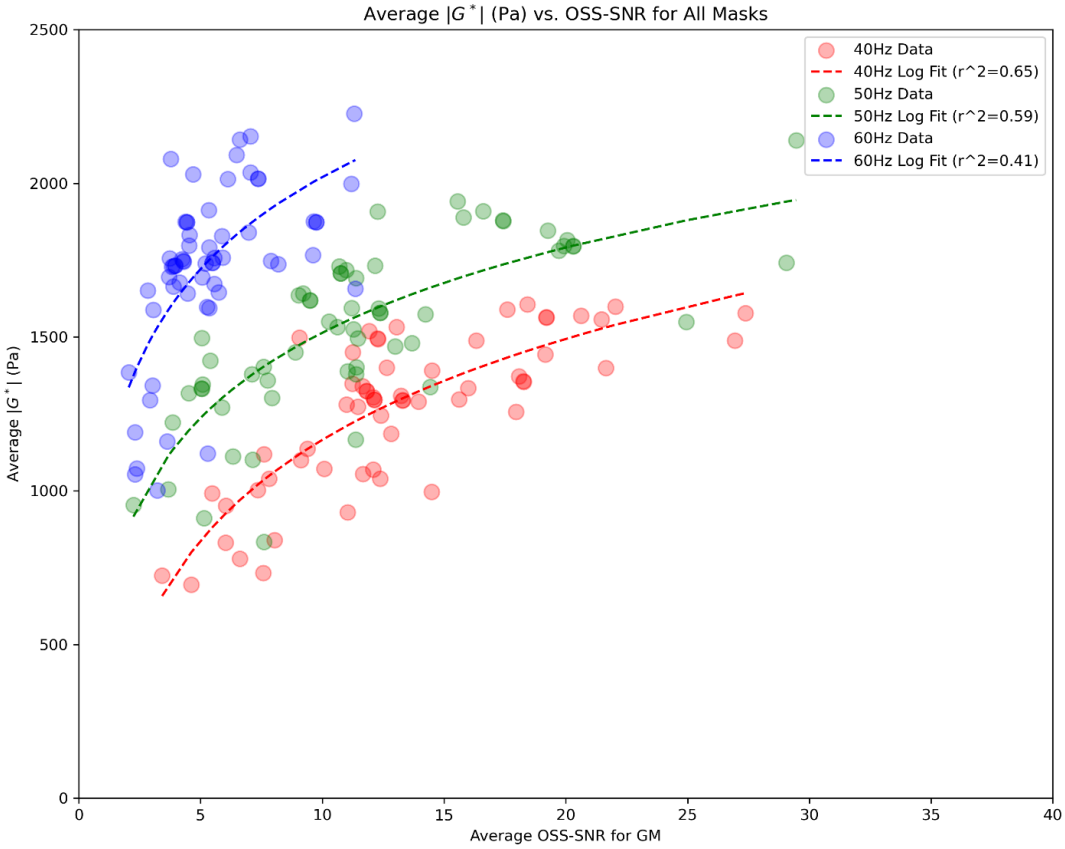

Figure 4.6.3.3. *The relationship between regional average |G*| and regional average OSS-SNR at each frequency (log fit)*

Additionally, as we saw with the single frequency investigation in the previous sections, we find a relationship between |G*| and OSS-SNR, which may cause difficulties in comparing |G*| directly between frequencies, as higher frequency acquisitions typically have lower OSS-SNR (Figure 4.6.3.3). We therefore performed a logarithmic fit for each frequency group, displaying how the higher the frequency of vibration applied, the higher the |G*| appears, despite lower OSS-SNR.

4.6.4. Discussion

As previously stated, 3 subjects were excluded due to low vibration amplitude in the 60 Hz scan, resulting in an OSS-SNR value too low to be considered accurate for viscoelastic reconstruction (OSS-SNR < 3.0). This is due to hardware limitations of the MRE actuator, as vibration amplitude drop-off becomes more significant at higher frequencies. Multiple improvements to the MRE actuator to improve this, such as a thicker plate covering the subwoofer cone and smaller diameter, less compliant tubing, can be made and have been successfully implemented in other MRE setups. Additionally, geometric distortion becomes more apparent at higher frequencies, which should be addressed in future investigations.

In the future, this multifrequency MRE protocol can be used to determine region specific frequency-dependent mechanical properties as it has in the past at 3T, but at the ultra-high resolution possible at 7T. Additionally, with the suggested modifications to the custom MRE actuator, the frequency range of our multifrequency protocol can be extended to the 80-100 Hz range to gather more frequency-specific mechanical properties of the human brain. By obtaining the multifrequency response of the human brain at the ultra-high resolution possible using 7T MRE, we can develop subfield specific material models. These material models can therefore be used to inform FE brain models and therefore simulate brain motion at the high frequency impacts accurately. Understanding brain movement and tissue deformation mechanisms during these impacts is a powerful strategy for predicting brain injury and developing preventative equipment.

Chapter 5: Characterizing Brain Mechanics Through 7T MRE with 3T MRE Comparison via Nonlinear Inversion

5.1. Introduction

In the previous Chapter, we have demonstrated the accuracy and robustness of high-resolution 7T MRE with advanced post-processing pipeline using direct inversion. We investigated the relationship between resolution, OSS-SNR, and the application of different advanced post-processing techniques. We observed that using these advanced processing techniques also increases OSS-SNR in the higher resolution groups to be in the same range as the lower resolution groups. However, while our results showed an overall strong correlation between |G*| and OSS-SNR regardless of resolution and processing technique, these initial statistical analyses and the results from the various phantom scans indicate a more complex relationship when taking resolution into account. This relationship between resolution and |G*| was also specifically identified by Barnhill, *et al.*[34] and Marshall, *et al.*[35] in the same subject populations, who hypothesized that a different distribution of features is being captured at high-resolution[34]. It was further hypothesized that higher resolution scans, which capture fine features and interfaces not visible at low resolution, produce lower elasticity estimates due to these finer features creating more tortuosity in the wave[34,111]. However, the limitation of the investigation in the previous Chapter, as well as of the referenced prior studies, is that |G*| was calculated using direct inversion methods.

As described in Chapter 2, direct inversion methods require a variety of simplifying mechanical assumptions that, while result in fast processing, may contribute to the observed resolution-dependent |G*| results for brain tissue. Because these |G*| values are calculated directly using displacement maps, it is very likely that higher spatial wave sampling rate is a contributor to this resolution-dependent differences. Additionally, using direct inversion requires the application of many spatial and temporal smoothening filter (*e.g.*, curl filtering and Romano filtering), reducing both the effective property map resolution (and therefore the benefit of moving to high resolutions), and the benefit of using non-smoothening denoising methods like the MP-PCA denoised applied in the previous Chapter. Therefore, it became clear that moving to a finite element, optimization based, nonlinear inversional algorithm was necessary for better

understanding of the mechanical properties of highly inhomogeneous and complex tissues such as the brain, as well as for determining clinical applicability of high resolution MRE.

Nonlinear viscoelastic inversion, as developed by McGarry, *et al.*[119], has been extensively used and validated for MRE of the human brain at various resolutions at 3T (3.00 mm – 1.25 mm) for OSS-SNR values above 3.0. As described in Chapter 2, nonlinear inversion uses an iterative optimization-based method, using the displacement measurements from MRE acquisition as boundary conditions in sliding subzones to calculate heterogeneous mechanical properties of tissue, reducing model-data mismatch that occurs in direct inversion methods[120]. While it is more computationally intensive and computation time scales exponentially with increased resolution, nonlinear inversion better accounts for reflection and mode conversion effects that are present for tissue and allows us to better model the small heterogeneous structures in the brain that are also visible in other imaging modalities[120].

With regards to other imaging modalities, this Chapter will also discuss a benefit of moving to 7T MRE- the availability of other high-resolution imaging. As stated earlier in this introduction, 1.25 mm resolution MRE has recently been achieved through utilizing k-space undersampling techniques, which may result in some doubt about why 7T MRE is necessary. While 7T MRE boasts higher image SNR and OSS-SNR at these higher resolutions and do not require such extreme undersampling methods to maintain a low TE, one of the main benefits of performing high resolution MRE at 7T is that other high resolution imaging modalities that are only available at 7T can also be captured for the same subjects in the same imaging sessions. The highest resolution that was performed in previous Chapters on the entire healthy young-adult cohort, 1.1 mm isotropic resolution, was specifically targeted because it is the resolution that is used during 7T Diffusion Tensor Imaging (DTI).

White matter microstructure has been known to change due to inflammation, demyelination, and neurological diseases and disorders. The most common imaging technique for investigating white matter microstructure integrity is DTI, which measures restricted diffusion of water in tissue[1]. Leveraging ultra-high field 7T MRI, with increased signal-to-noise ratio and improved soft tissue contrast, allows us to

accurately map tissue microstructure. 7T DTI has been used to investigate many clinical applications such as Epilepsy, Alzheimer's disease, and depression. By performing MRE at a matched resolution to these highly resolved 7T MRI sequences, we can determine the relationship between stiffness and these other properties like microstructural integrity, water diffusion, tissue anisotropy, perfusion, etc., as these contribute to the heterogeneity and anisotropic material properties of brain tissue. This relationship has been previously shown at 3T[121], where stiffness and damping ratio were correlated with diffusion metrics in small white matter structures. However, this was performed at a more course resolution and therefore partial volume effects may be playing a role in some of these correlations.

In the main portion of this Chapter, we will establish high resolution of whole brain coverage MRE at 7T with a target of 1 mm isotropic resolution, in addition to demonstrating the advanced post-processing techniques of Marchenko-Pastur Principal Component Analysis (MP-PCA) denoising[112], Gadgetron image reconstruction framework[105], and Nonlinear Viscoelastic Inversion[119] to accurately calculate the viscoelastic properties of the human brain while considering the tradeoff between resolution, OSS-SNR, and scan time. In addition to performing our own validation of the accuracy of nonlinear inversion through elasticity phantom experiments and single-subject repeatability, we will also compare our 7T results to results from the same cohort as collected at 3T using a sequence with which nonlinear inversion has been previously validated. In the secondary portion of this Chapter, we will utilize the high-resolution Diffusion Weighted Imaging (DWI) that is able to be captured at 7T to determine the relationship between the microstructural information captured though DWI (mean diffusivity, radial diffusivity, and fractional anisotropy) and the mechanical metrics measured by 7T MRE (shear stiffness and damping ratio).

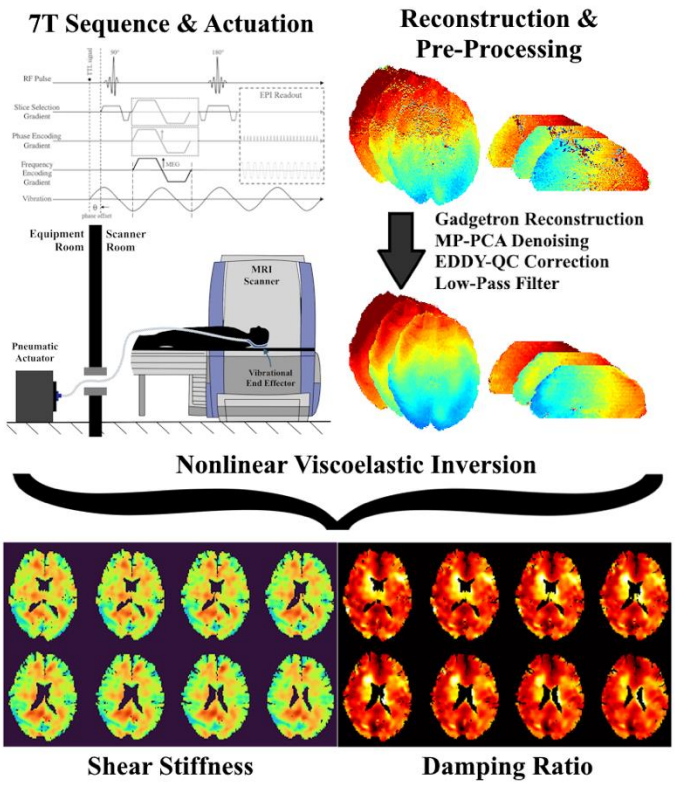

Figure 5.1.1. *Methodological Overview of 7T MRE*

5.2. 7T MRE Methods

5.2.1. Data Acquisition, Post-Processing, Inversion, and SNR Calculation

The ultra-high field data were acquired on 7T whole-body MRI scanner (Magnetom 7T, Siemens Healthineers, Germany) equipped with a 70 mT/m gradient coil and a 32-channel head coil (Nova Medical, Wakefield, MA). After each scanning session, both the raw data and DICOM image series for the MRE scans were collected. Using the raw data, we perform post-hoc offline reconstruction of magnitude and phase images using an open-source Gadgetron image reconstruction framework[105] to remove artifacts caused by scanner reconstruction error, such as inaccurate value assignment in pixels along phase wrapping lines. Gadgetron implements advanced reconstruction techniques that are not typically used in scanners due to long computation time. Specifically in this study, we are using advanced coil combination based on a non-linear optimization scheme[122,123]. To remove spatially varying noise in our MRE acquisition without comprising the anatomical accuracy and spatial resolution, we utilize an MP-PCA denoising algorithm as

described in the previous Chapter[112]. We employed the MP-PCA denoising algorithm to complex signal in a 5×5×5 sliding block.

The difference was then taken between two phase images acquired with reversed MEGs and unwrapped using SEGUE unwrapping[101]. Using the denoised Gadgetron reconstructed magnitude images for each image series, we used FSL's EDDY framework[124] to perform motion correction on these magnitude images, as well as use EDDY QC to generate a subject motion report for each acquisition for each subject. While EDDY does not have the capability to perform motion corrections on phase data, we were able to use the subject motion report to correct changes in phase that results from significant subject motions (above 2 standard deviations of average subject motion). While interleaved acquisition is useful in EPI sequences for reducing distortion, subject motion may cause a 'z-striping' effect where reference phase is only altered due to small subject motion in every other slice. After removing large outliers based on the EDDY QC motion report, we employed a simple low-pass Butterworth filter to remove the high-frequency striping effect that occurs due to small, irregular subject motions. In extreme striping cases, we also used the motion report to estimate the approximate phase in these slices as if the subject had not moved. Finally, Nonlinear Viscoelastic Inversion was used to calculate the commonly reported metrics, shear stiffness (μ, equation 1) and damping ratio (ξ, equation 2) from the denoised and motion-corrected unwrapped displacement data, where G' is the storage modulus, G" is the loss modulus, and G*=G'+iG"[119].

$$\mu = {2|G^*|^2}\Big/{(G' + |G^*|)} \tag{26}$$

$$\xi = \frac{G''}{2G'} \tag{27}$$

We also calculated OSS-SNR for each image series. To do this, we used the displacement as calculated during pre- processing (SEGUE unwrapped phase difference multiplied by the MENC value) before using Fourier decomposition to extract the different harmonic displacements. We then calculated OSS[91] of only the main harmonic component and the OSS of the sum of the other harmonic components. The ratio of the main harmonic component OSS to the OSS of the other harmonics is used as the OSS-SNR

of the scan and data processing method. Whole brain, white matter, and gray matter binary masks were generated using SPM12[106] using an MP2RAGE T1-weighted whole-brain acquisition (0.7 mm isotropic resolution, TE/TR = 3.62/6000 ms) for each subject, and the resulting masks and T1 structural images were then co-registered with the motion-corrected magnitude images captured during MRE acquisition. The masks were used to segment elastograms and OSS-SNR maps to calculate whole brain, gray matter, and white matter averages.

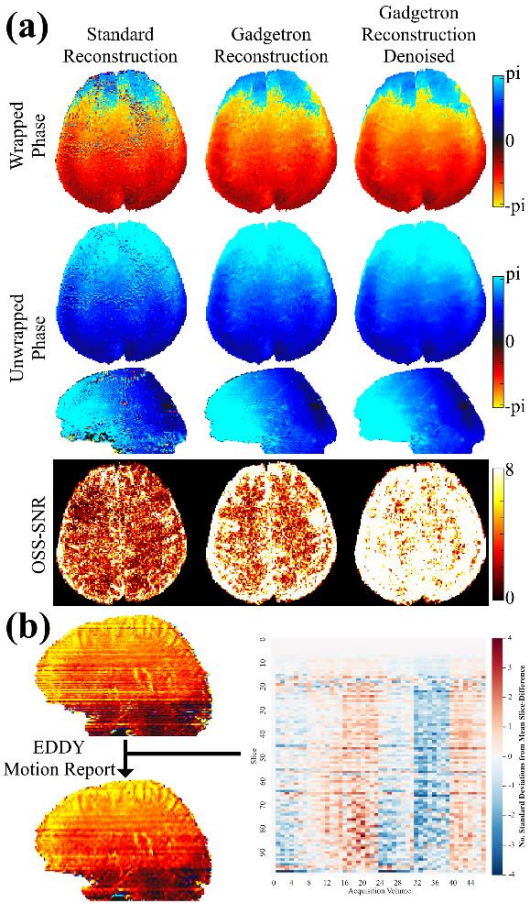

Figure 5.2.1.1. Post-processing pipeline and the effects/benefits of each post-processing step. *(a) using the Gadgetron reconstruction algorithm instead of the standard scanner reconstruction algorithm removes phase irregularities that occur due to low image SNR along phase wrapping lines during acquisition, using MP-PCA denoising removes spatially varying noise, overall increasing OSS-SNR, and (b) applying EDDY correction realigns the raw magnitude and phase images, as well as produces a motion report that can be used in conjunction with low-pass filtering to correct slice-wise irregularities in phase that occur due to irregular subject motion.*

5.2.2. Phantom Validation Scans

To validate the developed MRE sequence at the resolutions of interest with high SNR and OSS-SNR, we performed experiments on a custom elasticity MRE phantom (CIRS 049, CIRS, USA) with the manufacturer's specifications of a background Young's modulus of 5.0±1.0 kPa and spherical inclusions of 3.00±1.00 kPa, 8.00±1.00 kPa, 12.00±2.00 kPa, and 20.00±2.00 kPa Young's Modulus (Fig 5.3.1.1(a), background shear stiffness of 1.70±0.30 kPa and spherical inclusions of 1.00±0.30 kPa, 2.70±0.30 kPa, 4.00±0.70 kPa, and 6.70±0.70 kPa Shear Modulus). MRE acquisition was performed at 7T using our custom multi-slice 2D-EPI pulse sequence with 3D MEGs[30], a vibration frequency of 50Hz and 8 phase offsets at 2.5 mm, 1.7 mm, and 1.1 mm isotropic imaging resolutions. The authors would like to note that when referring to 'resolution' in this work, we are referring to imaging resolution and not resolution of elastographic detail, of which the numerical value is difficult to exactly determine and is dependent on inversion technique[103].

To obtain a similar vibration amplitude and OSS-SNR, low amplitudes of vibration were used by adjusting the input voltage to one of two relatively low levels. To obtain a comparable image SNR to that of human scans, a lower excitation flip angle of 35^{o} was used. External vibration was applied to the surface of the phantom using a custom pneumatic actuator described in Triolo, *et al*.[31,36,37,104] and Chapter 2 of this work. Elastograms and OSS-SNR maps of the phantom's cross section were obtained using the post-processing methods described previously. The average of each elastogram and OSS-SNR map of five homogeneous slices per scan (2.5 mm, 1.7 mm, and 1.1 mm) were compared. An ROI around the 1.00 kPa and 2.70 kPa shear stiffness spherical inclusions were also drawn to compare accuracy of small structures at each resolution.

5.2.3. Human Scans

Full brain coverage MRE at 2.5 mm, 1.7 mm, and 1.1 mm isotropic resolution was performed on eighteen healthy volunteers (Average age 27.5 ± 3.6 years old, 9F, 9M) at 7T using previously described MRE pulse sequence, a vibration frequency of 50 Hz and 8 phase offsets with the sequence parameters listed in Table 5.2.3.1. One of these subjects was scanned at each of the three full-brain coverage resolutions

three times over the course of one week in order to test repeatability (twice in one day and once on a different day). Informed consent was obtained from all participants for being included in the study. Full brain coverage MRE was also performed on sixteen of the same subjects on a 3T Siemens Skyra scanner with a 16-channel head coil (Siemens Healthineers) at 2.5mm isotropic resolution using an echo planar spin echo 2D pulse sequence with vibration frequency 50 Hz, TE = 70 ms, TR = 5600 ms, GRAPPA = 3.

Table 5.2.3.1: *Sequence Parameters for Whole Brain Coverage Human MRE Scans at 7T*

Resolution	**TE**	**TR**	**GRAPPA**	**Partial Fourier**	**# of Slices**	**Scan Duration** (mm:ss)
2.5mm	65ms	4800ms	2	N/A	40	04:05
1.7mm	65ms	7200ms	2	N/A	60	06:07
1.1mm	65ms	14000ms	3	7/8	100	12:22

Vibration was applied to the head via the custom pneumatic actuator, using the final 3D printed TPU end-effector shaped to rest in the base of the head coil as described in Triolo, *et al*.[31] Elastograms and OSS-SNR maps of each of the scans were obtained using the processing methods described above, but scanner reconstructed images were processed from the 3T data instead of the raw data files. Repeated measures ANOVA with Bonferroni correction and multiple comparisons was performed between each group of resolutions and field strengths to determine statistical significance while accounting for inter-subject variation. To investigate the similarity between the 3T and 7T datasets at matched resolution, we also calculated the average Structural Similarity Index (SSIM), as defined by:

$$\mathrm{SSIM}(x,y) = \frac{(2\mu_x\mu_y+c_1)(2\sigma_{xy}+c_2)}{(\mu_x^2+\mu_y^2+c_1)(\sigma_x^2+\sigma_y^2+c_2)} \qquad (28)$$

Where μ_x is the voxel-by-voxel mean of x (*i.e.*, MRE 3T elastograms), μ_y is the voxel-by-voxel mean of y (*i.e.*, MRE 7T elastograms), σ_x^2 is the spatial variance of x, σ_y^2 is the spatial variance of y, σ_{xy} is the spatial covariance of x and y, and the c's are stabilization variables. MATLAB was used to perform this analysis, so the structural similarity for each pixel is based on its relationship to other pixels in an 11-by-11 window. This metric has been historically used to compare between reconstruction and undersampling methods in MRE studies[125,126]. However, the different acquisition resolutions have not been compared with SSIM

analysis. In order to reduce any bias by up-sampling and interpolating low resolution data or down-sampling high resolution data, we only used SSIM to compare between the images of matched resolution.

Using the MP2RAGE T1-weighted images acquired for each subject, Freesurfer 7.0 segmentation was performed, and masks for each region of interest (whole brain left hemisphere, whole brain right hemisphere, caudate, corpus callosum, hippocampus, putamen, and thalamus) were generated based on each individual's parcellation. The T1 structural image and resulting masks were co-registered and resliced to the MRE magnitude space for each resolution and field strength using SPM12. Regional average stiffness and damping ratio, percent difference in stiffness and damping ratio between gray matter and white matter, percent difference in stiffness and damping ratio between left hemisphere and right hemisphere, and stiffness contrasts (between small regions and gray matter, small regions and white matter, and between the caudate and putamen) were calculated for each individual. Paired t-tests were used to compare between left and right hemispheres and Cohen's-d was calculated to determine effect size (reported in Supplementary Materials). Prior to all ANOVA and t-tests performed, a Shapiro Wilk test was performed to ensure that the data are normally distributed, and correction has been applied if necessary for the t-tests. Most between-group analyses were performed with ANOVAs, however, which is considered a robust test against the normality assumption.

5.3. 7T MRE Results

5.3.1. Phantom Validation Scans

In phantom validation scans with lowered SNR and OSS-SNR values, similar to the human scans, the estimated shear modulus values were within the specification range given by the phantom's data sheet (1.70±0.30 kPa). There was also no significant difference in shear modulus found between any of the resolution groups ($p>0.50$). This would indicate that in a homogeneous, linearly elastic material, changing resolution does not inherently change the calculated shear stiffness of the material being imaged. Furthermore, moving from 2.5 mm resolution to 1.1 mm resolution results in shear modulus estimates of the spherical inclusions that match the manufacturer specifications of the custom MRE phantom.

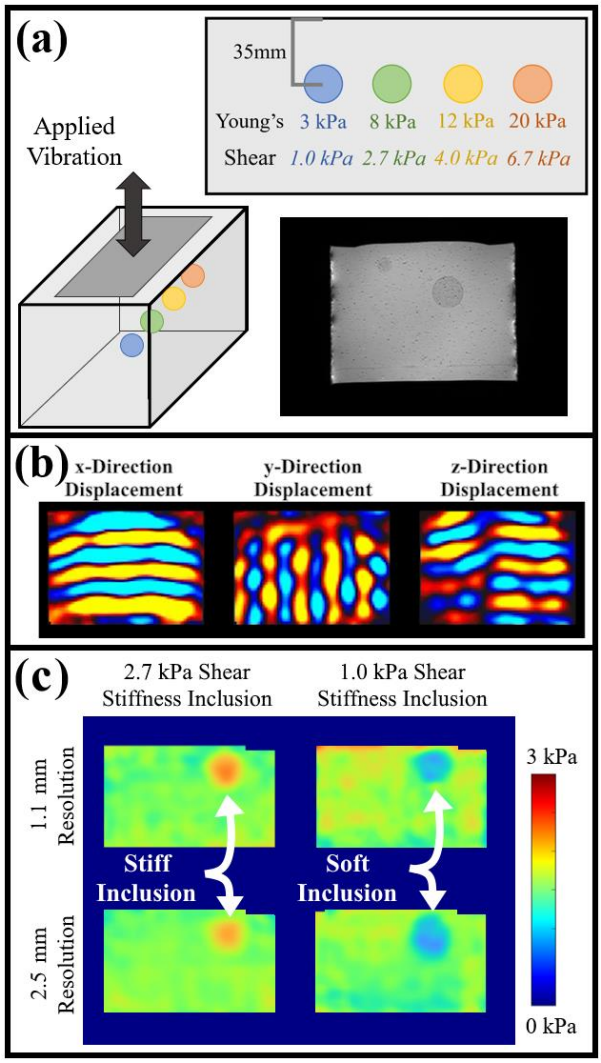

Figure 5.3.1.1. (a) *Schematic and T2-weighted slice of custom CIRS phantom with a background shear of 1.7 kPa and multiple spherical inclusions (listed as both Young's Modulus values and shear modulus), (b) normalized displacement in a homogeneous slice of the custom phantom shown at 1.1 mm resolution in all three orthogonal directions, and* ***(c)*** *1.1 mm and 2.5 mm resolution elastograms in the custom phantom in slices with the 2.70±0.30 kPa shear modulus (measured as 2.12±0.07 kPa shear stiffness in 1.1 mm resolution scan and 1.74±0.243 kPa in 2.5 mm resolution scan) and 1.00±0.30 kPa shear stiffness (measured as 0.82±0.12 kPa shear stiffness in 1.1 mm resolution scan and 0.85±0.17 kPa in 2.5 mm resolution scan) spherical inclusions*

At 2.5 mm resolution, the inclusion in the specification range 1.00±0.30 kPa Shear modulus is within the specified range at 0.85±0.17 kPa, but the inclusion of specification range 2.70±0.30 kPa is not in the correct range at only 1.74±0.24 kPa. At 1.1 mm resolution, the lower stiffness inclusion was calculated to have shear stiffness in the correct ranges at 0.82±0.12 kPa, and the stiffer inclusion was closer to the lower end of the manufacturer specified range at 2.12±0.07 kPa (Fig 5.3.1.1(b)). Despite not being

exactly within the manufacturer's specifications, the estimate aligns with the trend of the material properties of the phantom being on the softer side of what was specified. This alteration in measured shear stiffness in the stiffer spherical inclusion, as well as the lowered standard deviation at higher resolution, implies that increasing resolution results in more accurate shear stiffness calculations for smaller features, such as these inclusions. Additionally, this apparent softer stiffness measurement than expected based on specifications is similarly observed in Herthum, *et al.*, in which softer inclusions were more accurately estimated than stiffer ones, as was expected based on the finite-differences schemes used by inversion methods[127].

5.3.2. Human Scans

We successfully performed MRE at 7T on all subjects at all resolutions and reconstructed the data using nonlinear inversion (Figure 5.3.2.1). By applying Gadgetron reconstruction and MP-PCA denoising to the 7T data, we observed a statistically significant increase in OSS-SNR in the 2.5 mm, 1.7 mm, and 1.1 mm datasets, respectively, when compared to standard scanner reconstructed images ($p < 0.05$). All whole brain, white matter, and gray matter average values at each resolution can be found in Table 5.3.2.1, with the final OSS-SNR achieved at each resolution as 60.3±26.3, 44.8±19.1, and 16.3±5.1 at 2.5 mm, 1.7 mm, and 1.1 mm isotropic resolutions respectively, and 60.7±17.5 at 2.5 mm isotropic resolution at 3T. Consistent with the prior literature, average shear stiffness is significantly greater in white matter than gray matter at all resolutions ($p<0.001$, Table 5.3.2.1), with the average values at 1.1 mm isotropic resolution as 2.85±0.19 kPa for white matter and 2.70±0.19 kPa for gray matter.

We have also included a comparison of shear stiffness and damping ratio in the left and right hemispheres to access the possible asymmetry in MRE measures. This showed that when averaged over all subjects there is only a 0.4%, 0.5%, and 1.8% difference between the right and left hemispheres at 1.1 mm, 1.7 mm, and 2.5 mm isotropic resolution at 7T, respectively. The average absolute value percent difference in shear stiffness between the hemispheres is 6.4±3.2%, 7.2±3.9%, and 9.1±7.2% (Table 5.3.2.2) at 1.1 mm, 1.7 mm, and 2.5 mm isotropic resolution at 7T, respectively, although there are no statistically significant differences between the left and right hemisphere average stiffnesses when tested with a paired t-test

($p>0.05$). The average absolute value percent difference in shear stiffness between the hemispheres measured at 2.5 mm isotropic resolution on 3T MRI was 6.1±4.4% (Table 5.3.2.2), and there is also no statistically significant difference between the left and right hemisphere average stiffness when tested with a paired t-test ($p>0.05$).

We also acquired partial brain coverage 7T MRE data with 0.8 mm isotropic resolution, the first sub-millimeter human MRE reported, on three subjects from this previously described cohort to access the feasibility of submillimeter MRE. The results showed an acceptable average OSS-SNR of 12.9±0.9, with estimated average shear stiffness of 2.89±0.22 kPa, damping ratio of 0.26±0.01, gray matter shear stiffness of 2.79±0.13 kPa, and white matter shear stiffness of 3.00±0.29 kPa. Though the application of submillimeter MRE for the whole brain might be challenging for the patient's comfort due to the long total acquisition time, it might be beneficial for the focused biomechanical analysis of smaller brain regions, such as hippocampal subfields, which does not require whole brain acquisition.

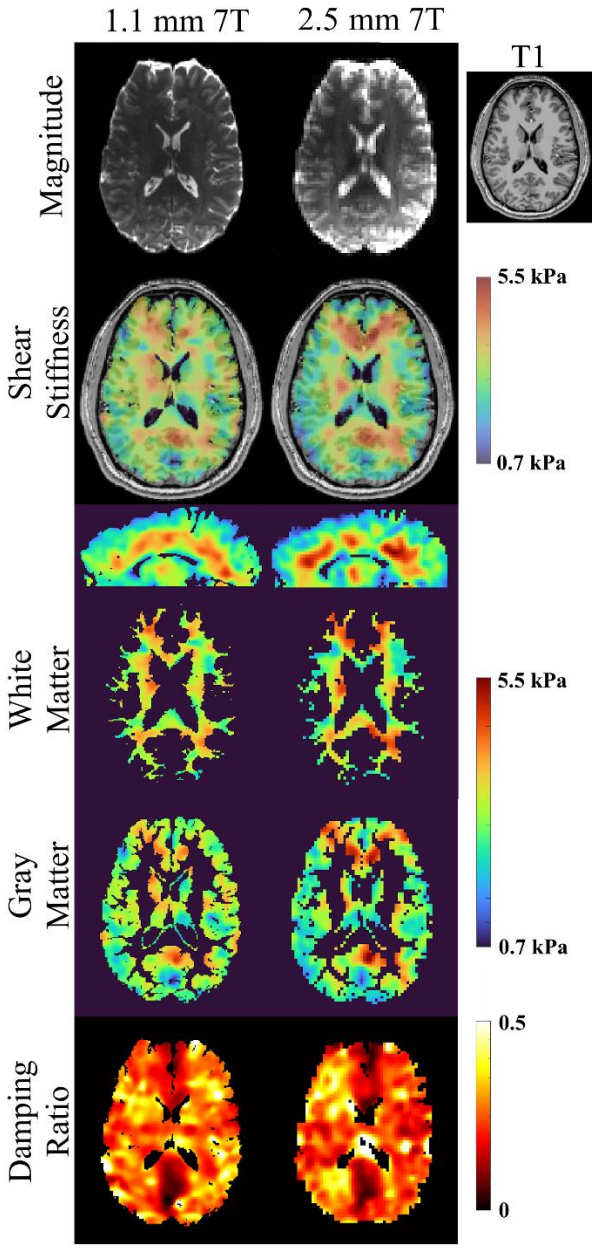

Figure 5.3.2.1. *MRE magnitude images, T1 structural, whole brain, white matter, and gray matter shear stiffness maps, and damping ratio maps, in one healthy human subject in the same slice for each resolution and field strength. The mean and standard deviation of the white matter shear stiffness for this subject is 2.65±0.51 kPa, and the associated damping ratio is 0.253±0.075.*

We observed no statistically significant difference in whole brain average shear stiffness between the 3T and 7T matched resolution datasets, as well as no significant difference in between any of the resolution groups at 7T (Table 5.3.2.1). An SSIM analysis on the matched resolution datasets resulted in an

average score of 0.873±0.058 revealing that the results were similar, but not identical (Figure 5.3.2.2). This is also exemplified by the subject-wise average percent difference between shear stiffness and damping ratio at 3T and any resolution at 7T (Table 5.3.2.2). We observe an average of 8.8-12.7%, 7.9-13.0%, and 8.6-13.1% percent differences in shear stiffness between the 2.5mm resolution 3T acquisition and the 7T acquisitions in the whole brain, white matter, and gray matter, respectively (Table 5.3.2.3).

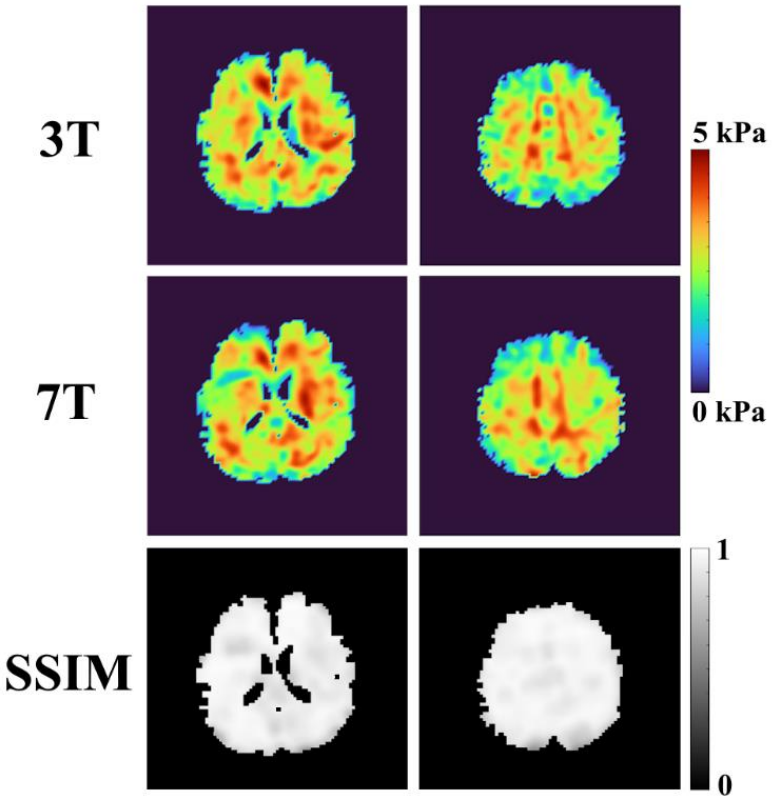

Figure 5.3.2.2 *Elastograms and SSIM analysis on two representative slices on the same subject at 2.5 mm isotropic resolution at both 3T and 7T*

As all groups are above the acceptable OSS-SNR limit (> 3)[91], we see no dependence of SNR and shear stiffness. From our repeatability analysis (one person scanned three times over the course of one week), we have a coefficient of variation of 1.88%, 9.24%, and 5.78% in the 1.1 mm, 1.7 mm, and 2.5 mm resolution groups, respectively, for shear stiffness. For the two scans performed on the same day approximately 2 hours apart, the coefficient of variation for shear stiffness across all resolutions was 3.30%.

Over all the scanning sessions and resolutions, we have a coefficient of variation of 6.48% for shear stiffness.

Table 5.3.2.1. *Whole Brain, White Matter, and Gray Matter Averages for Each Resolution with Advanced Reconstruction and Denoising Applied Concurrently (Average ± Standard Deviation, *16 subjects only)*

Whole Brain				
Resolution	2.5 mm	1.7 mm	1.1 mm	2.5 mm (3T)*
Shear stiffness (kPa)	2.68±0.26	2.62±0.16	2.73±0.19	2.52±0.20
Damping ratio	0.25±0.03	0.26±0.02	0.27±0.03	0.25±0.03
OSS-SNR	63.5±25.8	43.4±19.3	16.5±5.3	60.7±17.5
White Matter				
Shear stiffness (kPa)	2.76±0.26	2.70±0.16	2.84±0.19	2.58±0.21
Damping ratio	0.25±0.02	0.26±0.02	0.27±0.03	0.25±0.03
Gray Matter				
Shear stiffness (kPa)	2.63±0.25	2.56±0.16	2.70±0.19	2.48±0.20
Damping ratio	0.25±0.03	0.27±0.02	0.27±0.03	0.25±0.03
Percent Difference Between Gray and White Matter				
Shear stiffness	4.72±2.10%	5.52±1.88%	5.40±1.57%	4.08±1.37%
Percent Difference Between Left and Right Hemisphere				
Shear stiffness	9.14±7.28%	7.20±3.95%	6.43±3.17%	6.07±4.41%
Damping Ratio	6.97±4.62%	6.17±3.87%	6.90±4.63%	8.34±7.28%

Table 5.3.2.2. *7T Whole Brain, White Matter, and Gray Matter Average Percent Difference from 2.5 mm Resolution 3T for Each Resolution (Average ± Standard Deviation, 16 subjects only)*

Whole Brain			
Resolution	2.5 mm	1.7 mm	1.1 mm
Shear stiffness	10.7±8.7%	8.8±5.7%	12.7±6.6%
Damping ratio	8.3±7.9%	9.5±6.8%	10.3±6.4%
White Matter			
Shear stiffness	10.4±9.2%	7.9±6.5%	13.0±6.8%
Damping ratio	7.4±7.1%	8.6±6.7%	9.2±6.2%
Gray Matter			
Shear stiffness	10.8±8.6%	8.6±5.6%	13.1±7.5%
Damping ratio	8.5±7.8%	9.4±6.3%	10.0±6.1%

Addressing symmetry, when averaged over all subjects there is only a 0.4%, 0.5%, and 1.8% difference between the right and left hemispheres (at 1.1 mm, 1.7 mm, and 2.5 mm isotropic resolution at 7T, respectively), meaning that if we were to make an atlas of all the data we collected in this study, the

atlas would be left-right symmetrical. The average absolute value percent difference in shear stiffness between the hemispheres is 6.4±3.2%, 7.2±3.9%, and 9.1±7.2% at 1.1 mm, 1.7 mm, and 2.5 mm isotropic resolution at 7T, respectively, although there are no statistically significant differences between the left and right hemisphere average stiffnesses when tested with a paired t-test. The 2.5 mm isotropic resolution collection's average absolute value percent difference in shear stiffness between the hemispheres was 6.1±4.4%, and there is also no statistically significant difference between the left and right hemisphere average stiffness when tested with a paired t-test. Our post-processing steps endeavor to remove asymmetries in phase images that may result from the asymmetries in the static magnetic field and magnetic gradients, and we have accounted for any inherent image asymmetries.

We chose not to perform interpolation or other spatial comparison between resolutions, as the down-sampling or up-sampling methods introduce their own biases, however, global averages of whole brain tissue may not be the best way to address that comparison. Given that there is little precedent for performing left-right hemisphere asymmetry statistical analysis on MRE data, we have modeled the additional analysis performed here after that performed in the Supplementary Materials of Johnson, *et al*. from 2016 in *Human Brain Mapping*[128], but with the small regions we investigated for our contrast analysis (described in the subsequent Section). We have compiled unilateral shear stiffness and damping ratio for each structure, along with the effect size and p-value from paired t-tests comparing left and right structures Tables 5.3.2.3 and 5.3.2.4.

We found no significant differences and generally small effect sizes, comparable to the analysis performed in Johnson, *et al*. (2016, *Human Brain Mapping*)[128]. An analysis like SSIM or a pixel-wise correlation analysis was not performed (where the left hemisphere was mirrored on top of the right), as the inherent differences in gyri and sulci patters in the left and right hemispheres in the brain would skew the results considerably. As a demonstration of this, we performed such an analysis our T1-weighted structural images. We flipped and coregistered the structure of the left hemisphere to that same space as the right hemisphere, and found an average SSIM value of 0.24±0.05, meaning that the images are not the same and

not well correlated. Hence why we looked at small structures that are historically structurally symmetrical, as described above and by Johnson, et al.

Table 5.3.2.3. *Population statistics for shear stiffness for unilateral left and right small structures, with effect size and p-value from paired t-tests*

	Shear Stiffness (kPa)		p-value	Cohen's d
	Left	Right		
Caudate	3.34±0.55	3.34±0.42	0.961	0.008
Corpus Callosum	3.10±0.61	3.44±0.54	0.071	0.582
Hippocampus	2.77±0.55	2.75±0.51	0.538	0.043
Putamen	3.69±0.45	3.60±0.35	0.343	0.221
Thalamus	3.70±0.53	3.62±0.46	0.407	0.155

Table 5.3.2.4. *Population statistics for damping ratio for unilateral left and right small structures, with effect size and p-value from paired t-tests*

	Damping Ratio		p-value	Cohen's d
	Left	Right		
Caudate	0.274±0.033	0.278±0.047	0.643	0.108
Corpus Callosum	0.245±0.054	0.226±0.049	0.215	0.367
Hippocampus	0.243±0.042	0.231±0.055	0.346	0.255
Putamen	0.247±0.039	0.259±0.047	0.304	0.292
Thalamus	0.249±0.029	0.241±0.032	0.092	0.245

5.3.3. 7T MRE in Small Brain Regions

Due to technical limitations of our 3T MRE sequence, we were unable to capture images at 1.1 mm isotropic resolution at 3T. Attempting to decrease the voxel size by that amount increased the TE and scan time greatly, and required significant sequence acceleration, increasing noise to an unacceptable level. In addition to the resolution that one is able to achieve, we believe that one of the main benefits of implementing MRE at 7T is the resulting ability to pair it with other high resolution 7T sequences such as DTI, high resolution structural scans, spectroscopy, or SWI.

We have here, included a stiffness comparison and stiffness contrast analysis between anatomical structures (Tables 5.3.3.1 & 5.3.3.2). Running a repeated-measures ANOVA between resolutions for each anatomical structure and global white matter, there is a significant difference ($p<0.05$) between resolutions in shear stiffness for each of structures shown, as well as between the structures shown and global white matter. There is, however, no significant difference in damping ratio between resolutions for each of the

structures shown. It should be noted that the standard deviations in these homogenous white matter structures are lower at the higher resolution, implying that we see less variation in these regions likely due to partial volume effects. We also observe this in our earlier phantom experiments, where the standard deviation in shear stiffness in the stiff spherical inclusion is less at 1.1 mm isotropic resolution (0.07 kPa) than at 2.5 mm isotropic resolution (0.24 kPa).

Table 5.3.3.1. *Average shear stiffness and damping ratio at low and high resolution of 7T MRE performed in a selection of small anatomical structures*

Resolution	2.5 mm* (3T)	2.5 mm	1.1 mm
Caudate	2.73±0.33	3.18±0.47	3.37±0.43
Corpus Callosum	3.01±0.31	3.13±0.49	3.34±0.35
Hippocampus	2.13±0.52	2.59±0.49	2.80±0.48
Putamen	3.41±0.35	3.70±0.57	3.71±0.35
Thalamus	2.68±0.42	3.34±0.61	3.70±0.46
Damping Ratio			
Caudate	0.290±0.044	0.277±0.034	0.265±0.039
Corpus Callosum	0.185±0.042	0.226±0.050	0.222±0.031
Hippocampus	0.239±0.046	0.224±0.048	0.235±0.038
Putamen	0.227±0.051	0.242±0.042	0.250±0.034
Thalamus	0.228±0.039	0.248±0.041	0.244±0.027

Table 5.3.3.2. *Average shear stiffness contrast between structures at low and high resolution of 7T MRE*

Shear Stiffness Contrast			
Resolution	2.5 mm* (3T)	2.5 mm	1.1 mm
Caudate vs WM	0.075±0.129	0.175±0.163	0.189±0.156
Corpus Callosum vs WM	0.179±0.098	0.144±0.148	0.179±0.119
Hippocampus vs WM	-0.145±0.225	-0.060±0.156	-0.020±0.156
Putamen vs WM	0.339±0.136	0.333±0.155	0.297±0.117
Thalamus vs WM	0.055±0.159	0.216±0.131	0.291±0.141
Caudate vs GM	0.146±0.146	0.235±0.186	0.267±0.175
Corpus Callosum vs GM	0.255±0.116	0.202±0.161	0.256±0.140
Hippocampus vs GM	-0.095±0.231	-0.012±0.169	0.043±0.163
Putamen vs GM	0.425±0.158	0.400±0.171	0.381±0.126
Thalamus vs GM	0.124±0.181	0.278±0.153	0.375±0.154
Caudate vs Putamen	0.261±0.178	0.146±0.133	0.108±0.092

We also performed within-resolution repeated-measures ANOVAs with multiple comparisons and Bonferroni Correction to compare shear stiffness between the small white matter structures and the total

white matter (Significance level p<0.003333, Table 5.3.3.3). Generally, as the image resolution increases from 2.5 mm to 1.1 mm, the number of small white matter features that are distinguishable from each other is greater.

Table 5.3.3.3. *Repeated Measures ANOVAs with multiple comparisons and Bonferroni correction to compare the shear stiffness of small structures within resolution groups (significance level as p<0.003333, where significance is indicated by a gray cell)*

2.5 mm Isotropic Resolution

	CC	Hippocampus	Putamen	Thalamus	White Matter
Caudate	0.5907	0.0003	0.0001	0.2128	0.0001
CC	0	0.0005	0.0003	0.1342	0.0005
Hippocampus		0	1.053×10^{-7}	2.391×10^{-6}	0.3325
Putamen			0	0.0052	1.246×10^{-8}
Thalamus				0	1.425×10^{-5}

1.7 mm Isotropic Resolution

	CC	Hippocampus	Putamen	Thalamus	White Matter
Caudate	0.8143	3.323×10^{-5}	0.0008	0.0018	0.0001
CC	0	0.0001	0.0062	0.0068	3.296×10^{-6}
Hippocampus		0	4.940×10^{-7}	3.573×10^{-8}	0.0644
Putamen			0	0.6983	7.112×10^{-8}
Thalamus				0	1.211×10^{-6}

1.1 mm Isotropic Resolution

	CC	Hippocampus	Putamen	Thalamus	White Matter
Caudate	0.9936	0.0008	0.0004	0.0021	2.159×10^{-5}
CC	0	0.0001	0.0042	0.0003	7.821×10^{-7}
Hippocampus		0	1.179×10^{-7}	7.467×10^{-10}	0.8678
Putamen			0	0.5952	8.035×10^{-10}
Thalamus				0	1.701×10^{-8}

5.4. 7T MRE Discussion and Conclusions

In this work, MRE was successfully implemented at multiple resolutions at 7T using a custom pneumatic actuator and motion sensitive single-shot EPI-based sequence, with advanced post-processing and nonlinear inversion algorithm to accurately calculate the mechanical properties of the brain and its substructures at high resolution. In using our custom elasticity phantom, we validated the accuracy of our sequence and proposed post-processing procedures. We have confirmed that in a linearly elastic material with no known complex microstructure, there are no inherent differences when upgrading to high resolutions at 7T. Using phantom scans, we also investigated the benefits of higher resolution to resolve

small structures, *e.g.*, the spherical inclusions. While we achieved a measurement of shear stiffness within the manufacturing specifications of the softer inclusion at both 2.5 mm and 1.1 mm resolutions, a shear stiffness closer to the manufacturing specifications for the stiffer inclusion at 1.1 mm isotropic resolution was found. We hypothesize that this is due to the larger difference between the background shear modulus (1.70 kPa) and the modulus of the stiffer inclusion (2.70 kPa) compared to the softer inclusion (1.00 kPa). The higher resolution acquisition can better resolve the changes in wavelength and wave speed between materials of different mechanical properties, therefore achieving a more accurate measurement even when tissue types that are beside each other are different. This is also exemplified in Figure 5.3.1.1, where the edges of the spherical inclusions appear sharper at 1.1 mm resolution compared to at 2.5 mm. There is, additionally, still no significant difference in apparent shear stiffness of the background shear modulus in the phantom between resolution groups despite the lower OSS-SNR, as these values were still above the recommended threshold for accuracy of 3.0 as determined by McGarry, *et al.*[91].

Although moving to higher resolution at 7T can theoretically decrease vibrational motion sensitivity, we found similar intra-subject vibrational amplitudes across all scan types, with the largest variability being inter-subject. In all resolution groups, overall, using advanced reconstruction with Gadgetron framework and applying denoising significantly increases OSS-SNR. Taking into consideration the scan duration for each resolution, phantom validation results, and average OSS-SNR after the advanced reconstruction techniques, we have established 1.1 mm isotropic resolution as the most suitable and robust for MRE at 7T to accurately calculate the viscoelastic properties of the whole human brain. While higher resolution with the current sequence and post-processing algorithm is possible, this would increase scan time and make the scan uncomfortable for participants and therefore more prone to motion artifacts.

Despite no group differences in whole brain average shear stiffness between the 3T and 7T matched resolution datasets, as well as no significant difference in between any of the resolution groups at 7T, the results were not identical. Specifically looking at the differences in matched resolution between 3T and 7T through the SSIM analysis, many subjects were scanned on different days, which decreases the repeatability

of the result according to our repeatability analysis. To clarify the differences found, we identified a same-scanner, same-day 1.5-2.5 % test-retest variation, a same-scanner, different-day 5.5-7.5% test-retest variation, and a different-scanner, different-day 7-13% test-retest variation. While our same-scanner, same-day test-retest variation is similar to that of other human brain MRE studies[32,109,128–130], different-day test-retest analysis is rarely performed for MRE and, to our knowledge, has not been reported for human brain MRE. Currently, the only clinical/commercial application of MRE is in the detection of liver fibrosis in which the acceptable level of variation is set at 7% for commercial use for same-scanner, within-7 day test-retest analysis (via the MRE QIBA Profile)[131]. However, the scale at which liver fibrosis alters liver stiffness is much larger than any changes we have seen in the stiffness of brain tissue as it relates to neurological disorders like dementias or multiple sclerosis. There was, however a very recent study investigating multi-site and multi-scanner test-retest repeatability of phantom stiffness measurement using the various commercial MR Elastography devices, sequences, and software. This study found a 7.0% (95% CI: 2.9, 11.2) variation using the same sequence at different sites on the same elastography phantoms[132], which is consistent with the differences we found in the human brain. This would then indicate that our study's level of variation is considered acceptable. Based on the results from the multi-site phantom study and this study, consistency in sequence and scanner appear to be very important for consistency in data between subjects. Therefore, when proposing a clinical study investigating differences between healthy controls and a patient population, either all subjects should be scanned on the same scanner with the same protocol, or the scanner used should be included as a covariate.

Current MRE studies investigating clinical populations are comparatively small and use the same site, scanner, and protocol within each paper. While we don't see as large of a difference between healthy and diseased tissue as we would in the liver, studies investigating the difference between Alzheimer's patients and healthy controls have found a 8-26% difference depending on the brain region[133]. Similar differences were found between healthy controls and patients with normal pressure hydrocephalus (11-24%) [133]. Given all these levels of change due to clinical pathologies in previous studies with similar same-

day test-retest variation, we can establish that our sequence and post-processing procedure would be able to discriminate between healthy tissue and pathology, like Alzheimer's disease or mild cognitive impairment.

Since what stiffness and damping ratio in the brain "actually" represents is still not fully understood, it is clear that (at least with the current state of the field) we cannot use brain MRE alone to diagnose or assess clinical disorders. It is unlikely that the use of brain MRE alone will be used in the future to diagnose an individual based on a quantitative stiffness range that is available for the liver due to inter-subject variability based on age, sex, and other characteristics. This result implies that further studies are required to investigate the day-to-day changes in brain stiffness or how brain stiffness may change throughout the day, similar to other physiological phenomena that are observable through MRI. For example, cerebral blood flow velocity has a daily rhythm, where it is lower in the morning than the afternoon or evening, and is hypothesized to be related with sleep-associated processes[134]. As prior investigations have shown correlations between cerebral blood flow and shear stiffness[135], this may influence our results. Alternatively, subject hydration, intracranial pressure, or amount of sleep may also contribute to daily fluctuations in brain shear stiffness, as these factors have been shown to have effects on the results of other MRI sequences such as BOLD or fMRI. [136–140].

Unlike previous investigations, including in the previous Chapter[24,29,34,35,93,104,111,115,117], we saw no statistically significant difference between whole brain shear stiffness between resolution groups despite the results not being identical. The trend of decreased apparent stiffness values with increasing resolution when employing a direct inversion method was also specifically identified by Barnhill, *et al.*[34] and Marshall, *et al.*[35] in the same subject populations, who hypothesized that a different distribution of features is being captured at high-resolution[34]. It was further hypothesized that higher resolution scans, which capture fine features and interfaces not visible at low resolution, produce lower elasticity estimates due to these finer features creating more tortuosity in the wave[34,111]. Neither of these studies, however, investigated the effect of SNR, post-processing techniques, or inversion method, nor did they investigate matched resolution scans

between field strengths, so the lack of controlled variables made it difficult to support this hypothesis further. The difference in our findings can be attributed to a variety of factors. For example, by acquiring data at multiple resolutions, including matching the 3T acquisition resolution, we remove any bias that up-sampling or down-sampling may introduce. Also, by ensuring that each individual's OSS-SNR were above the accuracy threshold of 3.0 and that all acquisitions had a similar vibrational amplitude range, we maximize data quality for inversion processing. This investigation is the first to utilize nonlinear inversion on 7T data, and is the first to investigate the difference between 3T and 7T using such an algorithm, so this is likely a large contributing factor.

Advanced processing techniques such as rigid body motion correction to phase images, B_0 correction, and distortion corrections are not incorporated into the proposed framework but may be considered in the future. Rigid body motion correction is partly addressed in the current framework by removing the 0 Hz component of motion during the Fourier decomposition step and EDDY-QC correction to MRE magnitude images, although a prior investigation utilized an SPM-based realign routine, resulting in sharper looking images[93]. In MRE with EPI readout, typically, B_0 and geometric distortion correction are interrelated, as B_0 inhomogeneities result in said geometric distortions[93]. This technique, however, requires either an additional B_0 field map at the time of data collection or additional acquisition with reversed encoding directions[93,107], and while this correction appears quite significant in simulations, its effect is less so *in vivo*[107]. While Gadgetron has a functionality to perform B_0 correction without such a field map, this algorithm has not been applied. Generally, the potential corrections were not implemented at this time, as to not introduce additional controlled bias, as they have not been shown to be accurate in correction of average stiffness values[107].

Additionally, one potential drawback of using a denoising technique is the possibility of an artificially increased OSS-SNR due to the general removal of higher order components[108,109]. This effect has been observed when using filtering such as Gaussian or Median filtering[94,96,98–100,109–111], which also result in the blurring of fine physiological features. However, the MP-PCA method aims to remove only

the noise without interfering with the signal itself (*i.e.*, without blurring features)[112]. The denoising algorithm is additionally applied in local patches without assumptions on noise levels. Therefore, under the assumption smoothly varying noise maps (*i.e.*, noise being constant within a local patch), the denoising can be used on data with spatially varying noise levels[108] and estimate such noise maps accordingly[113]. Just like smoothing, the MP-PCA will not correct the signal offset due to non-Gaussian MR signals, as the algorithm removes random signal fluctuations without interfering with the signal[112,113]. Therefore, the average signal is not altered. If the data are non-Gaussian distributed (*e.g.*, Rician), then the noise will be removed, but the Rician noise floor will be preserved.

In conclusion, we have demonstrated the accuracy and robustness of high-resolution whole brain 7T MRE with an advanced post-processing pipeline and nonlinear viscoelastic inversion. Capturing finer viscoelastic features with higher imaging resolutions can be investigated further in future studies by utilizing heterogeneous phantoms with known mechanical properties and by analyzing differences in smaller brain regions, which is one of the goals of using such high-resolution scans. The developed techniques will be used in future studies to investigate biomechanical parameters of small volume brain sub-structures with applications in neurodegenerative diseases and other relevant neurological disorders.

5.5. Determining the Relationship between DTI and MR Elastography metrics in Highly Anisotropic White Matter Structures at 7T

5.5.1. Methods

On the same cohort from Chapter 4 and earlier in this Chapter, we also performed a high-angular-resolved (HARDI) diffusion-weighted imaging sequence (dMRI) that allows us to acquire brain images with 1.05 mm isotropic resolution (b=1500 s/mm^2, reversed-phase encoding in anteroposterior and posteroanterior directions for paired acquisition in 68 directions) with a total acquisition time of 20 minutes. The dMRI pre-processing was performed using the human connectome project (HCP) pipelines, adjusted to account for significant eddy currents. The pre-processing pipeline included skull-stripping, eddy current correction using FMRIB Software Library (FSL) (www.fmrib.ox.ac.uk/fsl), correction of gradient non-linearities using the HCP, B0-field inhomogeneity correction and co-registration to the structural images from the

Freesurfer pipeline[141]. This allowed to estimate whole brain maps of Radial Diffusivity (RD) and Fractional Anisotropy (FA).

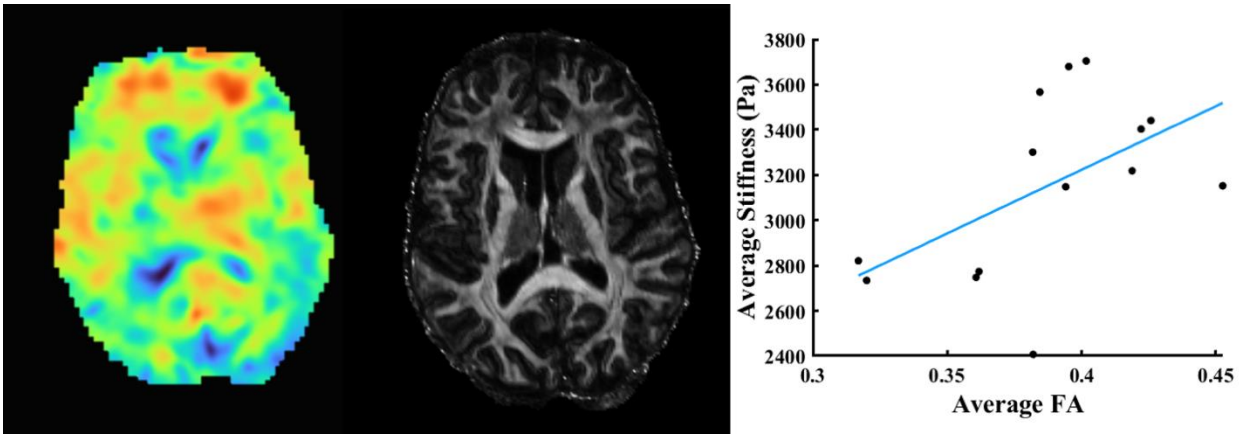

Figure 5.5.1.1. *Overview Figure showing (from left to right) MR Elastography Shear Stiffness and Fractional Anisotropy in the same subject, and the Significant ($p<0.05$) correlation between Average Shear Stiffness and FA in the Superior Longitudinal Fasciculus.*

Segmentation of individual structures in the white matter, specifically the body, genu, and splenium of the corpus callosum, the anterior, posterior, and superior corona radiata, and the superior longitudinal fasciculus, was performed using the ICBM-DTI-81 white matter atlas and parcellation map[142]. Registration of the ICBM-152 template to the DTI and MRE image spaces was performed using SPM12[106] and the same transformation was applied to the masks generated by the white matter atlas. Region-wise correlations between Shear Stiffness or Damping Ratio to FA or RD were performed to determine the relationship between MRE metrics and DTI metrics of these highly anisotropic brain regions.

5.5.2. Results

We found a significant positive correlation between FA and Shear Stiffness in the superior longitudinal fasciculus, with trending correlations in the body of the corpus callosum, the full corpus callosum, and the superior corona radiata. We also found significant negative correlations between FA and Damping ratio in the body of the corpus callosum and the full corpus callosum. We found significant negative correlations between RD and Shear Stiffness in the superior corona radiata and the superior longitudinal fasiculus, as

well as significant positive correlations between RD and damping ratio in the body of the corpus callosum and the full corpus callosum.

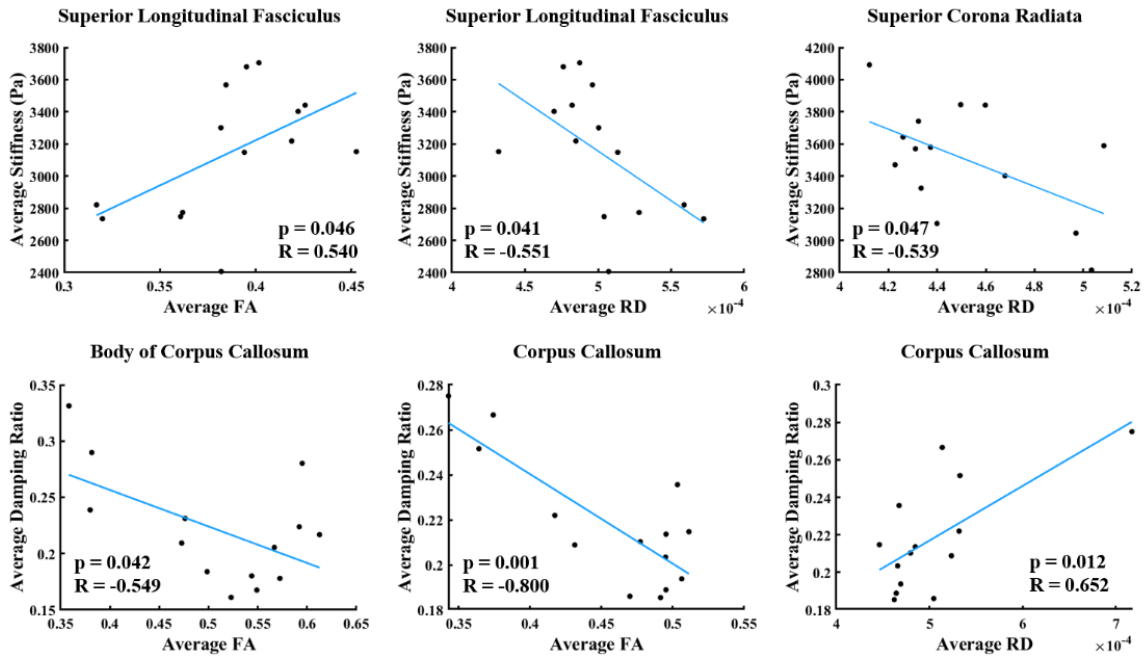

Figure 5.5.2.1. *Selected Significant Correlations ($p<0.05$) Between Average Stiffness and FA or RD (top row) and Average Damping Ratio and FA or RD (bottom row).*

Table 5.5.2.1. *Correlation Coefficients and p-values of FA, MD, or RD and Shear Stiffness for Each Brain Region. There is a significant positive correlation (p<0.05, bolded) between FA and Shear Stiffness in the superior longitudinal fasciculus, with trending correlations in the body of the corpus callosum, the full corpus callosum, and the superior corona radiata. There are also significant negative correlations (p<0.05, bolded) between RD and Shear Stiffness in the superior corona radiata and the superior longitudinal fasiculus.*

Brain Region	**FA & Shear Stiffness**		**RD & Shear Stiffness**	
	R	**p-value**	**R**	**p-value**
Gray Matter	0.028	0.925	-0.214	0.462
White Matter	0.304	0.290	-0.357	0.210
Corpus Callosum (Body)	0.489	0.076	-0.526	0.053
Corpus Callosum (Genu)	0.322	0.262	-0.327	0.254
Corpus Callosum (Splenium)	0.167	0.568	-0.348	0.223
Corpus Callosum	0.482	0.081	-0.527	0.053
Corona Radiata (Anterior)	-0.035	0.905	0.100	0.734
Corona Radiata (Posterior)	0.019	0.949	-0.014	0.963
Corona Radiata (Superior)	0.497	0.071	**-0.539**	**0.047**
Corona Radiata	-0.185	0.526	0.149	0.612
Superior Longitudinal Fasciculus	**0.540**	**0.046**	**-0.551**	**0.041**

Table 5.5.2.2. *Correlation Coefficients and p-values of FA or RD and Damping Ratio for Each Brain Region. There are significant negative correlations (p<0.05, bolded) between FA and Damping ratio in the body of the corpus callosum and the full corpus callosum. There is also a significant positive correlation (p<0.05, bolded) between RD and damping ratio in the body of the corpus callosum and the full corpus callosum.*

Brain Region	**FA & Damping Ratio**		**RD & Damping Ratio**	
	R	**p-value**	**R**	**p-value**
Gray Matter	-0.193	0.508	0.351	0.218
White Matter	-0.275	0.341	0.332	0.247
Corpus Callosum (Body)	**-0.549**	**0.042**	**0.652**	**0.012**
Corpus Callosum (Genu)	-0.398	0.159	0.062	0.833
Corpus Callosum (Splenium)	0.035	0.904	0.096	0.745
Corpus Callosum	**-0.800**	**0.001**	**0.677**	**0.008**
Corona Radiata (Anterior)	-0.239	0.411	0.210	0.472
Corona Radiata (Posterior)	-0.020	0.947	0.139	0.637
Corona Radiata (Superior)	-0.365	0.199	0.393	0.164
Corona Radiata	-0.157	0.593	0.229	0.431
Superior Longitudinal Fasciculus	-0.163	0.578	0.211	0.468

5.5.3. Discussion and Conclusions

Our correlation between FA and MRE metrics implies greater stiffness and lower energy dissipation across the volume in small regions where the uniform directionality of the white matter fibers is high. This indicates the need for anisotropic viscoelastic inversion specifically in these areas of the brain. Alterations in the correlation between metrics in these areas may be indicative of damage to the white matter microstructure. While it is possible that the correlation between RD and MRE metrics are related to axon density, this remains under investigation.

While correlations between the DTI metrics of FA and RD, and MRE metrics of Shear Stiffness and Damping Ratio are not apparent in larger structures, the high resolution achieved at 7T for both MRE and DTI allows us to investigate these relationships in small, highly anisotropic, brain regions. Changes in these

metrics or the relationships between these metrics could signal changes in microstructure indicative of damage to white matter microstructure.

Chapter 6: MRE as a Biomarker for Alzheimer's Disease and for Exploration of Healthy Brain Aging

6.1. Introduction

Alzheimer's disease (AD) is a progressive neurodegenerative disease that is characterized by abnormal deposits of amyloid plaques and intracellular neurofibrillary tangles of the protein Tau in the cortex, or gray matter, of the brain[143]. Over time, this damage causes the connections between neurons to be lost and those neurons to die over time. According to the World Health Organization, 10 million new cases of dementia occur per year, 60-70% of which are Alzheimer's Disease[144]. Around 1/3rd of the US population over 85 years old will develop Alzheimer's Disease, and it's one of the top 5 leading causes of death with the survival estimate being 3-9 years after diagnosis[144]. Neuronal loss initially occurs in the temporal lobe before progressing to the precuneus region[145]. This, as well as thinning, initially occurs in the gray matter throughout the brain before moving to the superficial white matter[146]. Over the progression of AD, the damage spreads throughout the brain, shrinking the volume of the overall brain tissue[147]. Symptoms include memory loss, confusion, and cognitive difficulties[148]. Many risk factors for the development of AD have been identified such as high cholesterol, diabetes, and sleep apnea[144]. The progression of AD is typically split into three major phases or groups that begins with aggregation of amyloid, then the phosphorylation of tau, before the aggregation of p-tau in neurons[145]. The first phase of the disease is asymptomatic, where no cognitive deficits have occurred. The second stage is where patients develop mild cognitive impairment, or MCI, and there the loss of neurons begins to cause short term memory loss. The third phase is where AD is confirmed and there is short and long term memory loss, as well as hallucinations and delusions.

Amyloid deposition and progression throughout the brain is traditionally described through 'Thal Staging', with Phase 1 reflecting early deposition and Phase 5 reflecting late-stage disease[149]. In phase 1, amyloid is deposited in the frontal, parietal, temporal, and/or occipital neocortex [149]. These amyloid plaques are typically small groups of diffuse plaques and do not extend into any other brain region [149]. Phase 2 is characterized by additional neocortical plaques, deposits in the entorhinal region, and some cases of

amyloid in the amygdala, cingulate gyrus, and the neocortex of the occipital, temporal, parietal, and frontal lobes [149]. In Phase 3, amyloid is observed to have spread to multiple subcortical regions including white matter [149]. By Phase 4, amyloidosis has reached the central gray matter of the midbrain and has begun to reach the brain stem [149]. Phase 5 sees amyloid reach the cerebellum and additional brainstem nuclei [149]. Tau phosphorylation throughout the brain begins later than amyloid deposition and is described via 'Braak Staging'[150]. Stage 1 shows neurofibrillary tangles in the transentorhinal cortical region, and Stage 2 is considered an aggravation of Stage 1[150]. Stage 3 is characterized by neurofibrillary tangles in the Pre-α layer of the transentorhinal and entorhinal regions, and Stage 4 sees this extending into the hippocampus and amygdala [150]. Stage 5 is an aggravation of Stage 4 where tangles begin extending into the Pre-β and Pre-γ layers and the isocortex [150]. Stage 6 is the most severe stage with extensive tangles in all layers of the entorhinal cortical region, isocrotex, and hippocampus, and is also characterized by a marked loss of nerve cells [150].

Early diagnosis of AD is still challenging because of the subtlety of the microstructural changes it initially causes in the brain, which is particularly troubling, as most treatments for AD can only be used to slow its progression, not reverse it, and are often far more successful when started early. This is especially important because AD starts developing a decade or more before actual diagnosis with a long preclinical and mild cognitive impairment stage that lasts several years[144]. Current drug trials for AD treatment focus on amyloid clearing in these pre-clinical or early phases where pathological changes are present but before symptoms can manifest, which gives an unfortunate bias in that these studies likely include subjects who have a clinical AD diagnosis but who don't have actual AD pathology[148]. This is why this investigation, and many other new investigations, are looking to move away from defining AD clinically but instead using brain pathology and biomarkers.

The current gold standard of AD diagnosis is still the pathological analysis of tissue, however, this is not a feasible screening option given its obvious invasiveness. From pathological analysis, postmortem accumulation of amyloid and tau in the entorhinal cortex has been observed[144]. Amyloid is deposited first,

followed by tau, and this accumulation is accompanied by non-specific markers of neurodegeneration, such as atrophy in multiple characteristic regions. From this ex-vivo knowledge, there are other tests of varying degrees of invasiveness that are typically used for diagnosis in living humans. For clinical usage, cerebrospinal fluid (CSF) and blood biomarkers are gaining popularity, as are structural MRIs and different types of positron emission tomography (PET) scans. There are also other biomarkers that are currently in the research stages of development, such as functional MRI (fMRI), DTI, and MRE. Due to the heterogeneous presentation of AD, usually multiple biomarkers are investigated simultaneously to increase specificity.

PET Neuroimaging

The current in vivo gold standard diagnosis is PET neuroimaging, with the three main types being amyloid PET, tau PET, and Fluorodeoxyglucose (FDG) PET. For amyloid PET, a radioactive ligand that can cross the blood brain barrier, such as F-18 labeled Florbetaben, selectively binds to fibrillar amyloid and diffuse/dense amyloid plaques[151]. This uptake is measured during the PET scan, and because white matter and the cerebellum do not uptake this radioactive ligand, these are used as reference regions to properly scale the uptake in the cortex (quantitatively called standardized uptake value ratio, or SUVR)[152]. While the correlation between amyloid tracer uptake and cortical amyloid plaques have been confirmed via post-mortem autopsy, classic amyloid uptake is symmetric and diffuse, so uptake does not necessarily correlate with severity of symptoms[148]. Although, the parietal cortex is one of the earliest amyloid deposition sites, and progression of amyloid deposition may be influence by anatomical and functional connectivity between posterior cortices and medial temporal lobes[151,153,154]. Generally, uptake increases with increasing age, but amyloid 'positivity' is through to be indicative of future cognitive decline[148]. Amyloid positivity is defined both globally and regionally, dependent on the radioactive tracer and method used. In this work, we will be using F-18 labeled Florbetaben with the imaging method described in Bullich, et al.[151] This study also established the reference values, both as SUVR and as centiloid measurements, we will use to determine subject positivity and regional positivity with this tracer and method (listed in Table

6.1.1)[152]. One downside to amyloid PET is that these traces don't bind to less mature amyloid, which can be more neurotoxic than fibrillar[148].

Table 6.1.1. *From Bullich, et al.- Regional amyloid SUVR cutoff values for F-18 labeled Florbetaben*[151]

Cortical Region	SUVR Cutoff	Sensitivity	Specificity
Frontal	1.31	95%	97%
Lateral Temporal	1.26	97%	98%
Occipital	1.29	88%	95%
Parietal	1.26	97%	98%
Anterior Cingulate	1.43	92%	97%
Posterior Cingulate	1.47	93%	97%
Precuneus	1.28	95%	98%
Composite	1.38	93%	100%

Phosphorylated tau, on the other hand, is rarely found in asymptomatic individuals, as hyperphosphorylation of tau is a downstream event[148]. Tau is a neuronal protein that is produced throughout the nervous system and promotes self-assembly of axonal microtubules and stabilizes them[145,155,156]. Normal aging tauopathy is isolated to the medial temporal lobe, which is a non-AD pathology, and different regions of uptake are indicative of different diseases [148]. Like with amyloid PET, tau uptake has also been validated against autopsy[144,145]. Neurofibrillary tau tangle density correlates with neurodegeneration and cognitive impairment, with a close relationship between patterns of tau deposition and atrophy measures[156]. Tau imaging is also capable of detecting regionally specific patterns of tau tangle deposition that follow Braak staging the neurofibrillary tangle pathology. A common tracer for tau PET scans is ^{18}F-AV-1451, which has shown increased binding in the isocortex with worsening global cognitive function, and decreased visual and verbal function with binding in the medial temporal region[155].

Cerebral FDG uptake can also be measured using PET and is used as a measure of neurodegeneration (synaptic loss) and dysfunction in the surviving cells[144,145]. FDG uptake is proportional to glucose metabolism, and decreased cerebral uptake indicates loss of neuropil and functional impairment of neurons[148]. Hypometabolism in the in bilateral middle and inferior temporal gyri, limbic parahippocampal gyrus and posterior cingulate gyrus, and parietal lobes is associated specifically with

memory loss[148]. FDG PET is poorly correlated, however with amyloid or tau accumulation, and instead is correlated specifically with neurodegeneration[145,148]. Each neurodegenerative disease has its own characteristic FDG PET findings, but it is not a very sensitive biomarker[145]. This is also due to the fact that amyloid and tau accumulation occur before neurodegeneration (as neuronal loss is late in the pathway), so these are typically detected first[145,148].

Cerebrospinal Fluid and Plasma Biomarkers

Despite the FDA not formally approving any specific CSF biomarker for AD diagnosis, researchers and clinicians can use CSF to sample biomarkers for amyloid and tau using a spinal tap. These are the earliest biomarker changes reflecting underlying AD pathology, as these biomarkers in the CSF of cognitively normal individuals is associated with an increased risk of cognitive decline, development of MCI, and of symptomatic AD. Specifically, increased tau in the CSF is a marker of the intensity of neuronal degeneration and injury that correlates to tau load, and these tau levels can also indicate recent damage. P-tau specifically is a biomarker of the pathologic state associated with the neurofibrillary tangle formation, but p-tau cannot be used as a measure of tau deposits.

In contrast, low CSF levels of amyloid, specifically Aβ42 is a marker of fibrile amyloid aggregation, trafficking, and deposition into plaques in the brain[144]. Like the tau biomarker, it is not a measure of amyloid plaques, but as a biomarker of a pathologic state associated with amyloid plaque formation[157]. By the time a patient presents with cognitive impairment, cortical amyloid deposition is close to reaching its maximum extent. With CSF, we observe higher accuracy in diagnosis by using multiple biomarkers simultaneously. For just amyloid, looking at the ratio between Aβ42 and Aβ40 helps improve specificity[144,157]. Additionally, using a combination of Aβ42/40 ratio, total tau, and p-tau is more accurate than looking at just one of these markers alone. From a study that investigated the sensitivity of different biomarkers, a combination of these different CSF biomarkers was determined to be the most sensitive of all the biomarkers tested[157].

In an attempt to be less invasive than CSF biomarkers, blood-based biomarkers are emerging as an alternative. Analysis of blood plasma for biomarkers such as amyloid, tau, and neurofilament light chain is performed using mass spectrometry or Single Molecule Arrays (SiMoA)[144]. While not as sensitive as CSF, plasma samples have shown some ability to predict amyloid deposition in brain tissue through decreased Aβ42/40 ratio. This is still an emerging field, however, and it is unclear sensitive or specific these biomarkers will be in distinguishing between different pathologies.

MRI Neuroimaging

While PET scans can measure pathological aggregation, MRI scans can measure other pathophysiological mechanisms like structural decline (loss in volume and cortical thinning), functional decline (fMRI hyperactivity or altered network connectivity), or white matter decline (diffusion anisotropy reduction or white matter pathology)[144–146,158,159]. Additionally, while PET requires the use of tracers and ionizing radiation, MRI is a less invasive alternative. T1-weighted images can detect changes in gray matter due to the good contrast between gray and white matter. By improving spatial resolution by using high field strengths or advanced MR imaging techniques, quantitative measurements of gray matter volume, cortical thickness, and other volumetric analyses can be accomplished using tools like Freesurfer or FSL[146]. By using T1-weighted MRI scans, cortical gray matter loss greater than that of healthy aging (0.5% per year) has been correlated with greater amounts of tau tangles and with memory loss and other decreased cognitive functions[145]. Specifically, cortical atrophy in the hippocampus has been linked to the AD symptom of amnesia. High resolution structural imaging studies in AD and MCI patients have suggested that some hippocampal subfields are more susceptible to neuronal loss than others. Additionally, APOE ε4 status was associated with volumetric decline in this region[145]. However, cortical loss is nonspecific to AD and occurs late in diseases stages, so is not useful as an early screening tool. Furthermore, structural MRI alone has not been proven to be accurate enough to identify individuals with MCI who will develop AD.

In order to determine MRI-based differences between these groups, fMRI has been used to examine functional changes in MCI and early AD. fMRI is an MRI techniques that measures brain activity by

detecting changes associated with blood flow, as cerebral blood flow and neuronal activity are linked. During learning, there was increased hippocampal activity in MCI patients compared to those diagnosed with AD, with more activity in less severe MCI cases and similar level of activity to AD patients in more severe MCI cases. As with T1-weighted MRI, high resolution fMRI has also found that some subfields of the hippocampus are more affected than others, and that these changes are also correlated with APOE ε4 status[145,148].

While initial degeneration occurs in the gray matter, white matter volume and white matter integrity have been identified as being disrupted as early as preclinical AD as measured through DTI[160]. Both MCI and AD patients have been shown to have declines in white matter integrity throughout the brain with the most reliable changes reported in the temporal lobes[145,159,160]. While fractional anisotropy (FA) is used as a proxy for white matter integrity, there are many factors that affect the FA measurement such as axonal degeneration, packing density, disorganization, and demyelination[160]. In addition to changes in FA in the temporal lobe, changes in white matter connectivity due to AD have also been identified in the fornix, which is the major links between the hippocampus and hypothalamus[145,159]. Damage to the fornix has specifically been linked to learning and memory deficits that have also been attributed to hippocampal lesions[159]. It has also been hypothesized that myelin loss could contribute to changes in diffusivity in white matter, which can also be measured using DTI[159]. Elevation in mean diffusivity (MD) and decreases in FA in the medial temporal and parietal white matter have been associated with neurofibrillary tangle pathology and higher Braak stages[158]. The same changes in MD and FA have also been associated with lower cognitive scores[158]. While FA can only provide useful information about white matter, recent investigations have identified that MD may be useful in assessing microstructural alterations in gray matter. While it is not entirely clear what MD is a proxy for in gray matter, it has been hypothesized that an increase of MD in gray matter indicates a breakdown of microstructural barriers that precede volume loss[161]. This increase in the MD of gray matter in AD and MCI has been identified in the hippocampus, cingulate cortex, parieto-occipital cortex, and the temporal cortex[161].

Particularly important in this body of work, MRE-derived stiffness and damping ratio have also been recently identified as potential biomarkers for AD. From studies using MRE to investigate healthy human aging, we know that the brain gets softer from early adulthood to late adulthood at a rate of annual change of anywhere from -0.008 to -0.025 kPa per year[133]. This softening affect was found in the whole brain volume, gray matter, white matter, hippocampus, and in the frontal, temporal, occipital, and parietal lobes, while no changes were observed in the sensory motor regions and deep gray matter and white matter regions[9,10,25–27,32,162]. Additional studies investigating the effect of memory on brain stiffness showed a relationship between memory score and hippocampal stiffness and damping ratio in healthy adults, with lower memory scores correlating with lowered shear stiffness[162]. In studies comparing patients with AD to age-matched healthy controls (to account for natural age variation), significant decreases in brain stiffness in the frontal, temporal, and parietal lobes were identified, as well as in the hippocampus and global brain tissue. Not only were there group differences between AD patients and age-matched healthy controls, but brain stiffness was also found to be correlated with hippocampal volume and functional connectivity, which are used as proxies for AD severity[9,10]. Additionally, Murphy, *et al.* demonstrated that AD patient's brains were significantly softer than both amyloid positive and amyloid negative healthy controls, and that there were no significant differences in brain stiffness between the two control groups, regardless of amyloid positivity[10]. A mouse model study found a negative correlation between CSF amyloid load and whole brain shear stiffness, but this has yet to be investigated in humans[163]. Two studies investigating different types of dementias reported different areas of softening dependent on the type of dementia the patient was diagnosed with, but small sample sizes made it difficult to determine if the groups could be discriminated with just MRE measurements alone[13,27].

6.2. Creating a Framework for PET and MRE Correlation from Healthy Older Adults

6.2.1. Introduction

As described in the Chapter introduction, early diagnosis of AD is still challenging because of the subtlety of the microstructural changes it initially causes in the brain, which is particularly troubling, as most treatments for AD can only be used to slow its progression, not reverse it, and are often far more

successful when started early. Pivotal studies applying MRE have shown a progressive softening of white and gray matter tissue in AD patients compared to healthy controls (especially in the frontal, parietal and temporal lobes) in line with the known topography of AD pathology[10,26]. This implies the future use of MRI and MRE metrics to track disease progression and as a tool for AD diagnosis, potentially replacing methods that require patients to undergo ionizing radiation on a regular basis.

Although MRE studies on AD patients have identified tissue softening[10,26], there might be different spatiotemporal effects of tau and amyloid beta on brain tissue mechanics due to the intracellular and extracellular nature of their deposition. There might be competing effects of tissue atrophy and plaque formation on the measured brain mechanical properties. Therefore, one of the limitations of using MRE on AD patients is the lack of understanding of microstructural causes that induce tissue viscoelasticity variations. This difficulty limits the current predictive value of MRE for early diagnosis and for the assessment of individual risk of developing cognitive decline. To overcome this challenge, in this pilot study, we developed a novel framework for performing 7T MRE at high resolution on subjects who have previously undergone PET scans, and performing joint analysis of biomechanical and pathologic markers on these subjects. This approach has the potential to provide physical understanding regarding the meaning of these MRE parameters in the context of dementia and neurodegeneration.

6.2.2. Methods

Full brain coverage MRE (using our custom SE-2D-EPI-based sequence[37]) was performed on six healthy human subjects (Avg. age 73.2 years) at 1.1mm isotropic resolution and 50Hz vibration frequency[31], using a 32-channel head coil (Nova Medical) on a 7T Siemens Magnetom MRI scanner (TR/slice=140ms, TE=65ms, GRAPPA=3, Partial Fourier 7/8). Raw data were collected for each of these scanning sessions, and images were reconstructed post-hoc using Gadgetron to reduce the occurrence of phase singularities often found in standard reconstructions of this type. Images were denoised using a MP-PCA algorithm[5] and unwrapped using Segue 4D unwrapping[101]. Curl filtering, Fourier decomposition, and a quartic smoothing kernel[7] were used to acquire wavefield images, before Algebraic Inversion of the Helmholtz Equation was

used to calculate the complex shear stiffness[164] (further described in Section 4.2). T1 images were segmented using Freesurfer and co-registered to the magnitude images of the MRE acquisition such that a transformation matrix was generated. This transformation matrix was then applied to the masks to be directly applied to the calculated elastograms.

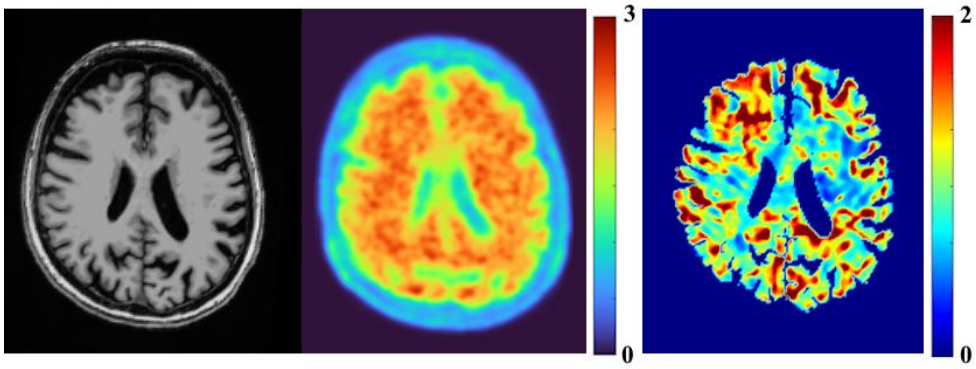

Figure 6.2.2.1. *From left to right, T1, PET SUVR map, and Elastogram (|G*|, kPa) for the Same Subject in the same image space.*

These six subjects have also previously undergone a Aβ burden measurement with F18–labeled florbetaben simultaneous positron emission tomography and magnetic resonance (PET-MR) imaging on a Siemens Biograph mMR using standardized protocols in accordance with FDA labeling instructions. Attenuation-corrected data from 90-110 minute post-injection are measured in 1-minute windows and corrected for motion. PET data are expressed as a selective uptake value ratio (SUVR) (Figure 6.2.2.1). These PET images were also co-registered to the T1 images captured during the 7T MRI scanning session and previously generated Freesurfer masks applied.

6.2.3. Preliminary Results and Discussion

Using 7T neuroimaging and advanced signal processing techniques, we have successfully created a framework for measurement of high-resolution brain mechanical properties. Average Loss Modulus, Storage Modulus, and SUVR for each brain region for each subject was calculated and can be found listed in Table 7.2.3.1. A regression for each brain region between average SUVR and average Loss and Storage Modulus was also performed. The correlation coefficients and p-values for each brain region can be found in Table 6.2.3.2.

Table 6.2.3.1. *Average SUVR, Storage Modulus (in Pa), and Loss Modulus (in Pa) for Each Brain Region (Mean ± Standard Deviation). OSS-SNR was also calculated for MRE measures to ensure SNR was high enough for accurate stiffness reconstruction (OSS-SNR > 3).*

Nucleus	**PET SUVR**	**Storage Modulus (Pa)**	**Loss Modulus (Pa)**
Cerebellar Cortex	0.979 ± 0.049	941.9 ± 72.6	386.8 ± 75.7
Hippocampus	1.355 ± 0.074	1065.7 ± 140.5	396.8± 37.7
Entorhinal	1.167 ± 0.108	861.6 ± 227.0	338.6 ± 176.6
Parietal	1.176 ± 0.053	1034.8 ± 167.4	599.0 ± 202.0
Temporal	1.096 ± 0.050	1026.9 ± 167.9	517.3 ± 115.4
Frontal	1.286 ± 0.127	1018.2 ± 168.3	555.1 ± 172.3
Left Cerebellar Cortex	0.993 ± 0.052	948.7 ± 89.7	364.8 ± 53.0
Left Hippocampus	1.358 ± 0.091	1067.4 ± 142.8	398.3 ± 66.5
Left Entorhinal	1.204 ± 0.146	862.4 ± 243.3	355.1 ± 258.2
Left Parietal	1.211 ± 0.072	1119.4 ± 212.1	644.9 ± 261.2
Left Temporal	1.115 ± 0.057	1066.5 ± 194.1	558.1 ± 151.4
Left Frontal	1.282 ± 0.116	1021.8 ± 182.8	571.2 ± 180.5
Right Cerebellar Cortex	0.967 ± 0.053	948.4 ± 74.0	433.7 ± 114.3
Right Hippocampus	1.361 ± 0.078	1038.4 ± 186.0	383.5 ± 60.4
Right Entorhinal	1.101 ± 0.113	777.7 ± 194.1	292.7 ± 152.0
Right Parietal	1.180 ± 0.054	981.2 ± 145.6	559.1 ± 188.7
Right Temporal	1.096 ± 0.067	939.7 ± 132.4	455.8 ± 87.0
Right Frontal	1.308 ± 0.147	1014.3 ± 150.9	537.9 ± 164.3

Based on these correlation coefficients, for healthy older adults, there is a strong positive correlation between SUVR and Storage Modulus that is approaching significance in the Entorhinal cortex, as well as a strong positive correlation between SUVR and Storage Modulus and SUVR and Loss Modulus that is approaching significance in the Left Entorhinal cortex. With continued recruitment of subjects with AD and MCI, we hope to expand this method to perform joint analysis of biomechanical, connectomic and pathologic markers in AD patients and bring novel insights in our understanding of the mechanisms of AD

onset and progression. We also intend to perform voxel-wise comparisons within brain regions in the future, control for age and sex, as well as include analysis of Tau and Dopamine PET metrics as this study progresses.

Table 6.2.3.2. Correlation Coefficients and p-values of SUVR and Storage and Loss Modulus for Each Brain Region. *While none of the follow correlations reach significance, the Entorhinal cortex is approaching significance for Storage Modulus and SUVR (signified by the *). As these subjects are all healthy controls, we do not yet expect to see strong correlations between PET and MRE metrics as we would with AD or MCI subjects.*

Nucleus	**SUVR & Storage Modulus**		**SUVR and Loss Modulus**	
	R	**p-value**	**R**	**p-value**
Hippocampus	0.4510	0.3694	0.547227	0.2611
Entorhinal	0.7994	0.0563*	0.630394	0.1797
Parietal	0.6142	0.1946	0.5203	0.2900
Temporal	0.4835	0.3313	0.665784	0.1489
Frontal	0.2795	0.5917	0.26924	0.6059
Left Hippocampus	0.4076	0.4224	0.210707	0.6886
Left Entorhinal	0.7724	0.0718*	0.767875	0.0746*
Left Parietal	0.0739	0.8893	0.154204	0.7705
Left Temporal	0.3631	0.4793	0.545053	0.2634
Left Frontal	0.0891	0.8666	0.200306	0.7036
Right Hippocampus	0.5016	0.3107	0.511227	0.3000
Right Entorhinal	-0.4269	0.3986	-0.07232	0.8917
Right Parietal	0.7198	0.1067	0.565237	0.2424
Right Temporal	0.6108	0.1977	0.610555	0.1980
Right Frontal	0.4248	0.4012	0.266453	0.6098

6.3. Cross-Correlation of Biomechanical, Connectomic, and Pathological Markers in Neurodegeneration at 7T MRI

6.3.1. Introduction

As discussed previously, performing MRE on human brain can provide information on different structures within brain tissue based on their mechanical properties, and pivotal studies applying MRE have

shown a progressive softening of white and gray matter tissue in AD patients in regions in line with the known topography of AD pathology[10,26]. Another potential non-invasive diagnostic tool is diffusion tensor magnetic resonance imaging (DTI), which provides a metric for understanding the integrity of microstructure[165]. In addition to changes in signal intensity in the white matter due to aging, previous DTI studies have also identified changes in DTI signal intensity in gray matter regions[166,167], making it a region of interest to study in aging and neurodegeneration.

Additionally, studies at 3T have found correlations between MR Elastography (MRE) and DTI metrics in small white matter structures in young, healthy individuals[121,168], but low imaging resolution limited the specificity of the results in small regions due to partial volume effects.

Leveraging non-invasive ultra-high field (UHF), 7 Tesla (7T) MRI, with increased signal-to-noise ratio and improved soft tissue contrast afforded by UHF allows us to accurately map tissue microstructure. In this study we aim to use 7T MRE, 7T DTI, 3T amyloid-PET, and cognitive testing results to determine the relationships between these metrics in a cohort of older individuals with either normal cognition, mild cognitive impairment (MCI), or AD.

Figure 6.3.1.1. All Imaging Modalities Used*; T1 (left), PET (right), Bottom: FA (left), and |G*| (right) maps for one subject with MCI.*

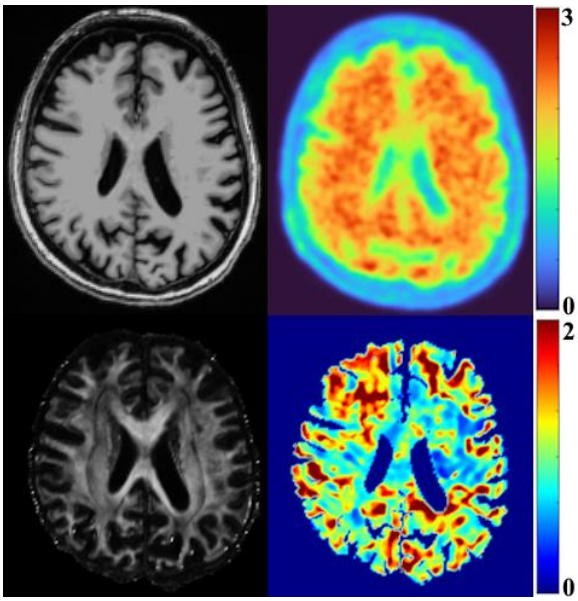

6.3.2. Methods

Two scanning sessions (7T MRI and 3T PET, Fig 6.3.1.1) and the Preclinical Alzheimer Cognitive Composite (PACC) test were performed on 14 subjects (Avg. age 70.3±5.2 years) determined to be cognitively normal (CN), and 6 subjects (Avg. age 70.0±9.4 years) determined to have MCI or AD. All MCI/AD patients have a consensus diagnosis of cognitive impairment and a Clinical Dementia Rating >4.0 in the Clinical Dementia Rating Scale Sum of Boxes. Additional subjects (7 additional healthy controls making the group Avg. Age 68±6 years and 3 additional subjects with AD or MCI making the group Avg. Age 71±9 years) underwent only the 7T MRI scanning session.

The 7T MRI (Magnetom, Siemens, Erlangen) scan, using a 32-channel head coil (Nova Medical) included, a T1-weighted MP2RAGE sequence, a high-angular-resolved diffusion-weighted imaging MRI (dMRI) sequence, and a custom SE-2D-EPI-based MRE sequence (Table 6.2.2.1). The DMRI series were collated into a single volume, denoised and corrected for artifacts and distortions using MRtrix3. Whole brain tractography was generated with 10,000 seeds using tractseg, and fractional anisotropy (FA) and radial diffusivity (RD) were calculated[141].

Full brain coverage MRE (using a custom SE-2D-EPI-based sequence[37]) was performed at 50Hz vibration frequency[31] (TR/slice=140ms). Raw data were collected and analyzed using direct inversion as described in Triolo, *et al.*[169] and Chapter 4 of this work to calculate the absolute value of the complex shear modulus (|G*|). Segmentation of brain regions was performed on an MP2RAGE T1scans (0.7mm^3) using Freesurfer 7.0[170] and regional masks were co-registered to the MRE space and DTI space using SPM12[106]. SPM12 was also used to estimate the percentage area of CSF for each region.

Table 6.3.2.1. *Imaging Parameters for the 7T and Biograph mMR Scanning Sessions*

7T Scanning Session							
Scan Type	**Resolution (isotropic)**	**TE (ms)**	**TR (ms)**	**GRAPPA**	**Partial Fourier**	**Other**	**# of Slices**
50Hz MRE (8 phase offsets)	1.1 mm	65	14000	3	7/8	**Bandwidth=** 1849 Hz/pixel	100
DWI	1.05 mm	67.6	7200	3	N/A	b = 1500 s/mm2	132
T1-Weighted MP2RAGE	0.7 mm	3.62	6000			**Bandwidth=** 130 Hz/pixel	256
Biograph mMR							
Scan Type	**Resolution (isotropic)**	**TE (ms)**	**TI (ms)**	**PAT**	**Flip Angle**		
T1-Weighted MPRAGE	1.0 mm	2.98	900	2	9º		

Using the previously described 7T acquisition with full advanced reconstruction and direct inversion (Chapter 4), we performed 7T MRE at high resolution on a larger cohort than those scanned with PET. The cohorts that we will be investigating only using 7T MRE are the cohort of 20 healthy young adults as described in Chapter 4 (Avg. age 27 ± 3 years), 9 human subjects that presented with cognitive deficits (CD, Avg. age 71 ± 9 years) and 21 age-matched ($p>0.10$) subjects with normal cognition (CN, Avg. age 68 ± 6 years). Average |G*| of each brain region listed were compared between CD and CN, and CN and young adult groups using one-tailed, unequal variance, t-tests.

Subjects also underwent a Siemens Biograph mMR simultaneous PET-MR scan to measure Aβ burden using F18-labeled florbetaben using FDA standardize protocols. Attenuation-corrected data from 90–110-minutes post-injection were measured in 1-minute intervals and motion corrected. The resulting images were coregistered to an MPRAGE T1-weighted image. Average selective uptake value ratio (SUVR), FA, MD, and |G*| were calculated per cortical region of interest as specified in Palmqvist, *et al.*[154]. All MCI/AD subjects and one CN subject were determined to be Aβ-positive. We performed multiple Shapley Regressions in subjects with amyloidosis (subjects whose average SUVR are above the region threshold as described in Bullich, *et al.*[151]) in five PET-relevant brain regions (cingulate, frontal, parietal, temporal, and palmqvist-early[154]) with combinations of the different imaging metrics and PACC that were acquired for

each subject. In order to determine the relative importance of each of our predictor variables to either SUVR or |G*|, each Shapley regression was performed twice for each region of interest.

6.2.3. 7T MRE Results

Investigating differences between CN and CD groups in regional averages of |G*|, we observe a significant decrease in |G*| in each brain region apart from the EC (12.6% decrease in WB*, 13.0% in GM*, 14.8% in WM*, 19.1% in FL*, 15.0% in PL*; 19.6%** in TL, and 17.9% in HC**; *p<0.05; **p<0.01; Figure 6.3.3.1 and 6.3.3.2). Additionally, we observe a significant decrease in |G*| between young adult and CN groups in WB (12.5%*), GM (11.6%*), WM (16.8%*), TL (11.4%**) and HC (20.6%**) simply due to the effect of aging (*p<0.05; **p<0.01; Figure 6.2.3.1).

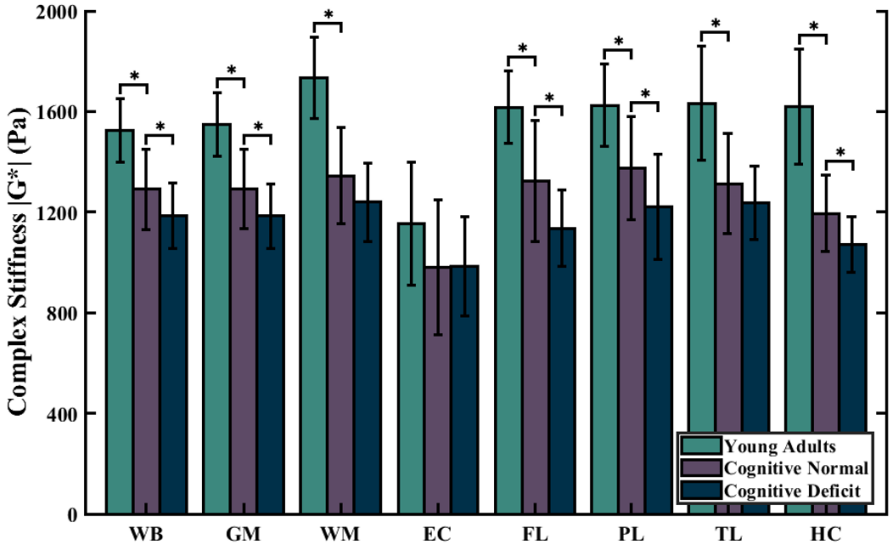

Figure 6.3.3.1. *Regional average |G*| in the whole brain (WB), gray matter (GM), white matter (WM), entorhinal cortex (EC), frontal lobe (FL), parietal lobe (PL, temporal lobe (TL), and hippocampus (HC) for the cohorts of young adults, older adults with cognitive deficits, and older adults with normal cognition. There was a significant difference in every brain region between young adults and adults with cognitive deficits, and significant differences between young adults and older adults, and between older adults and adults with cognitive deficits is indicated by *p<0.05.*

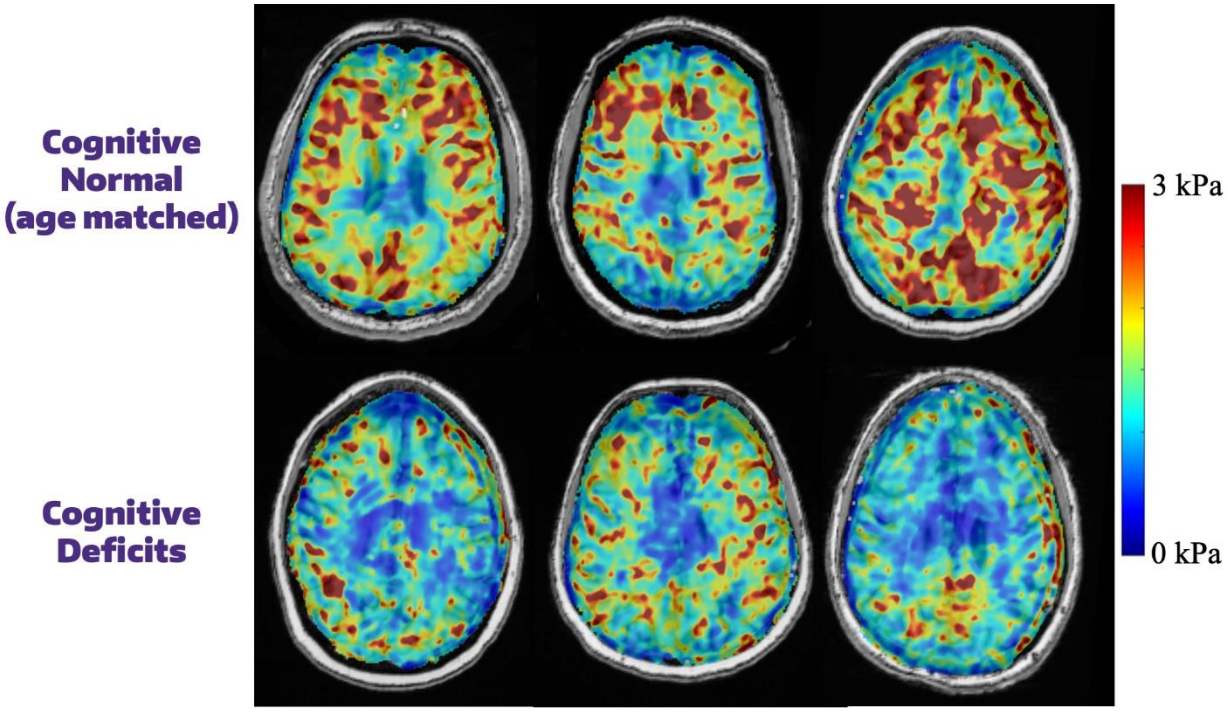

Figure 6.3.3.2. *Example elastograms in a single slice per three age and sex-matched subjects with normal cognition (top) and three adults with cognitive deficits (bottom)*

6.3.4. Multimodal Results

We found significant differences (one-tailed, unequal variance t-test, $p<0.05$) between the CN and AD/MCI groups in SUVR of all brain regions investigated. A significant negative correlation was found between average SUVR and |G*| in the cingulate and parietal cortical regions in the Aβ-positive subjects, with a trending correlation in the frontal cortex (Fig 6.3.4.1.A). We also found a significant positive correlation between SUVR and MD, and a negative correlation between |G*| and MD in the temporal cortex (Fig 6.3.4.1.B). Essentially, in the temporal cortex, the lower the diffusivity, the higher the stiffness of the tissue, and the less amyloid that was deposited. There was a significant negative correlation between SUVR and PACC, and positive correlation between |G*| and PACC, in all regions.

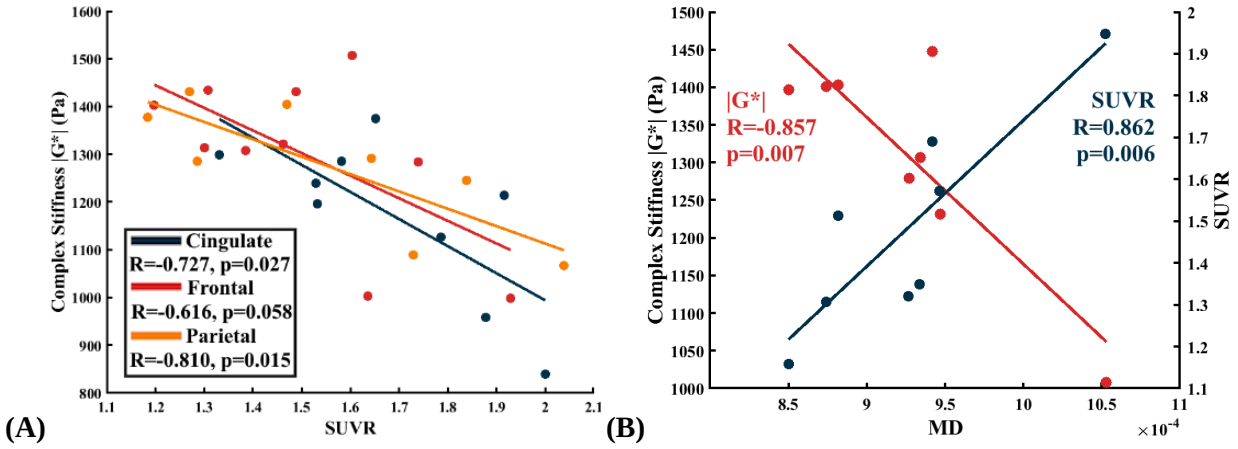

Figure 6.3.4.1. *(A) Linear correlations between |G*| and SUVR in three cortical brain regions, and (B) The linear correlations between |G*| and MD, and SUVR and MD in the temporal cortex.*

From the Shapley Regressions (Fig 6.3.4.2. A,B), in the cingulate cortex, frontal cortex, and early aggregate cortical regions, PACC was the strongest predictor of |G*|. In the parietal and temporal cortexes, MD was the strongest predictor of |G*|. To only look at imaging metrics, so excluding PACC, SUVR was the best predictor of |G*| in the cingulate cortex and early aggregate region, while MD was the best predictor of |G*| in the frontal cortex as well. PACC was also the strongest predictor of SUVR in all regions apart from the temporal cortex, where MD was the best predictor of SUVR. Once again, excluding PACC, |G*| was the best predictor of SUVR in all brain regions tested, apart from the temporal lobe, where MD was the better predictor.

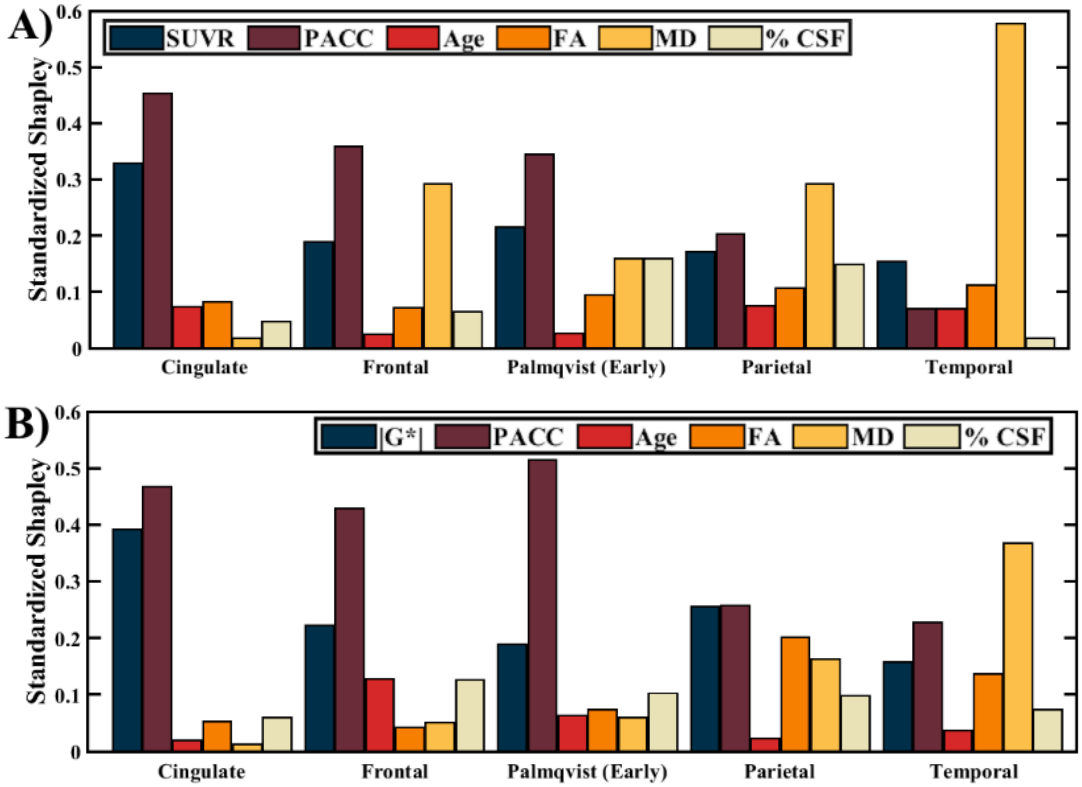

Figure 6.3.4.2. Results of the Shapley Regressions, *calculating the importance of* ***(A)*** *SUVR, Age, FA, RD, % CSF, and PACC in the results of MRE, and* ***(B)*** *the importance of Age, FA, RD, % CFS, and |G*| from MRE in the results of SUVR in multiple brain regions.*

6.2.5. Discussion

The negative correlation between |G*| and SUVR in brain regions initially impacted in MCI/AD progression is consistent with a previous investigation, supporting the hypothesis that tissue degeneration caused by Aβ accumulation results in tissue softening. The Shapley regression analyses demonstrated that SUVR and |G*| were the most important imaging covariates in their corresponding multi-regression analyses for multiple brain regions, which is promising for finding correlates of PET through MRE. This has an interesting clinical applicability, with the implication being that MRE may be used as a biomarker for amyloid deposition in the regions that |G*| was the best predictor of amyloid deposition. Given more evidence, patients may be able to undergo MRE instead of PET, so this would require less ionizing radiation for diagnosis. Additionally, because MRE does not involve any radiation or tracer use, patients would be able to undergo MRE more frequently than they would PET to better track disease progression.

Furthermore, subjects with liver and kidney injuries who cannot undergo PET scans for tracer clearance reasons (the reason why not every subject in this Chapter could have both PET and MRI scans) could undergo MRE instead.

MD being the best predictor of SUVR and G* in the temporal and parietal cortexes is consistent with previous investigations of neurodegenerative and age-related brain changes in gray matter. Specifically, correlations between SUVR or |G*| and MD, but not SUVR and |G*| in the temporal cortex may be indicative of cascades which contribute to Aβ deposition, microstructural damage, and tissue softening and degradation. The first area od degeneration and amyloid desposition in the brain is in the temporal cortex, which is where we observed the only significant Pearson correlation of MD with stiffness or amyloid deposition, so it would follow that change sin diffusion may happen later in the pathological cascade than change sin stiffness or amyloid load. Additionally, similar correlation coefficients between PACC and |G*|, and PACC and SUVR in all brain regions has interesting implications about use of MRE and DTI instead of PET for diagnosing amyloidosis with cognitive impairment.

In our investigation, we did not find any effect of volumetric changes on PACC or any imaging metric, which is why volumetric analysis was not included in the Pearson correlation plots or Shapley regressions. Since volumetric changes and cortical thinning typically occur later in AD progression[146] and the majority of our subjects are in early stages or MCI and AD, this is fairly unsurprising. Furthermore, any minor volumetric changes should not have impacted the other imaging metrics, as we used patient-specific parcellation through Freesurfer, and not coregistration with a standardized atlas. We also do not see any contribution of FA to our analysis. FA describes tractography alignment and anisotropy in white matter which cannot be measured in the cortical regions we investigated. Additionally, we saw no contribution of age, although this may be sample bias, as our patient with the most severe presentation of AD was also our youngest patient. Finally, we do not observe a large effect of CSF percentage (from our Shapley regression analysis) which was an initial partial volume concern for MRE. Due to CSF having effectively zero stiffness

as a liquid, we were initially concerned about a large volume of CSF in the parcellation volume deflating the apparent stiffness. This, however, had no effect.

Overall, we can hypothesize that decreasing stiffness in the human brain is accelerated with MCI and AD as compared to normal healthy aging. We can also hypothesize that this softening doesn't just happen globally, but more so, or early in brain regions that are associated with AD progression and memory or are functionally connected to those that are associated with memory. Additionally, amyloid deposition is predicted by this progressive softening. We can also hypothesize that changes in stiffness in cortical regions of the brain follow the same patterns of amyloid accumulation and degeneration- starting in the temporal cortex before progressing to the parietal and frontal cortexes. We can also hypothesize that increased water diffusivity occurs later in the pathway than initial softening and amyloid accumulation, as this correlation and predictive associated only happens in gray matter regions that are first affected by AD.

As for the directionality of the stiffness and amyloid cascade, it is difficult to determine from our current results whether increased amyloid plaques in a brain region causes degradation and therefore decreases stiffness, or if stiffness is decreased sue to a different mechanisms and amyloid plaques 'stick' to and are more easily embedded in the already softened tissue. Based on the results from our Shapley analysis, where stiffness was a better predictor of amyloid deposition than amyloid deposition was a predictor of stiffness, we can speculate that local softening occurs first. From animal studies investigating the microstructural changes in brain tissue due to AD progression, initial stiffness changes likely occur due to demyelination and/or changes in cell density, but not necessarily extracellular matrix degradation at first, as that happens later in the AD pathological cascade[171,172]. Plaques of amyloid then may be able to accumulate in these soft regions, which then causes more degradation and softening over time, which could cause even more amyloid to accumulate. This is supported by a recent mouse model study where myelin dysfunction was found to drive amyloid accumulation[173,174]. Some literature evidence against this hypothesis, however, is from an human brain MRE study from 2016 which found no difference in stiffness between people who were cognitively normal and amyloid negative, and cognitively normal individuals

with amyloidosis. This study, however, only looked at global brain tissue and whole lobe volume instead of just cortical regions[10].

One limitation of our study is that a more robust MRE inversion algorithm, like nonlinear inversion, would benefit the high-resolution allowed by 7T, resulting in even more detail. This study is limited by a small sample size due to some individuals not being cleared for PET tracer use and others not meeting 7T safety criteria, limiting statistical power, so future studies should look to include larger cohort of subjects diagnosed with MCI/AD. In addition, the subjects here have undergone tau PET, which has yet to be analyzed, and many have had genetic sequencing for the APOE ε4 status. Both of these additional pieces of information could shed light on further cascades and genetic predisposition to pathologic changes. Despite these challenges, our multi-modal biomechanical imaging and analysis framework has promise to determine relationships between a multitude of MRI and PET measures for AD and MCI subjects, providing a physical understanding between tissue mechanics and AD pathophysiology.

7. Future Outlooks

In this work, we have developed a 7T MRE framework, validated said framework, and applied that framework to investigate the clinical problem of Mild Cognitive Impairment and Alzheimer's disease. While significant progress was made in developing, validating, and applying 7T MRE, there is still much more work to be done in the future. For example, more work may be performed in the future to improve the 7T MRE sequence. We currently use an interleaved acquisition style, which results in a striping artifact in the z-direction during random subject motion, as the reference phase is slightly altered in the second set of slices post-motion. This results in an artificially short-wavelength and therefore an inaccurate mechanical stiffness reconstruction during nonlinear inversion. While we currently combat this through EDDY motion correction and low pass Butterworth filtering, by implementing a different readout scheme (like, for example, spiral readout) we remove the need for this extra correction and filtering that may decrease the effective resolution in the z-direction. The switch to a spiral readout, such as the type that Dr. Curtis Johnson's research group developed would result in not only a shorter echo time, thereby resulting in a TE closer to the T2 value of brain tissue at 7T, but it would also allow for high resolution acquisition, as echo time is no longer dependent on resolution[17]. This would also, however, require us to switch to a multi-shot acquisition scheme because a single-shot approach, like what is used currently, would lead to long readout times in high-resolution acquisitions and distortions due to inhomogeneities in the static magnetic field (also exacerbated at 7T). B1 and B0 inhomogeneities have also been addressed in other protocols with the addition of field mapping, so it may. Be beneficial to investigate this in the future. Another potential method for an altered encoding scheme would be to employ adiabatic pulses, as the 180° RF pulses used for refocusing a spin echo are particularly susceptible to B1 inhomogeneity[52]. Adiabatic RF pulses are highly effective solutions to perform refocusing in a B1-immune manner[52].

Now to discuss post-processing methods. As discussed in both Chapters 5 and 6, the 7T imaging protocol performed on our subjects not only included MRE, but also T1-weighted structural images and DTI. An additional mechanical modeling technique that we could employ in the future is anisotropic viscoelastic inversion by implementing DTI tractography in the nonlinear inversion. Property and fiber

direction heterogeneity can be incorporated into the model, as stiffness along these tracts is likely higher than in transverse directions, and accordingly, violates isotropic assumptions and causes wavefield-dependent artifacts when isotropic MRE is applied to anisotropic tissue[175]. The young healthy subjects scanned during Chapters 4 and 5 have also undergone full-brain CINE MRI[176], which measures intrinsic brain motion that results from blood flow throughout the heartbeat cycle. By using this extremely low-frequency motion (~1-2 Hz resting heart rate) in conjunction with the higher frequency motion measured during the 50 Hz MRE, we can perform poroviscoelastic inversion. Poroelastic effects are more important at low frequencies of intrinsic actuation, whereas model choice is less important at higher frequencies, so a simpler viscoelastic model can be used. Poroelastic inversion at low frequency has the advantage of providing a unique solution as the fluid–solid interaction forces can be balanced against elastic stresses when inertial forces are small[177].

As for the application of all of these methods, we can also use the data collected in Chapters 5 and 6 to investigate the changes in brain mechanics due to healthy aging. Both of our cohorts have undergone 50 Hz 7T MRE at 1.1 mm isotropic resolution and 7T DTI at matched resolution, so we could not only look at the change in MRE metrics or DTI metrics due to healthy aging separately, but we could also look at how the combination of these metrics change due to healthy aging as well. Additionally, the results that have not yet been processed with nonlinear inversion should be re-processed with this inversion scheme. The subjects from Chapter 6 who underwent a PET scanning session, in addition to the amyloid PET discussed, also underwent Tau and dopamine PET, so those could also be analyzed as covariates in the correlations and Shapley Regressions. All of the subjects from Chapter 6, as part of the 7T scanning protocol also underwent a T2 TSE structural scan and an SWI scan, so we could also look at the presence and number of perivascular spaces from the T2 scan and differences in susceptibility from the SWI scan as additional covariates. Because our sample size is very limited, Aim 3/Chapter 6 would benefit greatly from a larger cohort of subjects. While there were more MCI and AD subjects referred to us from the study that performed the PET and cognitive testing, many of these subjects did not pass the rigorous safety screening that is

required for a 7T MRI scan. Due to the PET scans being performed on a simultaneous 3T PET-MR scanner, we could, instead, scan these individuals on a 3T scanner using a 3T MRE sequence with k-space undersamping to achieve a resolution close to what is possible at 7T.

Despite the promising results from Chapter 6 that hint at the potential cascades of microstructural damage and neurodegeneration during the course of MCI and AD, more information is needed to draw any conclusions about the causality flow of the cascade. Future longitudinal studies using the designed framework or preclinical studies on animal models with a framework that mimics the one used here could provide more context. If a preclinical study was performed, the addition of immunofluorescent staining would also provide more context regarding cellular level contributors to the tissue-level effects we see with imaging, such as extracellular matrix integrity and cellular density. As for a future longitudinal study, we could observe how different imaging modalities' metrics change throughout the course of neurodegeneration and disease progression in relation to each other and to the subjects cognitive function. Additionally, if any of these subjects were to start taking amyloid clearing pharmaceuticals, we could observe how the progression of these changes in properties are different from those of subjects who are not taking the pharmaceutical treatments. We could also closely observe for any parameters that could precede side-effects from taking these amyloid clearing treatments, for example, amyloid-related imaging abnormality (ARIA), which is a new signs and symptoms including headache, worsening confusion, dizziness, visual disturbances, nausea, and seizures[178].

8. References

1. Muthupillai, R. *et al.* Magnetic resonance imaging of transverse acoustic strain waves. *Magn Reson Med* **36**, 266–274 (1996).
2. Clayton, E. H., Genin, G. M. & Bayly, P. V. Transmission, attenuation and reflection of shear waves in the human brain. *J R Soc Interface* **9**, 2899–2910 (2012).
3. Tse, Z. T. H. *et al.* Magnetic resonance elastography hardware design: A survey. *Proc Inst Mech Eng H* **223**, 497–514 (2009).
4. Guo, J. *et al.* Towards an Elastographic Atlas of Brain Anatomy. *PLoS One* **8**, (2013).
5. Johnson, C. L. *et al.* MR elastography of intercranial tumors: initial experience with high-resolution imaging and nonlinear inversion. in *ISMRM 2016* (2016). doi:10.1007/s00062-014-0311-9.
6. Zhang, J., Green, M. A., Sinkus, R. & Bilston, L. E. Viscoelastic properties of human cerebellum using magnetic resonance elastography. *J Biomech* **44**, 1909–1913 (2011).
7. Kurt, M. *et al.* Optimization of a Multifrequency Magnetic Resonance Elastography Protocol for the Human Brain. *Journal of Neuroimaging* **29**, 440–446 (2019).
8. Hiscox, L. V. *et al.* Standard-space atlas of the viscoelastic properties of the human brain. *Hum Brain Mapp* **41**, 5282–5300 (2020).
9. Huston, J. *et al.* Magnetic resonance elastography of frontotemporal dementia. *Journal of Magnetic Resonance Imaging* **43**, 474–478 (2016).
10. Murphy, M. C. *et al.* Regional brain stiffness changes across the Alzheimer's disease spectrum. *Neuroimage Clin* **10**, 283–290 (2016).
11. Streitberger, K. J. *et al.* In vivo viscoelastic properties of the brain in normal pressure hydrocephalus. *NMR Biomed* **24**, 385–392 (2011).
12. Huston, J. *et al.* Magnetic resonance elastography demonstrates increased brain stiffness in normal pressure hydrocephalus. *Fluids Barriers CNS* **12**, O38 (2015).
13. Perry, A. *et al.* Clinical Correlation of Abnormal Findings on Magnetic Resonance Elastography in Idiopathic Normal Pressure Hydrocephalus. *World Neurosurg* **99**, 695–700 (2017).
14. Pattison, A. J., Lollis, S. S., Perrinez, P. R., Weaver, J. B. & Paulsen, K. D. MR elastography of hydrocephalus. in *Proceedings of SPIE - The International Society for Optical Engineering* vol. 7262 72620A0-8 (2009).
15. McIlvain, G., Schwarb, H., Cohen, N. J., Telzer, E. H. & Johnson, C. L. Mechanical properties of the in vivo adolescent human brain. *Dev Cogn Neurosci* **34**, 27–33 (2018).
16. Sack, I. *et al.* The impact of aging and gender on brain viscoelasticity. *Neuroimage* **46**, 652–657 (2009).
17. Hiscox, L. V. *et al.* High-reolution magnetic resonance elastography reveals differences in subcortical gray matter viscoelasticity between young and healthy older adults. *Neurobiol Aging* **65**, 158–167 (2018).
18. Sack, I., Streitberger, K. J., Krefting, D., Paul, F. & Braun, J. The influence of physiological aging and atrophy on brain viscoelastic properties in humans. *PLoS One* **6**, (2011).
19. Fehlner, A. *et al.* The viscoelastic response of the human brain to functional activation detected by magnetic resonance elastography. in *Proceedings of the 22nd Annul Meeting of ISMRM, Milan* (2014).

20. Wuerfel, J. *et al.* MR-elastography reveals degradation of tissue integrity in multiple sclerosis. *Neuroimage* **49**, 2520–2525 (2010).

21. Johnson, C. L. *et al.* Multiple sclerosis lesions are softer than surrounding white matter : An MR elastography study. in *ISMRM 2017 Conference Proceedings* (2017).

22. Streitberger, K. J. *et al.* Brain viscoelasticity alteration in chronic-progressive multiple sclerosis. *PLoS One* **7**, (2012).

23. Lipp, A. *et al.* Cerebral magnetic resonance elastography in supranuclear palsy and idiopathic Parkinson's disease. *Neuroimage Clin* **3**, 381–387 (2013).

24. Lipp, A. *et al.* Progressive supranuclear palsy and idiopathic Parkinson's disease are associated with local reduction of in vivo brain viscoelasticity. *Eur Radiol* **28**, 3347–3354 (2018).

25. Murphy, M. C. *et al.* Decreased brain stiffness in alzheimer's disease determined by magnetic resonance elastography. *Journal of Magnetic Resonance Imaging* **34**, 494–498 (2011).

26. Hiscox, L. V *et al.* Mechanical property alterations across the cerebral cortex due to Alzheimer's disease. *Brain Commun* **2**, (2019).

27. ElSheikh, M. M. *et al.* MR elastography demonstrates unique regional brain stiffness patterns in dementias. *AJR Am J Roentgenol* **209**, 403–408 (2017).

28. Gerischer, L. M. *et al.* High resolution MR elastography of the hippocampus as a novel biomarker for Alzheimer's disease? in *Clinical Neurophysiology* vol. 127 e216–e217 (2016).

29. Braun, J. *et al.* High-resolution mechanical imaging of the human brain by three-dimensional multifrequency magnetic resonance elastography at 7T. *Neuroimage* **90**, 308–314 (2014).

30. Chaze, C. A. *et al.* Altered brain tissue viscoelasticity in pediatric cerebral palsy measured by magnetic resonance elastography. *Neuroimage Clin* **22**, (2019).

31. Triolo, E. R. *et al.* Design, Construction, and Implementation of a Magnetic Resonance Elastography Actuator for Research Purposes. *Curr Protoc* **2**, 1–26 (2022).

32. Murphy, M. C. *et al.* Measuring the characteristic topography of brain stiffness with magnetic resonance elastography. *PLoS One* **8**, 1–14 (2013).

33. Veraart, J. *et al.* Denoising of diffusion MRI using random matrix theory. *Neuroimage* **142**, 394–406 (2016).

34. Barnhill, E. *et al.* Impact of Field Strength and Image Resolution on MRE Stiffness Estimation. in *Proc 24th Annual Meeting ISMRM* (2016).

35. Marshall, H. *et al.* Magnetic resonance elastography (MRE) reproducibility study in the same participants at field strengths of 1.5, 3, and 7 Tesla. in *First International MRE Workshop in Berlin* 25 (2017).

36. Triolo, E. R. *et al.* Validation and testing of 7T MR elastography sequence and stiffness reconstruction. in *BMES 2021* (2021).

37. Triolo, E. *et al.* Development and validation of an ultra-high field compatible MR elastography actuator. in *Summer Biomechanics, Bioengineering and Biotransport Conference* SB3C2021-325 (2021).

38. Papazoglou, S., Hamhaber, U., Braun, J. & Sack, I. Horizontal shear wave scattering from a nonwelded interface observed by magnetic resonance elastography. *Phys Med Biol* **52**, 675–684 (2007).

39. Latta, P. *et al.* Convertible pneumatic actuator for magnetic resonance elastography of the brain. *Magn Reson Imaging* **29**, 147–152 (2011).

40. Ansorge, R. & Graves, M. *The Physics and Mathematics of MRI*. (Morgan & Claypool Publishers, 2016). doi:10.1088/978-1-6817-4068-3.

41. Hirsch, S., Braun, J. & Sack, I. *Magnetic Resonance Elastography: Physical Background and Medical Applications*. *Wiley* (2017). doi:10.1038/nm0596-601.

42. Weishaupt, D., Kochli, V. D. & Marincek, B. *How Does MRI Work? An Introduction to the Physics and Function of Magnetic Resonance Imaging*. (Springer, 2008).

43. Sack, I., Beierbach, B., Hamhaber, U., Klatt, D. & Braun, J. Non-invasive measurement of brain viscoelasticity using magnetic resonance elastography. *NMR Biomed* **21**, 265–271 (2008).

44. Muthupillai, R. *et al.* Magnetic resonance elastography by direct visualization of propagating acoustic strain waves. *Science (1979)* **269**, 1854–1857 (1995).

45. McGarry, M. D. J. Improvement and Evaluation of Nonlinear Inversion MR Elastography. (2013).

46. McGarry, M. D. J. *et al.* An octahedral shear strain-based measure of SNR for 3D MR elastography. *Phys Med Biol* **56**, (2011).

47. Vaughan, J. T. *et al.* 7T vs. 4T: RF power, homogeneity, and signal-to-noise comparison in head images. *Magn Reson Med* **46**, 24–30 (2001).

48. Duyn, J. H. The future of ultra-high field MRI and fMRI for study of the human brain. *Neuroimage* **62**, 1241–1248 (2012).

49. Uğurbil, K. *et al.* Ultrahigh field magnetic resonance imaging and spectroscopy. *Magn Reson Imaging* **21**, 1263–1281 (2003).

50. Peters, A. M. *et al.* T2* measurements in human brain at 1.5, 3 and 7 T. *Magn Reson Imaging* **25**, 748–753 (2007).

51. Balchandani, P. & Naidich, T. P. Ultra-high-field MR neuroimaging. *American Journal of Neuroradiology* **36**, 1204–1215 (2015).

52. Balchandani, P., Khalighi, M. M., Glover, G., Pauly, J. & Spielman, D. Self-refocused adiabatic pulse for spin echo imaging at 7 T. *Magn Reson Med* **67**, 1077–1085 (2012).

53. Feng, Y. *et al.* A multi-purpose electromagnetic actuator for magnetic resonance elastography. *Magn Reson Imaging* **51**, 29–34 (2018).

54. Freimann, F. B. *et al.* Alteration of brain viscoelasticity after shunt treatment in normal pressure hydrocephalus. *Neuroradiology* **54**, 189–196 (2012).

55. Asbach, P. *et al.* Assessment of liver viscoelasticity using multifrequency MR elastography. *Magn Reson Med* **60**, 373–379 (2008).

56. Yin, M., Rouviere, O., Glaser, K. J. & Ehman, R. L. Diffraction-biased shear wave fields generated with longitudinal magnetic resonance elastography drivers. *Magn Reson Imaging* **26**, 770–780 (2008).

57. Chang, W. *et al.* Liver fibrosis staging with MR elastography: Comparison of diagnostic performance between patients with chronic hepatitis B and those with other etiologic causes. *Radiology* **280**, 88–97 (2016).

58. Gruwel, M. L. H., Latta, P., Matwiy, B. & Tomanek, B. Characterization of food stuffs using Magnetic Resonance Elastography. *Food Research International* **43**, 2087–2092 (2010).

59. MR Elastography | Resoundant Inc. https://www.resoundant.com/.

60. Zheng, Y. *et al.* Magnetic resonance elastography with twin pneumatic drivers for wave compensation. in *Annual International Conference of the IEEE Engineering in Medicine and Biology - Proceedings* vol. 29 2611–2613 (2007).

61. Badachhape, A. A., Okamoto, R. J., Johnson, C. L. & Bayly, P. V. Relationships between scalp, brain, and skull motion estimated using magnetic resonance elastography. *J Biomech* **73**, 40–49 (2018).

62. Venkatesh, S. K., Yin, M. & Ehman, R. L. Magnetic Resonance Elastography of Liver: Technique, Analysis and Clinical Applications. *J Magn Reson Imaging* **37**, 544–555 (2013).

63. Neumann, W. *et al.* Coupled actuators with a mechanically synchronized phase during MR elastography: A phantom feasibility study. *Concepts Magn Reson Part B Magn Reson Eng* **48**, 1–9 (2018).

64. Uffmann, K., Abicht, C., Quick, H. H., Ulbrich, H. & Ladd, M. E. Characterization of an Electromagnetic Actuator for MR Elastography. in *Proc. Intl. Soc. Mag. Reson. Med* vol. 9 1635 (2001).

65. Sack, I., Bernarding, J. & Braun, J. Analysis of wave patterns in MR elastography of skeletal muscle using coupled harmonic oscillator simulations. *Magn Reson Imaging* **20**, 95–104 (2002).

66. Liu, G. R. *et al.* Brain magnetic resonance elastography on healthy volunteers: A safety study. *Acta radiol* **50**, 423–429 (2009).

67. Hamhaber, U., Grieshaber, F. A., Nagel, J. H. & Klose, U. Comparison of quantitative shear wave MR-elastography with mechanical compression tests. *Magn Reson Med* **49**, 71–77 (2003).

68. Hamhaber, U. *et al.* In vivo magnetic resonance elastography of human brain at 7 T and 1.5 T. *Journal of Magnetic Resonance Imaging* **32**, 577–583 (2010).

69. Suga, M. *et al.* Measurement of In Vivo Local Shear Modulus Using MR Elastography Multiple-Phase Patchwork Offsets. *IEEE Trans Biomed Eng* **50**, 908–915 (2003).

70. Neumann, W. *et al.* A novel 3D printed mechanical actuator using centrifugal force for magnetic resonance elastography: Initial results in an anthropomorphic prostate phantom. *PLoS One* **13**, 1–14 (2018).

71. Numano, T. *et al.* Magnetic resonance elastography using an air ball-actuator. *Magn Reson Imaging* **31**, 939–946 (2013).

72. Runge, J. H. *et al.* A novel magnetic resonance elastography transducer concept based on a rotational eccentric mass: Preliminary experiences with the gravitational transducer. *Phys Med Biol* **64**, (2019).

73. Gordon-Wylie, S. W. *et al.* MR elastography at 1 Hz of gelatin phantoms using 3D or 4D acquisition. *Journal of Magnetic Resonance* **296**, 112–120 (2018).

74. Uffmann, K., Abicht, C., Grote, W., Quick, H. H. & Ladd, M. E. Design of an MR-compatible piezoelectric actuator for MR elastography. *Concepts Magn Reson Part B Magn Reson Eng* **15**, 239–254 (2002).

75. Namani, R., Wood, M. D., Sakiyama, S. E. & Bayly, P. V. Anisotropic mechanical properties of magnetically aligned fibrin gels measured by magnetic resonance elastography. *J Biomech* **42**, 2047–2053 (2009).

76. Yin, Z., Kearney, S. P., Magin, R. L. & Klatt, D. Concurrent 3D acquisition of diffusion tensor imaging and magnetic resonance elastography displacement data (DTI-MRE): Theory and in vivo application. *Magn Reson Med* **77**, 273–284 (2017).

77. Rossman, P., Glaser, K., Felmlee, J. & Ehman, R. Piezoelectric Bending Elements for use as Motion Actuators in MR Elastography. *Proc. Intl. Soc. Mag. Reson. Med* vol. 11 1075 (2003).

78. Brauck, K., Galbán, C. J., Maderwald, S., Herrmann, B. L. & Ladd, M. E. Changes in calf muscle elasticity in hypogonadal males before and after testosterone substitution as monitored by magnetic resonance elastography. *Eur J Endocrinol* **156**, 673–678 (2007).

79. Ozkaya, E. *et al.* Brain-mimicking phantom for biomechanical validation of motion sensitive MR imaging techniques. *J Mech Behav Biomed Mater* **122**, 104680 (2021).

80. Meinhold, W., Ozkaya, E., Ueda, J. & Kurt, M. Tuneable resonance actuators for magnetic resonance elastography. in *Frontiers in Biomedical Devices, BIOMED - 2019 Design of Medical Devices Conference, DMD 2019* 1–5 (2019). doi:10.1115/DMD2019-3313.

81. Lee, Y. C., Zotti, M. G. T. & Osti, O. L. Operative management of lumbar degenerative disc disease. *Asian Spine Journal* vol. 10 801–819 Preprint at https://doi.org/10.4184/asj.2016.10.4.801 (2016).

82. van Uden, S., Silva-Correia, J., Oliveira, J. M. & Reis, R. L. Current strategies for treatment of intervertebral disc degeneration: Substitution and regeneration possibilities. *Biomaterials Research* vol. 21 Preprint at https://doi.org/10.1186/s40824-017-0106-6 (2017).

83. Farshad-Amacker, N. A., Farshad, M., Winklehner, A. & Andreisek, G. MR imaging of degenerative disc disease. *European Journal of Radiology* vol. 84 1768–1776 Preprint at https://doi.org/10.1016/j.ejrad.2015.04.002 (2015).

84. Boden, S. D., Davis, D. O., Dina, T. S., Patronas, N. J. & Wiesel, S. W. Abnormal magnetic-resonance scans of the lumbar spine in asymptomatic subjects. A prospective investigation. **72**, 403–408 (1990).

85. Pfirrmann, C. W. A., Metzdorf, A., Zanetti, M., Hodler, J. & Boos, N. Magnetic Resonance Classification of Lumbar Intervertebral Disc Degeneration. *Spine (Phila Pa 1976)* **26**, 1873–1878 (2001).

86. Zhou, Y. & Abdi, S. *Diagnosis and Minimally Invasive Treatment of Lumbar Discogenic Pain-A Review of the Literature*. http://journals.lww.com/clinicalpain (2006).

87. Ozkaya, E. *et al.* Viscoelasticity of children and adolescent brains through MR elastography. *J Mech Behav Biomed Mater* **115**, 104229 (2021).

88. Meinhold, W. *et al.* Towards Image Guided Magnetic Resonance Elastography via Active Driver Positioning Robot. *IEEE Trans Biomed Eng* **69**, 3345–3355 (2022).

89. Johnson, C. L. *et al.* Magnetic resonance elastography of the brain using multi-shot spiral readouts with self-navigated motion correction. *Magn Reson Med* **70**, 404–412 (2013).

90. Oliphant, T. E., Manduca, A., Ehman, R. L. & Greenleaf, J. F. Complex-valued stiffness reconstruction for magnetic resonance elastography by algebraic inversion of the differential equation. *Magn Reson Med* **45**, 299–310 (2001).

91. McGarry, M. D. J. *et al.* An octahedral shear strain-based measure of SNR for 3D MR elastography. *Phys Med Biol* **56**, (2011).

92. Streitberger, K. J. *et al.* In vivo multifrequency magnetic resonance elastography of the human intervertebral disk. *Magn Reson Med* **74**, 1380–1387 (2015).

93. Fehlner, A. *et al.* Increasing the spatial resolution and sensitivity of magnetic resonance elastography by correcting for subject motion and susceptibility-induced image distortions. *Journal of Magnetic Resonance Imaging* **46**, 134–141 (2017).

94. Barnhill, E., Selesnick, I., Sack, I., Braun, J. & Roberts, N. Impact of Wavelet Thresholding Methods on MR Elastography Human Brain Stiffness Results. in (2014).

95. Mcilvain, G., Hannum, A. J., Christodoulou, A. G., Mcgarry, M. D. J. & Johnson, C. L. Low-Rank Denoising of Magnetic Resonance Elastography Images. *ISMRM Conference Proceedings*.

96. Solamen, L. M., Gordon-Wylie, S. W., McGarry, M. D., Weaver, J. B. & Paulsen, K. D. Phantom evaluations of low frequency MR elastography. *Phys Med Biol* **64**, 0–14 (2019).

97. Barnhill, E. *et al.* Investigation Of The Relationship Between Feature Detail And Stiffness Estimate In Magnetic Resonance Elastography (MRE) Elastograms. *Proc 24th Annual Meeting ISMRM* 22–24 (2016).

98. Manduca, A., Lake, D. S. & Ehman, R. L. Spatio-temporal Directional Filtering for Improved Inversion of MR Elastography Images. in *MICCAI 2002, LNCS 2489* 293–299 (2002).

99. Manduca, A., Lake, D. S. & Ehman, R. L. Improved inversion of MR elastography images by spatio-temporal directional filtering. *Medical Imaging 2003: Image Processing* **5032**, 445 (2003).

100. Li, B. N. *et al.* Evaluation of robust wave image processing methods for magnetic resonance elastography. *Comput Biol Med* **54**, 100–108 (2014).

101. Karsa, A. & Shmueli, K. SEGUE: A Speedy rEgion-Growing Algorithm for Unwrapping Estimated Phase. *IEEE Trans Med Imaging* **38**, 1347–1357 (2019).

102. Johnson, C. L. *et al.* 3D multislab, multishot acquisition for fast, whole-brain MR elastography with high signal-to-noise efficiency. *Magn Reson Med* **71**, 477–485 (2014).

103. Manduca, A. *et al.* MR elastography: Principles, guidelines, and terminology. *Magnetic Resonance in Medicine* vol. 85 2377–2390 Preprint at https://doi.org/10.1002/mrm.28627 (2021).

104. Triolo, E. *et al.* Parameter Optimization for High-Resolution MR Elastography of the Human Brain at 7T. in *Proc. ISMRM-ESMRMB 31st Annual Meeting* (2022).

105. Hansen, M. S. & Sørensen, T. S. Gadgetron: An open source framework for medical image reconstruction. *Magn Reson Med* **69**, 1768–1776 (2013).

106. Penny, W., Friston, K., Ashburner, J., Kiebel, S. & Nichols, T. *Statistical Parametric Mapping: The Analysis of Functional Brain Images*. (2006).

107. McIlvain, G., McGarry, M. D. J. & Johnson, C. L. Quantitative effects of off-resonance related distortion on brain mechanical property estimation with magnetic resonance elastography. *NMR Biomed* **35**, (2022).

108. Hannum, A. J., McIlvain, G., Sowinski, D., McGarry, M. D. J. & Johnson, C. L. Correlated noise in brain magnetic resonance elastography. *Magn Reson Med* **87**, 1313–1328 (2022).

109. McIlvain, G., Cerjanic, A. M., Christodoulou, A. G., McGarry, M. D. J. & Johnson, C. L. OSCILLATE: A low-rank approach for accelerated magnetic resonance elastography. *Magn Reson Med* **88**, 1659–1672 (2022).

110. Mcilvain, G., Hannum, A. J., Christodoulou, A. G., Mcgarry, M. D. J. & Johnson, C. L. Low-Rank Denoising of Magnetic Resonance Elastography Images. *ISMRM Conference Proceedings* (2019).

111. Barnhill, E. *et al.* Investigation Of The Relationship Between Feature Detail And Stiffness Estimate In Magnetic Resonance Elastography (MRE) Elastograms. *Proc 24th Annual Meeting ISMRM* 22–24 (2016).

112. Veraart, J. *et al.* Denoising of diffusion MRI using random matrix theory. *Neuroimage* **142**, 394–406 (2016).

113. Veraart, J., Fieremans, E. & Novikov, D. S. Diffusion MRI noise mapping using random matrix theory. *Magn Reson Med* **76**, 1582–1593 (2016).

114. Xu, L., Lin, Y., Xi, Z. N., Shen, H. & Gao, P. Y. Magnetic resonance elastography of the human brain: A preliminary study. *Acta radiol* **48**, 112–115 (2007).

115. Hamhaber, U. *et al.* Three-dimensional analysis of shear wave propagation observed by in vivo magnetic resonance elastography of the brain. *Acta Biomater* **3**, 127–137 (2007).

116. Weickenmeier, J. *et al.* Magnetic resonance elastography of the brain: A comparison between pigs and humans. *J Mech Behav Biomed Mater* **77**, 702–710 (2018).

117. Kruse, S. A. *et al.* Magnetic resonance elastography of the brain. *Neuroimage* **39**, 231–237 (2008).

118. Fehlner, A. *et al.* Higher-resolution MR elastography reveals early mechanical signatures of neuroinflammation in patients with clinically isolated syndrome. *Journal of Magnetic Resonance Imaging* **44**, 51–58 (2016).

119. McGarry, M. D. J. *et al.* Multiresolution MR elastography using nonlinear inversion. *Med Phys* **39**, 6388–6396 (2012).

120. McGarry, M. *et al.* A heterogenous, time harmonic, nearly incompressible transverse isotropic finite element brain simulation platform for MR elastography. *Phys Med Biol* **66**, (2021).

121. Johnson, C. L. *et al.* Local mechanical properties of white matter structures in the human brain. *Neuroimage* 145–152 (2013) doi:10.1016/j.neuroimage.2013.04.089.Local.

122. Inati, S. J., Hansen, M. S. & Kellman, P. A Fast Optimal Method for Coil Sensitivity Estimation and Adaptive Coil Combination for Complex Images. in *Proc. Intl. Soc. Meg. Reson. Med.* 4407 (2014).

123. Inati, S. J., Hansen, M. S. & Kellman, P. A Solution to the Phase Problem in Adaptive Coil Combination. in *Proc. Intl. Soc. Mag. Reson. Med.* vol. 16 2672 (2013).

124. Andersson, J. L. R. & Sotiropoulos, S. N. An integrated approach to correction for off-resonance effects and subject movement in diffusion MR imaging. *Neuroimage* **125**, 1063–1078 (2016).

125. Mohammed, S., Kozlowski, P. & Salcudean, S. Phase-regularized and displacement-regularized compressed sensing for fast magnetic resonance elastography. *NMR Biomed* **36**, (2023).

126. Shan, X., Yang, J., Xu, P., Hu, L. & Ge, H. Deep neural networks for magnetic resonance elastography acceleration in thermal-ablation monitoring. *Med Phys* **49**, 1803–1813 (2022).

127. Herthum, H. *et al.* In vivo stiffness of multiple sclerosis lesions is similar to that of normal-appearing white matter. *Acta Biomater* **138**, 410–421 (2022).

128. Johnson, C. L. *et al.* Viscoelasticity of subcortical gray matter structures. *Hum Brain Mapp* **37**, 4221–4233 (2016).

129. Svensson, S. F. *et al.* Robustness of MR Elastography in the Healthy Brain: Repeatability, Reliability, and Effect of Different Reconstruction Methods. *Journal of Magnetic Resonance Imaging* **53**, 1510–1521 (2021).

130. Smith, D. R. *et al.* Anisotropic mechanical properties in the healthy human brain estimated with multi-excitation transversely isotropic MR elastography. *Brain Multiphys* **3**, (2022).

131. *QIBA Profile: Magnetic Resonance Elastography of the Liver 5 Stage 2: Consensus Profile*. (2018).

132. Ozkaya, E. *et al.* Precision and Test-Retest Repeatability of Stiffness Measurement with MR Elastography: A Multicenter Phantom Study. *Radiology* **311**, (2024).

133. Coelho, A. & Sousa, N. Magnetic resonance elastography of the ageing brain in normal and demented populations: A systematic review. *Human Brain Mapping* vol. 43 4207–4218 Preprint at https://doi.org/10.1002/hbm.25891 (2022).

134. Conroy, D. A., Spielman, A. J. & Scott, R. Q. Daily rhythm of cerebral blood flow velocity. *J Circadian Rhythms* **3**, (2005).

135. Hetzer, S. *et al.* Perfusion alters stiffness of deep gray matter. *Journal of Cerebral Blood Flow and Metabolism* **38**, 116–125 (2018).

136. Farahani, F. V. *et al.* Effects of chronic sleep restriction on the brain functional network, as revealed by graph theory. *Front Neurosci* **13**, (2019).

137. Jackson, M. L. *et al.* The effect of sleep deprivation on BOLD activity elicited by a divided attention task. *Brain Imaging Behav* **5**, 97–108 (2011).

138. Arani, A. *et al.* Acute pressure changes in the brain are correlated with MR elastography stiffness measurements: initial feasibility in an in vivo large animal model. *Magn Reson Med* **79**, 1043–1051 (2018).

139. Zhang, N., Zhang, J., Du, S. & Ma, G. Dehydration and rehydration affect brain regional density and homogeneity among young male adults, determined via magnetic resonance imaging: A pilot self-control trial. *Front Nutr* **9**, (2022).

140. Lv, H. *et al.* MR elastography frequency–dependent and independent parameters demonstrate accelerated decrease of brain stiffness in elder subjects. *Eur Radiol* **30**, 6614–6623 (2020).

141. Fischl, B., Liu, A. & Dale, A. M. *Automated Manifold Surgery: Constructing Geometrically Accurate and Topologically Correct Models of the Human Cerebral Cortex*. *IEEE TRANSACTIONS ON MEDICAL IMAGING* vol. 20 (2001).

142. Mori, S. *et al.* Stereotaxic White Matter Atlas Based on Diffusion Tensor Imaging in an ICBM Template. *Neuroimage* **40**, 570–582 (2008).

143. Hardy, J. A. & Higgins, G. A. Alzheimer's Disease: The Amyloid Hypothesis. *Science (1979)* **256**, 184–185 (1992).

144. Gunes, S., Aizawa, Y., Sugashi, T., Sugimoto, M. & Rodrigues, P. P. Biomarkers for Alzheimer's Disease in the Current State: A Narrative Review. *International Journal of Molecular Sciences* vol. 23 Preprint at https://doi.org/10.3390/ijms23094962 (2022).

145. Márquez, F. & Yassa, M. A. Neuroimaging Biomarkers for Alzheimer's Disease. *Molecular Neurodegeneration* vol. 14 Preprint at https://doi.org/10.1186/s13024-019-0325-5 (2019).

146. Lombardi, G. *et al.* Structural magnetic resonance imaging for the early diagnosis of dementia due to Alzheimer's disease in people with mild cognitive impairment. *Cochrane Database of Systematic Reviews* (2020) doi:10.1002/14651858.CD009628.pub2/full.

147. Blinkouskaya, Y. & Weickenmeier, J. Spatiotemporal Atrophy Patterns in Healthy Brain Aging and Alzheimer's Disease. in *IMECE* (2021).

148. Andersen, E. *et al.* Diagnostic biomarkers in Alzheimer's disease. *Biomark Neuropsychiatry* **5**, (2021).

149. Thal, D. R., Rüb, U., Orantes, M. & Braak, H. Phases of A-deposition in the human brain and its relevance for the development of AD. *Neurology* **58**, (2002).

150. Braak, H. & Braak, E. Neuropathological stageing of Alzheimer-related changes. *Acta Neuropathol* **82**, 239–259 (1991).

151. Bullich, S. *et al.* Early detection of amyloid load using 18F-florbetaben PET. *Alzheimers Res Ther* **13**, (2021).

152. Klunk, W. E. *et al.* The Centiloid project: Standardizing quantitative amyloid plaque estimation by PET. *Alzheimer's and Dementia* **11**, 1-15.e4 (2015).

153. Imabayashi, E. *et al.* Amyloid accumulation in the medial temporal area starts in the mild cognitive impairment stage of Alzheimer's disease in [18 F]flutemetamol positron emission tomography . *Alzheimer's & Dementia* **19**, (2023).

154. Palmqvist, S. *et al.* Earliest accumulation of β-amyloid occurs within the default-mode network and concurrently affects brain connectivity. *Nat Commun* **8**, (2017).

155. Kroth, H. *et al.* Discovery and preclinical characterization of [18F]PI-2620, a next-generation tau PET tracer for the assessment of tau pathology in Alzheimer's disease and other tauopathies. *Eur J Nucl Med Mol Imaging* **46**, 2178–2189 (2019).

156. Cho, H. *et al.* Tau PET in Alzheimer disease and mild cognitive impairment. *American Academy of Neurology* **87**, 375–383 (2016).

157. Schroeter, M. L. *et al.* Dissociation of amyloid biomarkers in PET and CSF in Alzheimer's disease: A case report. *BMC Neurol* **15**, (2015).

158. Mayo, C. D. *et al.* Relationship between DTI metrics and cognitive function in Alzheimer's disease. *Front Aging Neurosci* **11**, (2019).

159. Kantarci, K. *et al.* White-matter integrity on DTI and the pathologic staging of Alzheimer's disease. *Neurobiol Aging* **56**, 172–179 (2017).

160. Henf, J., Grothe, M. J., Brueggen, K., Teipel, S. & Dyrba, M. Mean diffusivity in cortical gray matter in Alzheimer's disease: The importance of partial volume correction. *Neuroimage Clin* **17**, 579–586 (2018).

161. Lee, P., Kim, H. R. & Jeong, Y. Detection of gray matter microstructural changes in Alzheimer's disease continuum using fiber orientation. *BMC Neurol* **20**, (2020).

162. Hiscox, L. V. *et al.* Hippocampal viscoelasticity and episodic memory performance in healthy older adults examined with magnetic resonance elastography. *Brain Imaging Behav* **14**, 175–185 (2020).

163. Palotai, M. *et al.* Magnetic resonance elastography to study the effect of amyloid plaque accumulation in a mouse model. *Journal of Neuroimaging* **32**, 617–628 (2022).

164. Maharjan, S. *et al.* Directional Filter, Local Frequency Estimate and Algebraic Inversion of Differential Equation of Psoas Major Magnetic Resonance Elastography. *Open Journal of Medical Imaging* **10**, 1–16 (2020).

165. O'Donnell, L. J. & Westin, C. F. An Introduction to Diffusion Tensor Image Analysis. *Neurosurg Clin N Am* **22**, 185–196 (2011).

166. Lee, H. Y., Park, J. H., Kim, A. R., Park, M. & Kim, T. W. Neurobehavioral recovery in patients who emerged from prolonged disorder of consciousness: A retrospective study. *BMC Neurol* **20**, (2020).

167. Pfefferbaum, A. *et al.* Accelerated aging of selective brain structures in human immunodeficiency virus infection: A controlled, longitudinal magnetic resonance imaging study. *Neurobiol Aging* **35**, 1755–1768 (2014).

168. Anderson, A. T. *et al.* Observation of direction-dependent mechanical properties in the human brain with multi-excitation MR elastography. *J Mech Behav Biomed Mater* **59**, 538–546 (2016).

169. Triolo, E. *et al.* High Resolution MR Elastography Of The Human Brain: Technical Development And Applications In Aging And Alzheimer's Disease. in *Summer Biomechanics, Bioengineering and Biotransport Conference 2023* (Vail, CO, USA, 2023).

170. Reuter, M., Schmansky, N. J., Rosas, H. D. & Fischl, B. Within-Subject Template Estimation for Unbiased Longitudinal Image Analysis. *Neuroimage* **61**, 1402–1418 (2012).

171. Hall, C. M., Moeendarbary, E. & Sheridan, G. K. Mechanobiology of the brain in ageing and Alzheimer's disease. *European Journal of Neuroscience* **53**, 3851–3878 (2021).

172. Hebisch, M. *et al.* The Impact of the Cellular Environment and Aging on Modeling Alzheimer's Disease in 3D Cell Culture Models. *Advanced Science* vol. 10 Preprint at https://doi.org/10.1002/advs.202205037 (2023).

173. Depp, C. *et al.* Myelin dysfunction drives amyloid-β deposition in models of Alzheimer's disease. *Nature* **618**, 349–357 (2023).

174. Majumdar, S. & Klatt, D. Longitudinal study of sub-regional cerebral viscoelastic properties of 5XFAD Alzheimer's disease mice using multifrequency MR elastography. *Magn Reson Med* **86**, 405–414 (2021).

175. McGarry, M. *et al.* Mapping heterogenous anisotropic tissue mechanical properties with transverse isotropic nonlinear inversion MR elastography. *Med Image Anal* **78**, (2022).

176. Terem, I. *et al.* Revealing sub-voxel motions of brain tissue using phase-based amplified MRI (aMRI). *Magn Reson Med* **80**, (2018).

177. McGarry, M. *et al.* Uniqueness of poroelastic and viscoelastic nonlinear inversion MR elastography at low frequencies. *Phys Med Biol* **64**, (2019).

178. Withington, C. G. & Turner, R. S. Amyloid-Related Imaging Abnormalities With Anti-amyloid Antibodies for the Treatment of Dementia Due to Alzheimer's Disease. *Frontiers in Neurology* vol. 13 Preprint at https://doi.org/10.3389/fneur.2022.862369 (2022).

Curriculum Vitae

Emily (Em) Rose Triolo

Education

Ph.D. **University of Washington, Mechanical Engineering** 2024

M.Eng. **Stevens Institute of Technology, Mechanical Engineering** 2021

GPA: 4.0, Masters Concentration: Medical Device Engineering

B.S. **The College of New Jersey, Biomedical Engineering** 2019

GPA: 3.85, Fred O. Armstrong Scholar- Highest GPA in Graduating Class

Research track, honors program student

Experience

Ph.D. Student Researcher, KurtLab
2019-2024

University of Washington 2022-2024

Stevens Institute of Technology 2019- 2021

Doctoral researcher in Dr. Mehmet Kurt's lab developing MR compatible devices and post-processing pipelines for performing MR elastography of the brain at 7T and 3T MRI to model the human brain and develop diagnostic techniques for neurological disorders.

Responsibilities: collecting and curating brain MRI datasets, developing and training others in in MRI protocols, image analysis, and post-processing (MATLAB, Freesurfer, SPM, FSL), operating 3T Siemens Prisma MRI scanner for human and phantom studies, writing IRBs for human imaging studies, maintenance, training, and printing jobs for 3-D printers, maintaining data backups, scientific paper writing, research grant writing, setting up jobs and performing simulations on UW's HPC environment, building computational workflows and SOPs

Transferred with Dr. Kurt from Stevens Institute of Technology to the University of Washington in Jan 2022 to continue work in the same lab and on the same projects.

Ph.D. Student Research Volunteer, BMEII, Mount Sinai Hospital 2021-2024

Student Research Volunteer in Dr. Priti Balchandani's laboratory assisting with 7T MRI clinical research involving healthy aging, mild cognitive impairment, and Alzheimer's Disease

I work in collaboration with Dr. Balchandani's lab as part of my work as a Ph.D. student researcher in Dr. Kurt's lab (UW) and many responsibilities and skills overlap. I assist in coordination between the two labs, including the PIs, other researchers and students.

Undergraduate Student Researcher, The College of New Jersey 2017-2019

Undergraduate student researcher in Dr. Brett BuSha's bioinstrumentation laboratory developing and performing human testing for a powered, 3-D printed orthotic exoskeleton for the human hand to augment grip and pinch strength. I was the only active student researcher in the lab at this time.

Responsibilities: literature review, control system development, physiological signal processing, human data collection, prototyping, scientific writing, independent work, and coding in MATLAB and C++ (Arduino).

Laboratory Supervisor and Assistant, The College of New Jersey, School of Engineering 2017-2019

Shift supervisor for engineering building labs after-hours

Responsibilities include supervising students using labs, other student workers on shift, cleaning and closing labs and classrooms when building closes, assisting machinist and 3D printing lab

Peer Tutor, *The College of New Jersey, Tutoring Center* 2016-2019

Tutored individuals or groups in mechanics, biomechanics, physiological systems, circuit analysis, physics, calculus, and computer science

Team Engineering, *The College of New Jersey, School of Engineering* 2016-2019

Gives tours of the engineering facilities to prospective students, parents, and alumni

Talks to prospective students and their parents during open houses and accepted students days

Honors and Awards

SB3C PhD Paper Competition – Runner Up	2024
Robert Crooks Stanley Fellowship	2020-21, 2021-22
SB3C Diversity Participation Award	2021,22
NSF GRFP – Honorable Mention	2021
Stevens Institute of Technology Provost Fellowship	2019-2021
Fred O. Armstrong Scholar – Biomedical Engineering	Class of 2019
TCNJ Academic Scholarship	2015-2019
Conrad and Melita Johnson Scholarship Endowment Fund	2018
Tau Beta Pi Scholarship	2018
NASA New Jersey Space Grant Consortium Research Stipend	Summer 2018
Freshman Engineering Fund Scholarship	2015

Guest Lectures & Invited Presentations

Intro to Biomechanics, University of Notre Dame
October 2023

Invited guest lecturer by Dr. Maria Holland (Assistant Professor, University of Notre Dame) to present my research on MRI and applications in tissue mechanics and viscoelasticity. Lecture was a 50-minute seminar titled "Development of Advanced MR Elastography Techniques for Biomechanical Assessment of Neurodegeneration".

Biomechanical Imaging: Principles and Methods, University of Washington
November 2023

Invited to teach a class and give a demonstration about how to read and analyze MR Elastography data. The lecture and demonstration were 1.5 hours and was titled "MR Elastography and NeuroImage Processing". The presentation detailed how MRE works as a sequence, what MRI scanners output, different MRI data formats, how the steps for processing an MRE dataset, noise metrics, segmentation, co-registration, and masking in neuroimaging. This lecture included four

demos: processing an MRE dataset, calculating signal-to-noise, using FreeSurfer for segmentation, and using SPM for co-registration of different imaging types.

Publications

Journal Papers

[J1] **E. Triolo**, O. Khegai, T. Lam, M. McGarry, J. Veraart, A. Alipour, P. Balchandani, M. Kurt. "Understanding the Effect of Resolution and Signal-to-Noise Ratio on Brain Mechanics Measurements Through 7T MR Elastography," *Physics in Medicine and Biology, Major Revisions*

[J2] **E. Triolo**, W. Meinhold, E. Ozkaya, J. Ueda, M. Kurt, "Magnetic Resonance Elastography. For Mechanical Modeling of the Human Lumbar Intervertebral Disc," *Proceedings of Engineering in Medicine and Biology Conference*, 2024, *Full Contributed Paper*

[J3] W. Meinhold, E. Ozkaya, D. Petti, V. Rice, **E. Triolo**, F. Rezayaraghi, P. Kennedy, L. Fleysher, A. Hu, J. Ueda, M. Kurt. "Towards Image Guided Magnetic Resonance Elastography via Active Driver Positioning Robot," in *IEEE Transactions on Biomedical Engineering*, 69(11), 2022. doi: 10.1109/TBME.2022.3168494.

[J4] **Emily Triolo**, Oleksandr Khegai, Efe Ozkaya, Nicholas Rossi, Akbar Alipour, Lazar Fleysher, Priti Balchandani, Mehmet Kurt. "Design, Construction, and Implementation of an MR Elastography Actuator" *Current Protocols,* 2(3), 2022. https://doi.org/10.1002/cpz1.379

[J5] **Emily R. Triolo**, Brett F. BuSha "Design and Experimental Testing of a Force-Augmenting Exoskeleton for the Human Hand" *Journal of NeuroEngineering and Rehabilitation*, 19(23), 2022.

[J6] E. Ozkaya, **E. Triolo**, F. Rezayaraghi, J. Abderezaei, W. Meinhold, K. Hong, A. Alipour, P. Kennedy, L. Fleysher, J. Ueda, P. Balchandani, M. Eriten, C. Johnson, Y. Yang, and M. Kurt. "Brain-Mimicking Phantom for Biomechanical Validation of Motion Sensitive MR Imaging Techniques" *Journal of the Mechanical Behavior of Biomedical Materials,* Volume 122, 2021, 104680.

[J7] **E.R. Triolo**, M.H. Stella and B.F. BuSha, "A force augmenting exoskeleton for the human hand designed for pinching and grasping," *Proceedings of Engineering in Medicine and Biology Conference,* 2018, *Full Contributed Paper*

Conference Papers & Abstracts

[C1] **E. Triolo**, M. Langan, O. Khegai, A. Diaz, S. Binder, T. Hedden, P. Balchandani, M. Kurt. "Relationship between brain stiffness, microstructural integrity, beta-amyloid accumulation and cognitive decline in beta-amyloid positive individuals," AAIC 2024, July 28 – Aug 1 2024, *Poster*

[C2] **E. Triolo**, M. Langan, O. Khegai, S. Binder, T. Hedden, P. Balchandani, M. Kurt, "Cross-Correlation of Biomechanical, Connectomic, and Pathologic Markers in Neurodegeneration at 7T MRI," *SB3C 2024*, June 11-14 2024, Lake Geneva, WI, USA. *PhD Paper Competition – Runner Up*

[C3] **E. Triolo**, M. Langan, O. Khegai, S. Binder, T. Hedden, P. Balchandani, M. Kurt, "A Multi-Modal Biomechanical Imaging and Analysis Framework for Co-Correlation of 7T MR Elastography, 7T DTI, and Amyloid Deposition," *2024 ISMRM & ISMRT Annual Meeting & Exhibition*, May 4-9 2024, Singapore. *Power Pitch & MRE Study Session Young Investigator Abstract Award*

[C4] **E. Triolo**, O. Khegai, A. Frankini, M. McGarry, P. Balchandani, M. Kurt, "Determining the Relationship between DTI and MR Elastography Metrics in Highly Anisotropic White Matter Structures at 7T," *2024 ISMRM & ISMRT Annual Meeting & Exhibition*, May 4-9 2024, Singapore. *Digital Poster*

[C5] C. Neher, **E. Triolo**, M. Kurt, "Regional Correlation of Stiffness and Perfusion in the Human Brain at 7T MRI through MR Elastography and Arterial Spin Labeling Techniques," *2024 ISMRM & ISMRT Annual Meeting & Exhibition*, May 4-9 2024, Singapore. *Digital Poster*

[C6] **E. Triolo**, M. Langan, O. Khegai, A. Diaz, S. Binder, T. Hedden, P. Balchandani, M. Kurt. "Relationship between brain stiffness, microstructural integrity, beta-amyloid accumulation and cognitive decline in beta-amyloid positive individuals," BMEII Symposium 2024, *Podium Presentation*

[C7] C. Neher, K. Green, **E. Triolo**, M. Kurt, "Voxelwise Correlation of Magnetic Resonance Elastography and Arterial Spin Labeled Imaging Signals in the Human Brain," *Biomedical Engineering Society (BMES) Annual Meeting 2023,* October 11-14, Seattle, WA, USA. *Podium Presentation*

[C8] **E. Triolo**, O. Khegai, A. Alipour, P. Balchandani, M. Kurt, "Multifrequency Magnetic Resonance Elastography (MRE) of the Human Brain at 7T," *Biomedical Engineering Society (BMES) Annual Meeting 2023,* October 11-14, Seattle, WA, USA. *Podium Presentation*

[C9] **E. R. Triolo**, M. Langan, O. Khegai, A. Alipour, C. Ferreira-Atuesta, A. Pionteck, J. Sutkowsky, T. Hedden, P. Balchandani, and M. Kurt, "A Biomechanical Analysis Framework for Co-Correlation of 7T MR Elastography Measures and Amyloid Beta Deposition," *Proceedings of the Joint Annual Meeting ISMRM-ISMRT, 2023,* 2023, Digital Poster

[C10] **E. Triolo**, M. Eritrean, C. Johnson, M. Kurt, "Utilizing MR Elastography to Visualize Higher Harmonic Components of Wave Propagation in Phantoms with Interfaces", 2023 *ISMRM & ISMRT Annual Meeting & Exhibition,* June 03-08 2023, Toronto, ON, Canada. *Digital Poster*

[C11] Mackenzie Langan , **Em Rose Triolo**, Oleksandr Khegai, Carolina Ferreira-Atuesta, Jonathan Sutkowski, Trey Hedden, Mehmet Kurt and Priti Balchandani, "Identifying multimodal imaging biomarkers: a framework exploring association of β-Amyloid Accumulation and Microstructural integrity at 7T", *2023 ISMRM & ISMRT Annual Meeting & Exhibition*, June 03-08 2023, Toronto, ON, Canada. *Digital Poster*

[C12] **E. Triolo**, O. Khegai, A. Alipour, T. Hedden, P. Balchandani, M. Kurt, "High Resolution MR Elastography of the Human Brain: Technical Development And Applications In Aging And Alzheimer's Disease," *11th Annual BioMedical Engineering and Imaging Institute Symposium*, 2023, April 20-21, NYC, New York, USA, *Poster and Innovation Station Exhibit*

[C13] **E. R. Triolo**, O. Khegai, A. Alipour, T. Hedden, P. Balchandani, and M. Kurt, "High Resolution MR Elastography of the Human Brain: Technical Development and Applications in Aging and Alzheimer's Disease," *Proceedings of SB3C,* 2023, *Podium Presentation*

[C14] **E. R. Triolo**, O. Khegai, J. Veraart, A. Alipour, P. Balchandani, and M. Kurt, "How Signal-To-Noise Ratio Impacts the Apparent Stiffness Of Brain Tissue In MR Elastography At 7T," *Proceedings of SB3C,* 2022, Poster

[C15] **E.R. Triolo**[†], O. Khegai[†], J. Veraart, A. Alipour, T. Hedden, M. Kurt*, P. Balchandani*, "Parameter Optimization for High-Resolution MR Elastography of the Human Brain at 7T," *Proceedings of the Joint Annual Meeting ISMRM-ESMRMB,* 2022, *ePoster & MRE Study Group Invited Presentation* ([†]co-first author, *co-last author)

[C16] **E.R. Triolo**, A. Alipour, O. Khegai, P. Balchandani, and M. Kurt, "Multifrequency Magnetic Resonance Elastography (MRE) at 7T," *Proceedings of the 10th Annual BioMedical Engineering and Imaging Institute Symposium,* 2022, Poster

[C17] **E. R. Triolo**, O. Khegai, A. Alipour, P. Kennedy, P. Balchandani, and M. Kurt, "Validation and Testing of 7T MR elastography sequence and stiffness reconstruction," *Proceedings of BMES Annual Meeting,* 2021, Virtual Poster

[C18] **E. Triolo**, A. Pionteck, A. Alipour, O. Khegai, P. Kennedy, P. Balchandani, and M. Kurt. "Development and Validation of an Ultra-High Field Compatible MR Elastography Actuator", *Proceedings of SB3C,* 2021, Virtual Podium Presentation

[C19] E. Ozkaya, W. Meinhold, D. Petti, **E. Triolo**, P. Kennedy, L. Fleysher, J. Ueda, M. Kurt, "Parallel Stage Mechanism Image Guided and Targeted MR Elastography", Summer Biomechanics, Bioengineering, and Biotransport Conference (SB3C), June 14-18th 2021, Virtual.

[C20] **E. Triolo**, T. Detroux, J. Abderezaei, Y. Yang, M. Kurt, "Nonlinear Dynamics of a Brain-Mimicking Phantom Under MR Imaging", Biomedical Engineering Society (BMES) Annual Meeting, OCT 14-17th 2020, Virtual

[C21] T. Detroux and **E. Triolo** and J. Abderezaei and M. Kurt, "Numerical and experimental investigation of the nonlinear dynamics in the human brain", International Mechanical Engineering Congress and Exposition, November 16-19 2020, Virtual, Conference Proceedings

[C22] E. Ozkaya, V. Rice, N. Rossi, J. Abderezaei, **E. Triolo**, L. Fleysher, P. Kennedy, Y. Yang, M. Kurt "A Novel MRI Phantom Test Setup For Validation of Mechanical Imaging Techniques via Tissue Mimicking Phantoms", *Summer Biomechanics, Bioengineering, and Biotransport Conference (SB3C)*, July 17-20th 2020, Virtual

[C23] **E.R. Triolo**†, E. Ozkaya†, K. Hong, L. Fleysher, P. Kennedy, Y. Yang, and M. Kurt. "A novel MRI setup for validation of Amplified MRI via Intrinsic actuation of tissue-mimicking phantoms," *Proceedings of BioMedical Engineering and Imaging Institute Conference*, 2020. (†co-first)

Professional Affiliations

ISTAART, *Student Member,* 2024

ISMRM, *Trainee Member***,** 2021-Present

Tau Beta Pi, *Member and Chapter President (2018), New Jersey Zeta*, 2017-Present

IEEE and EMB, *Student Member* 2015-Present

BMES, Student Member, 2015-2016, 2021-Present

Service & LGBTQ+ Outreach

KurtLab.com/Pride Administrator

[Funding List Organizer, PRIDE Reviewer], 2021-present

[SB3C LGBTQ+ Social, Assistant Organizer], SB3C Annual Meeting 2022, 2023

Thanksgiving Canned Food Drive Organizer

[Organizer- Chapter President], [New Jersey Zeta Tau Beta Pi], 2018

GLOW (Gay, Lesbian, Or Whatever) Club President

[Club President], [Biotechnology High School], 2014-15